Suppressing loss channels in the bulk and at the surface of crystalline silicon solar cells

Der Fakultät für Mathematik und Physik

der Gottfried Wilhelm Leibniz Universität Hannover

zur Erlangung des Grades

Doktor der Naturwissenschaften

Dr. rer. nat.

genehmigte Dissertation

von

Dipl.-Phys. Dimitri Zielke

geboren am 24.11.1983 in Schapaewsk / Russland

2016

Referent:	Prof. Dr. Jan Schmidt
Korreferent:	Prof. Dr. Tobias Wietler
Tag der Promotion:	13.10.2016

Kurzzusammenfassung

Im Rahmen dieser Arbeit werden verschiedene innovative Ansätze verfolgt, um die dominanten Verlustmechanismen in den heutigen kristallinen Siliziumsolarzellen zu verringern. Das Augenmerk wird dabei auf folgende Komponenten einer Solarzelle gerichtet: (i) den Metall-Halbleiter-Kontakt auf dem n^+-Emitter, (ii) den löchersammelden Kontaktbereich, (iii) die Rekombination im Siliziumvolumen und (iv) die Oberflächentexturierung des multikristallinen Siliziums.

Die Implementierung einer ultradünnen ALD-AlO_x-Schicht als neuartige passivierende Tunnelschicht zwischen einem phosphordotierten n^+-Emitter und einer aufgedampften Al-Vorderseitenmetallisierung einer PERC-Solarzelle wird erstmals untersucht. Eine optimale ALD-AlO_x-Schichtdicke wird identifiziert, welche die Al-Kontakte passiviert, das Al-‚Spiking' verhindert und einen guten Stromtransport gewährleistet. Durch den Vergleich der Messergebnisse einer Solarzelle und einer Lebensdauerprobe wird die Effektivität der AlO_x-Kontaktpassivierung bestimmt. Eine Zunahme der AlO_x-Schichtdicke über das Optimum hinaus führt zu einer Abnahme des Füllfaktors, was auf die drastische Abnahme der Tunnelwahrscheinlichkeit zurückgeführt wird. PERC-Solarzellen mit einer optimalen Dicke der ALD-AlO_x-Tunnelschicht erreichen einen unabhängig bestätigten Rekordwirkungsgrad von 21,7% und eine Leerlaufspannung von 673 mV.

Ein neuartiger Polymer-Silizium-Heteroübergang wird analysiert, basierend auf dem löcherleitenden Polymer PEDOT:PSS. Mittels Lebensdauermessungen wird erstmals ein überraschend niedriger Wert der Sättigungsstromdichte J_0 des PEDOT:PSS/c-Si-Heteroübergangs von 46 fA/cm² gemessen. Solarzellen mit PEDOT:PSS auf der Vorderseite eines *n*-Typ c-Si-Wafers werden realisiert und erreichen einen Rekordwirkungsrad zum Zeitpunkt der Publikation von 12,3%. Die PEDOT:PSS-Dispersion und die Vorbehandlung der c-Si-Oberfläche werden bezüglich niedriger J_0-Werte und Kontaktwiderstände R_C optimiert. Ein neuartiges Konzept wird eingeführt, die sogenannte „*BackPEDOT*"-Solarzelle, mit einem realistischen Wirkungsgradpotential von 22%. Erste experimentelle *BackPEDOT*-Solarzellen werden realisiert mit einem Wirkungsgrad von 20,6%, welcher den höchsten bislang erreichten Wirkungsgrad einer PEDOT:PSS/c-Si-Solarzelle darstellt.

Degradationsexperimente am PEDOT:PSS/c-Si-Heteroübergang werden durchgeführt. Die *J-V*-Kennlinie einer Solarzelle unter Beleuchtung entwickelt einen ‚*S*-förmigen' Verlauf bei Lagerung an Luft. Der Kontaktwiderstand R_C wird identifiziert als der am meisten beeinflusste Parameter, wobei die Luftfeuchtigkeit als Haupursache der Degradation identifiziert wird. Mithilfe der Kelvin-Sonde-Messung wird die Abnahme der Austrittsarbeitsdifferenz ΔW_A der PEDOT:PSS/c-Si Probe bei Lagerung an Luft detektiert. Ein Modell wird entwickeln, bei dem die Reduzierung der Austrittsarbeit W_A der PEDOT:PSS die Band-Offsets an der PEDOT:PSS/c-Si-Grenzfläche verändert, was zu einer Barriere für den Löchertransport führt. Eine neuartige Verkapselungsmethode der *BackPEDOT*-Solarzellen wird eingesetzt und ein stabiler Wirkungsgrad bei Langzeitlagerung an Luft nachgewiesen.

PERC-Solarzellen auf multikristallinen Silizium (mc-Si) Wafern werden hergestellt. Unsere Simulationen und Solarzellenergebnisse zeigen, dass bei Verwendung eines hochreinen Schmelztiegels und der Ausdehnung der monokristallinen Flächenanteile des mc-Si-Materials vergleichbare Ergebnisse wie auf monokristallinen Silizium erreichbar sind. Auf einer ausgewählten mc-Si-Fläche von 1 × 1 cm² wird eine sehr hohe Effizienz von 20% erreicht, welche zu dem Zeitpunkt der Publikation nur marginal unter dem Effizienz-Weltrekord für mc-Si-Solarzellen von 20,4% lag.

Eine direkte Lasertextur (*DiLaT*) auf PERC-Solarzellen wird implementiert. Der Vorteil der *DiLaT*-Textur ist die Abwesenheit von jeglichen Maskierungsschichten und die Anwendbarkeit auf jede Kristallorientierung, sodass auch diese Methode ideal geeignet ist für mc-Si-Wafer. An Float-zone-Si-Wafern werden für die RP-texturierten und für die *DiLaT*-texturierten Solarzellen vergleichbare Resultate erreicht. Auf mc-Si-Wafern wird ein unabhängig bestätigten J_{sc}-Wert von 39,3 mA/cm² erreicht, welcher zum Zeitpunkt der Publikation der höchste berichtete J_{sc}-Wert für eine mc-Si-Solarzelle war. Dieses Ergebnis zeigt das hohe Potenzial der *DiLaT*-Textur.

Schlagworte: Aluminiumoxid, PEDOT:PSS/c-Si-Heteroübergang, Multikristallines Silizium, Lasertextur

Abstract

In the present thesis, we introduce different innovative approaches to reduce predominant loss channels in today's crystalline silicon solar cells. The following components of a solar cell are examined: (i) the metal-semiconductor contact at the n^+-emitter, (ii) the hole contact region, (iii) the silicon bulk recombination and (iv) the surface texturing of multicrystalline silicon.

The application of ultrathin ALD-AlO_x as a novel contact-passivating tunneling layer between the phosphorus-doped n^+-emitter and the Al-evaporated front metal grid of a lab-type PERC solar cell is investigated. An optimal ALD-AlO_x layer thickness is identified, which passivates the Al-contacts, prevents the Al-spiking and allows for a good current transport. Comparing the solar cell results and the lifetime sample measurements, we determine the effectiveness of the AlO_x contact passivation. Increasing the AlO_x thickness above the optimum leads to a decrease in fill factor due to a drastically reduced tunneling probability. PERC solar cells featuring an ALD-AlO_x tunneling layer show an independently confirmed record-high efficiency of 21.7% and a V_{oc} of 673 mV.

An in-depth analysis of organic-silicon heterojunctions based on the hole-conducting polymer PEDOT:PSS is performed. Using lifetime measurements, we determine for the first time the surprisingly low J_0 value of 46 fA/cm² of the PEDOT:PSS/c-Si heterojunction. Heterojunction solar cells with PEDOT:PSS on c-Si *n*-type silicon wafer front surfaces are realized and a record-high efficiency at the time of publication of 12.3% is achieved. PEDOT:PSS dispersion and the silicon surface pre-treatment are optimized towards reduced J_0 and the R_C values. We introduce a novel solar cell concept – the so-called '*BackPEDOT*' solar cell – with a realistic efficiency potential 22%. First *BackPEDOT* experimental devices are realized with an outstanding efficiency of 20.6%, which is by far the highest efficiency for a PEDOT:PSS/c-Si solar cell to date.

Degradation experiments on our PEDOT:PSS/c-Si heterojunction solar cells are performed. The illuminated *J-V* curves show an '*S*-shaped' form with increasing time in air. The contact resistance R_C is identified as the most affected solar cell parameter with the humidity as the major source of degradation. Using Kelvin-probe measurements, we detect a decreasing work function ΔW_A difference of the PEDOT:PSS/c-Si samples stored in air. We develop a model, where a decreasing W_A of the PEDOT:PSS alters the energy band configuration, forming a barrier for holes. A novel effective encapsulation method for *BackPEDOT* solar cells is applied with stabilized efficiency under long-term storage in air.

We fabricate PERC solar cells on block-cast multicrystalline silicon (mc-Si) from an industrial supplier and from a laboratory-scale high-purity crucible. Our simulations and solar cell results show that the reduced bulk quality is largely avoidable using a high-purity crucible during casting and by extending monocrystalline areas. On a selected mc-Si area of 1 × 1 cm² we achieve a very high solar cell efficiency of 20.0%, which was during the time of publication only slightly below the record value of 20.4%.

We implement a direct laser texturing (*DiLaT*) process into lab-type PERC solar cells. The advantage of the *DiLaT* texture is the absence of any masking layer and its applicability to any crystal orientation as it is the case for mc-Si wafers. On FZ-Si substrates we obtain similar cell parameters for the *DiLaT* as compared to random-pyramid texturing. On mc-Si we achieve an independently confirmed J_{sc} value of 39.3 mA/cm², which was the highest reported J_{sc} value at the time of publication for any mc-Si solar cell, highlighting the enormous potential of *DiLaT* for the application to mc-Si solar cells.

Keywords: aluminum oxide, PEDOT:PSS/c-Si heterojunction, multicrystalline silicon, laser texture

Contents

GLOSSARY 1-X

1 INTRODUCTION 1

2 FUNDAMENTALS AND CHARACTERIZATION 5

2.1 Solar cell parameters 5

2.2 Solar cell characterization 7
2.2.1 Quantum efficiency (QE) 7
2.2.2 Current-density voltage characterization (*J*-*V*) 7

2.3 Dependence of open-circuit voltage on excess carrier concentration $V_{oc}(\Delta n)$ 8

2.4 Recombination channels 9
2.4.1 Radiative recombination 9
2.4.2 Auger recombination 9
2.4.3 Shockley-Read-Hall recombination 10
2.4.4 Recombination at the surface 10
2.4.5 Total lifetime 11
2.4.6 Determination of the saturation current density J_0 11

2.5 Photoconductance-based lifetime measurements 12

2.6 Camera-based lifetime measurement techniques 13
2.6.1 Dynamic infrared lifetime mapping (ILM) 13
2.6.2 Photoconductance-calibrated photoluminescence lifetime imaging (PC-PLI) 14

3 CONTACT PASSIVATION WITH ALD-ALO$_X$ TUNNELING LAYER 15

3.1 Experimental details 15
3.1.1 n^+-emitter fabrication 15
3.1.2 Passivation schemes 16

3.2 Solar cells with AlO_x tunneling contacts 21
3.2.1 Experimental details 22
3.2.2 Solar cell results and discussion 23

3.3 Efficacy of AlO_x contact passivation 29

3.4 Comparison with other groups 31

3.5 Chapter summary 32

4 PEDOT:PSS/C-SI HETEROJUNCTIONS 35

4.1 Organic conductive polymers 36

4.2 Deposition of PEDOT:PSS from the aqueous solution 38

4.3 PEDOT:PSS/c-Si heterojunction solar cells 40

4.4 Efficiency potential of PEDOT:PSS/c-Si solar cells 40
4.4.1 Investigation of optical properties of the PEDOT:PSS layer 41
4.4.2 Passivation properties of PEDOT:PSS on c-Si 43
4.4.3 Realistic Efficiency potential of PEDOT:PSS/c-Si solar cells 44

4.5 Fabrication of organic-silicon heterojunction solar cells 46
4.5.1 *FrontPEDOT* processing sequence 46
4.5.2 *BackPEDOT* processing sequence 48
4.5.3 Solar cell results and discussion 49

4.6 Optimizing the PEDOT:PSS/c-Si interface 52
4.6.1 Optimization of the PEDOT:PSS composition 52
4.6.2 Optimization of the silicon surface pre-treatment 53
4.6.3 Contact resistance 55
4.6.4 Optimized organic-silicon heterojunction solar cells 57

4.7 Chapter summary 61

5 PEDOT:PSS JUNCTION: DEGRADATION AND STABILIZATION 63

5.1 Evolution of efficiency 63

5.2 Effect of encapsulation and storage in a humidity-reduced environment 67

5.3 Degradation mechanisms 69
5.3.1 First hypothesis: silicon oxide at the PEDOT:PSS/c-Si interface 71
5.3.2 Second hypothesis: drift in the PEDOT:PSS work function 72

5.4 Chapter summary 75

6 EFFICIENCY POTENTIAL OF MULTICRYSTALLINE SILICON WAFERS 77

6.1 Block casting of multicrystalline silicon 77

6.2 Impact of phosphorus gettering 78

6.3 Fabrication of multicrystalline silicon solar cells 81

6.4 Chapter summary 85

7 LASER-TEXTURING OF MULTICRYSTALLINE SILICON 87

7.1 Random-pyramid texturing 87

7.2 The honeycomb texture 88

7.3 Direct laser texturing (*DiLaT*) 89
7.3.1 Direct laser texturing process 89
7.3.2 Laser damage removal by wet chemical treatment 90

7.4 Application of direct laser texturing to solar cells 92
7.4.1 Solar cell structure and processing sequence 92
7.4.2 Solar cell results 94

7.5 Chapter summary **98**

8 SUMMARY **99**

9 BIBLIOGRAPHY **103**

10 LIST OF PUBLICATIONS **111**

Refereed journal papers 111

Refereed papers presented at international conferences 112

Awards and Prizes 113

Glossary

Δn	Excess carrier concentration	[cm^{-3}]
θ	Temperature	[°C]
η_0	Initial energy conversion efficiency	[%]
η	Energy conversion efficiency	[%]
η_0	Initial energy conversion efficiency	[%]
$\eta_{relative}$	Relative energy conversion efficiency	[%]
ρ	Resistivity	[Ωcm]
σ	Conductivity	[S/cm]
μ_e/ μ_h	Electron / hole mobility	[cm^2/Vs]
χ	Electron affinity	[eV]
τ_n/τ_p	Capture time constants	[s]
τ	Lifetime	[s]
τ_{eff}	Effective lifetime	[s]
τ_{Auger}	Auger lifetime	[s]
τ_{rad}	Radiative lifetime	[s]
τ_{int}	Intrinsic lifetime	[s]
τ_{SRH}	Shockley-Read-Hall lifetime	[s]
ω	Angular velocity	[m/s]
A	Area	[cm^2]
$A(\lambda)$	Absorbed light fraction	
ALD	Atomic layer deposition	
AlO_x	Aluminum oxide	
ARC	Anti reflection coating	
a-Si	Amorphous silicon	
B	Coefficient of the radiative recombination	[cm^3/s]
BSF	Back surface field	
C	Capacitance	[F]
$c1$, $c2$, $c3$	Coefficients	
C_n, C_p	Auger coefficients	[cm^6/s]
c-Si	Crystalline silicon	
D_n/ D_h	Electron/hole diffusion coefficient	[cm^2/Vs]
$D(E)$	Density of states	[cm^{-3}]
D_{it_midgap}	Midgap interface defect density	[$eV^{-1}cm^{-2}$]
ECR	Electron contact region	
E_C	Conductance band	[eV]
E_V	Valence band	[eV]
E_F	Fermi-level	[eV]
E_{Fn}/ E_{Fp}	Quasi-Fermi-level of electrons / holes	[eV]
E_t	Defect energy level	[eV]
E_G	Band gap	[eV]
EQE(λ)	External quantum efficiency	[%]
f	Metallization fraction	[%]
$f(E)$	Fermi-Dirac- distribution	

FSF	Front surface field	
FF	Fill factor	[%]
G	Generation of a casted silicon ingot	
G	Generation rate	[$cm^{-3}s^{-1}$]
G_{th}	Thermal generation rate	[$cm^{-3}s^{-1}$]
GPC	Growth pre cycle	
g_{eeh} / g_{ehh}	Enhancement factors for a eeh and ehh Auger process	
HCR	Hole contact region	
HOMO	Highest occupied molecular orbital	[eV]
HF	Hydrofluoric acid	
i	Current	[mA]
I	Current	[mA]
I_{mpp}	Current at the maximum power point	[mA]
IQE(λ)	Internal quantum efficiency	[%]
J	Current density	[A/cm^2]
J_{sc}	Short-circuit current density	[mA/cm^2]
J_{ph}	Photogenerated current density	[mA/cm^2]
J_{mpp}	Current density at the maximum power point	[mA/cm^2]
J_{rec}	Recombination current density	[mA/cm^2]
J_0	Saturation current density at the surface/HCR/ECR	[fA/cm^2]
$J_{0_cont_unpass}$	Saturation current density at the non-passivated contact	[fA/cm^2]
$J_{0_cont_pass}$	Saturation current density at the passivated contact	[fA/cm^2]
J_{0_bulk}	Saturation current density in the silicon bulk	[fA/cm^2]
J_{0_rear}	Saturation current density at the rear surface of a solar cell	[fA/cm^2]
J_{0_cell}	Saturation current density in a solar cell	[fA/cm^2]
$k(\lambda)$	Extinction coefficient, as function of wavelength	
k_B	Boltzmann constant	[J/K]
KOH	Potassium hydroxide	
LUMO	Lowest unoccupied molecular orbital	[eV]
L	Minority-carrier diffusion length	[µm]
L_{min}	Minimal minority-carrier diffusion length	[µm]
m	Metallization factor	[%]
mc-Si	Multicrystalline silicon	
MO	Molecular orbit	
N_A/N_D	Doping concentration of acceptors / donors	[cm^{-3}]
N_C	Effective density of states in the conduction band	[cm^{-3}]
N_V	Effective density of states in the valence band	[cm^{-3}]
N_t	Defect density	[cm^{-3}]
n / p	Electron/hole concentration	[cm^{-3}]
n_0 / p_0	Electron/hole concentration in equilibrium	[cm^{-3}]
n_i	Intrinsic carrier concentration	[cm^{-3}]
$n(\lambda)$	Refraction indices, as function of wavelength	
n_{id}	Ideality factor	
n_{id}	Local ideality factor	
one-sun	Illumination intensity of 1000 W/m^2	
PECVD	Plasma-enhances chemical vapor deposition	

PERC	Passivated emitter and rear solar cell	
PEDOT:PSS	Poly(3,4-ethylenedioxythiophene):(styrenesulfonate)	
PSG	Phosphorus silicate glass	
PCD	Photoconductance decay	
$POCl_3$	Phosphoryl chloride	
p	Pitch	[cm]
P_{light}	Power density of the light irradiated on the surface of a solar cell	[W/cm²]
P	Power density	[W/cm²]
pFF	Pseudo fill factor	[%]
pη	Pseudo energy conversion efficiency	[%]
Q_f	Fixed charge density	[cm^{-3}]
QSSPC	Quasi-steady-state photoconductance	
R	Recombination rate	[$cm^{-3}s^{-1}$]
$R(\lambda)$	Reflectance as function of the wavelength	[%]
R_{wgh}	Weighted reflectance with the AM 1.5G spectra [%]	
R_s	Series resistance	[Ωcm²]
R_{sh}	Shunt resistance	[Ωcm²]
R_{sheet}	Sheet resistance	[Ω/□]
R_{sheet_Si}	Sheet resistance of a silicon layer	[Ω/□]
R_{sheet_PEDOT}	Sheet resistance of a PEDOT:PSS layer	[Ω/□]
R_C	Contact resistance	[Ωcm²]
RPM	Revolution per minutes	[min^{-1}]
STC	Standard testing condition of illuminated *J-V* curves. STC implies one-sun illumination, a temperature of 25°C and the AM1.5G spectrum	
SRV	Surface recombination velocity	[cm/s]
S	Surface recombination velocity	[cm/s]
S_{max}	Maximal surface recombination velocity	[cm/s]
SEM	Scanning electron microscope	
S	Surface recombination velocity	[cm/s]
Si	Silicon	
SiO_x	Silicon oxide	
SiN_x	Silicon nitride	
TEM	Transmission electron microscope	
TMA	Trimethyl aluminum	
t	Time	[s]
t_{deg}	Time constant	[s]
T	Absolute temperature	[K]
U	Net recombination rate	[$cm^{-3}s^{-1}$]
V	Voltage	[mV]
V_{oc}	Open circuit voltage	[mV]
V_T	Thermal voltage	[mV]
V_{mpp}	Voltage at the maximum power point	[mV]
W	Wafer thickness	[cm]
W_A	Work function	[eV]
Z	Wavelength enhancement factor	

1 Introduction

The sun is the major source of energy available on the surface of the planet earth. The solar cell is an electronic device which directly converts light into valuable electrical energy based on the photovoltaic effect.

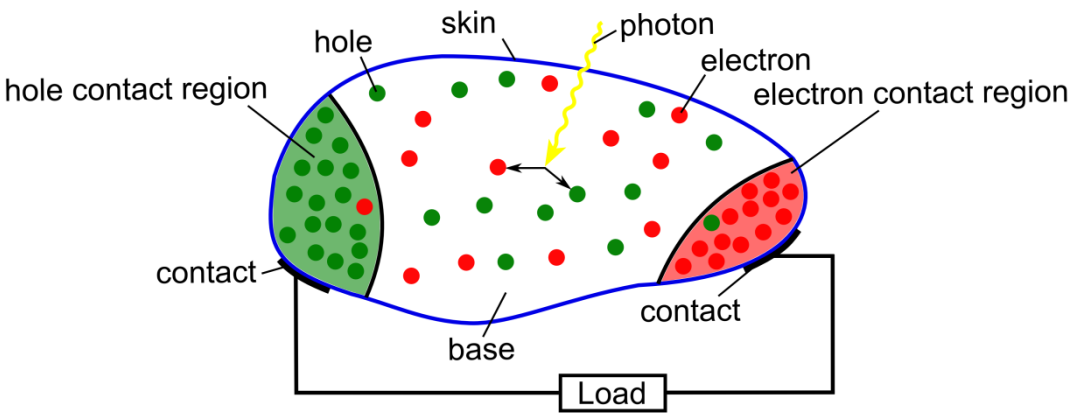

Figure 1: A basic schematic of an arbitrarily shaped solar cell with the essential components (taken from Cuevas et al. [1]).

Figure 1 shows schematically an arbitrarily shaped solar cell with its essential components according to Cuevas et al. [1]. A solar cell has a light transparent skin. Photons penetrating the skin are absorbed in the volume of the solar cell and generate electron-hole pairs. The majority of the photons are absorbed in the base. The excess carrier density of electrons and holes is Δn and Δp, respectively. The base is typically a semiconductor and requires a sufficiently high conductivity (σ) for electrons σ_e and for holes σ_h, respectively. The base of today's solar cells is doped with acceptors (for silicon a material from the 3rd group of the periodic table e.g. boron) or donors (for silicon a material from the 5th group of the periodic table e.g. phosphorus), which defines the base as *p*-type or *n*-type material, respectively. Both types of charge carriers move through the base driven by drift and diffusion. Separation of the carriers is performed by semipermeable filters, following the nomenclature of Würfel [2]. Such filters can be described by regions in the solar cell were conductivity for one charge carrier exceeds the conductivity of the other: $\sigma_h >> \sigma_e$ and $\sigma_e >> \sigma_h$ for the hole contact region (HCR) and electron contact region (ECR), respectively. The contact region with the opposite polarity compared to the base is often referred to as the 'emitter'. The term emitter is a historic term since the semiconductor structure of a solar cell is similar to a diode. In the image of a diode, a solar cell operates in the reverse bias where the emitter collects charge carries. By closing the external circuit at the contacts, charge carriers flow and power a load.

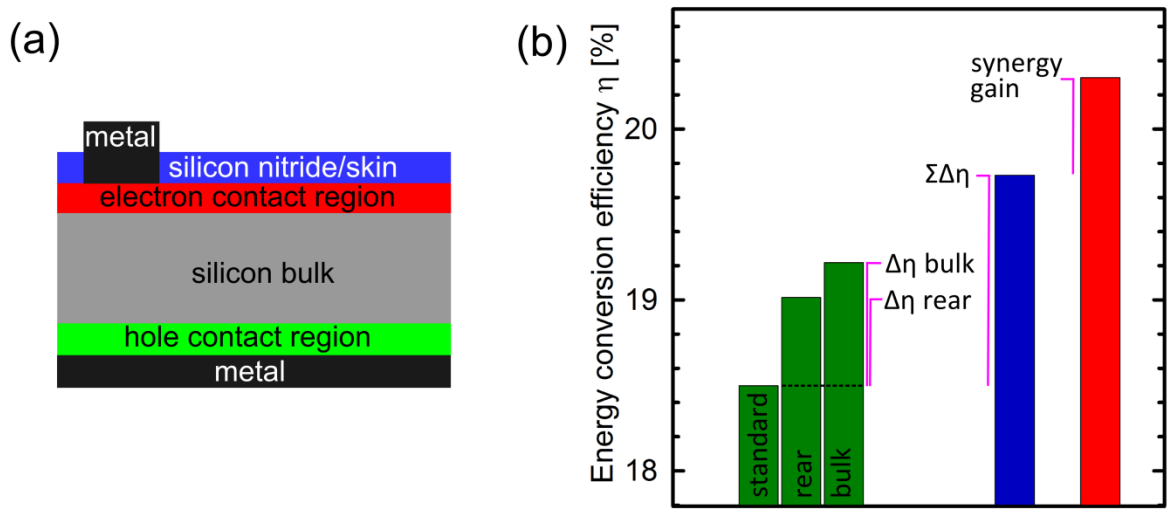

Figure 2: (a) Schematic of today's industrial standard standard c-Si solar cell. (b) Calculated solar cell energy conversion efficiencies.

Figure 2 (a) shows a simplified schematic of today's industrial standard crystalline silicon solar cell. This solar cell has a boron-doped (*p*-type) silicon base. The electron contact region (emitter) is located at the front facing the sun and is phosphorous-doped in a high-temperature diffusion process. The emitter is partially metallized by a Ag-metal grid. The HCR is formed by covering the silicon wafer rear with Al-paste followed by firing in a conveyor belt firing furnace. The front skin is a non-metallized textured emitter region passivated by a transparent silicon nitride layer, acting as antireflecting coating and to reduce front surface recombination losses.

Figure 2 (b) shows simulation results for different configurations of the recombination currents for the industrial standard solar cell. We simulate the solar cell efficiency for the standard industrial solar cell with separately reduced and successively reduced recombination channels. A set of the solar cell parameters used in our simulation is given in Table 1. The simulation is performed with the software *Quokka* 2 [3] (PVLighthouse.com.au v. 2.2.4).

Table 1: Typical solar cell parameters for an industrial solar cell. Solar cell simulation is performed with successively and simultaneously reduced recombination in the HCR and in the bulk.

Saturation current density in	Industrial	BSF	Bulk	Synergy
HCR [fA/cm²]	400	**42**	400	42
Bulk [fA/cm²]	285	285	**15**	15
Efficiency [%]	18.50	19.01	19.22	20.3

The simulated solar cells with the industrial standard parameters as given in Table 1 result in an efficiency of $\eta = 18.50\%$. By reducing the saturation current density in the HCR from 400 fA/cm² to 42 fA/cm² we simulate an efficiency of $\eta = 19.01\%$ which is a gain of $0.51\%_{abs}$ compared to the industrial solar cell. Assuming a saturation current density of 15 fA/cm² in the bulk compared to a saturation current density of 285 fA/cm² we simulate an efficiency of $\eta = 19.22\%$ which is a gain of $0.72\%_{abs}$ compared to the industrial solar cell. If we simply sum up all the efficiency gains to the industrial solar cell we obtain a total efficiency of 19.73%. A different result is obtained when all two saturation current density are reduced simultaneously in the simulation, where we obtain $\eta = 20.3\%$. The additional gain of $0.57\%_{abs}$ is due to synergetic effects [4], [5].

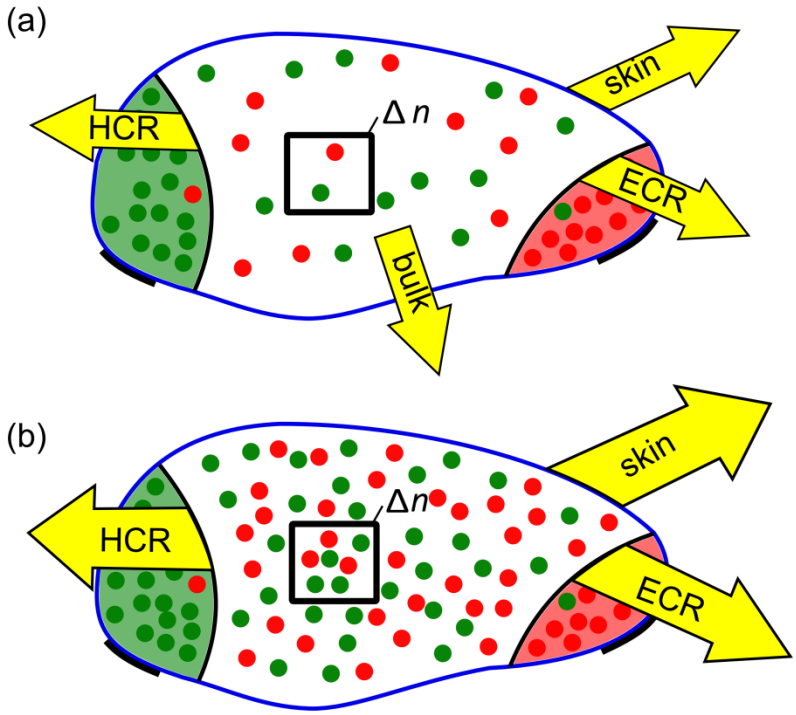

Figure 3: Visualization of (a) equally distributed power losses (yellow arrows) in a solar cell. (b) Effect on the three power losses when one power loss channel is switched off (in this case the bulk recombination). The black square represents a unit volume in the solar cell with the corresponding excess carrier density Δn.

Figure 3 (a) visualizes power loss channels in the bulk, in the HCR, in the ECR and at the skin. When one power loss channel (e.g. in the bulk) is switched off, the total recombination current in the solar cell decreases. However, this has an impact on the other loss channels, see Figure 3 (b). As a result the excess carrier density (Δn) increases in a volume unit of the solar cell. Visually, the increased Δn apply *pressure* on the remaining power loss channels and therefore increases the recombination in those channels. This image illustrates the importance of the simultaneous reduction of several power loss channels at the same time.

The present thesis focuses on reducing recombination losses of various relevant loss channels. The following components are studied: the metal-semiconductor contact at the electron contact region, the hole contact region, the silicon bulk and the skin. As exemplary solar cell structure we use the passivated emitter and rear cell (PERC) throughout this work with crystalline silicon as the base material. However, our results are not limited to one particular solar cell structure.

In more detail, this work is structured as follows:

Chapter 2 introduces the basic parameters of a solar cell and the characterization techniques employed during this work. Current density-voltage (*J-V*) and quantum efficiency (QE) measurements are discussed and a brief overview of physical mechanisms of recombination processes (power loss channels) in silicon is given. Furthermore, contactless lifetime measurement techniques based on photoconductance decay (PCD) and infrared lifetime mapping (ILM) are described.

Chapter 3 describes the fabrication sequence of our laboratory-scale passivated emitter and rear cell (PERC) devices, which is the baseline process in the present work. We present for the first time the application of an atomic-layer-deposited aluminum oxide (Al_2O_3) passivating tunneling layer in-between the phosphorus-doped emitter and the aluminum contact on the front surface of the PERC solar cell. A set of solar cells was fabricated without and with aluminum oxide of varying layer thicknesses, clearly proving the advantage of our newly introduced AlO_x tunnel layer.

Chapter 4 covers a detailed investigation of the passivation properties of an organic polymer poly(3,4-ethylenedioxythiophene):(styrenesulfonate) [PEDOT:PSS] layer on the silicon surface. Employing the PCD measurement we determined for the first time the saturation current density for this organic-silicon junction and demonstrate hereby its application to high-efficiency crystalline silicon solar cells. By combining ellipsometric measurements and using ray-tracing simulations we show the limitations of the present organic-silicon heterojunction solar cell concepts employing PEDOT:PSS on the front surface of the solar cell. We propose a novel organic-silicon solar cell concept (*BackPEDOT*), where the optical and the recombination loses are minimized. The influence of different PEDOT:PSS dispersions and silicon surface preparations prior to the PEDOT:PSS deposition on the saturation current density and contact resistance is examined in detail. Finally, we realize a high-efficiency *BackPEDOT* solar cell showing the highest efficiency of this novel type of heterojunction solar cell achieved so far.

Chapter 5 examines the long-term stability of our PEDOT:PSS/c-Si solar cells. In this thesis, we analyzed for the first time the degradation of the organic-inorganic solar cells based on PEDOT:PSS and crystalline silicon. By storing the solar cells in different environmental conditions we localized the source of degradation. A well-founded hypothesis regarding the major degradation mechanism is presented and – based on that – various approaches to improve the long-term stability of organic-silicon solar cells are presented.

Chapter 6 presents PERC solar cells based on cost-saving multicrystalline silicon (mc-Si) as the base material. We fabricate solar cells on pre-selected areas of mc-Si wafers to demonstrate the efficiency potential of this material. We implement commercially available as well as high-purity mc-Si wafers as the base material into our PERC solar cells. The high-purity mc-Si material is made at the purest possible condition at the time of fabrication. Finally, we compare SENTAURUS Device simulation with the PERC solar cell results.

Chapter 7 presents an alternative surface texture suitable for mc-Si. We developed a texturing technique based on direct ablation of silicon using a laser system and a post-treatment in an alkaline aqueous solution. We present mc-Si PERC solar cells with our newly developed direct-laser-textured surface and compare the performance of solar cells with planar surface, random pyramid and direct-laser-textured surfaces. The light path enhancement factor of the best random-pyramid solar cell is compared to that of the direct-laser-textured solar cell.

Chapter 8 concludes this thesis and summarizes the main results.

2 Fundamentals and characterization

In this Chapter, we introduce the basic solar cell parameters and the major characterization techniques used in this work. The basic physical mechanisms of carrier recombination processes in silicon are given and the lifetime measurement techniques employed in this thesis are described.

2.1 Solar cell parameters

A solar cell produces an electric current density (J) at a given voltage (V) when it is contacted and illuminated. The function $J(V)$ is the so-called J-V curve. The point on the J-V curve where the produced power density (P) reaches its maximum is defined as the maximum power point (MPP) with $P_{\mathrm{MPP}} = J_{\mathrm{MPP}} \times V_{\mathrm{MPP}}$. The efficiency of a solar cell (η) is defined by:

$$\eta = \frac{P_{\mathrm{MPP}}}{P_{\mathrm{light}}}, \tag{2.1}$$

where P_{light} is the power density of the light irradiated on the surface of a solar cell. The illuminated J-V characteristic of a solar cell can be described by the equation:

$$J(V) = J_{\mathrm{ph}} - J_{\mathrm{rec}}(V) = J_{\mathrm{ph}} - J_{0_\mathrm{cell}}\left(e^{\frac{V+J(V)R_{\mathrm{s}}}{n_{\mathrm{id}}V_T}} + 1\right) + \frac{V + J(V)R_{\mathrm{s}}}{R_{\mathrm{sh}}} \tag{2.2}$$

where J_{ph} is the photogenerated current density, J_{rec} is the recombination current density, J_{0_cell} is the saturation current density, $V_{\mathrm{T}} = k_{\mathrm{B}}T/\mathrm{q}$ is the thermal voltage (25.7 mV at a θ = 25°C), T is the absolute temperature, q is the elementary charge (1.6×10^{-19} C), n_{id} is the ideality factor ($n_{\mathrm{id}} = 1$ for an ideal diode), k_{B} is the Boltzmann constant (1.4×10^{-23} J/K), R_{s} is the series resistance and R_{sh} is the shunt resistance times device area. The saturation current density J_{0_cell} contains the lumped information about all present recombination channels. The most relevant saturation current densities in solar cells are: J_{0_bulk} in the bulk, J_{0_HCR} in the hole contact region, J_{0_ECR} in the electron contact region, and J_0 at the surface (skin). The J_{0_cell} in this case is described by the equation:

$$J_{0_\mathrm{cell}} = J_{0_\mathrm{bulk}} + J_{0_\mathrm{HCR}} + J_{0_\mathrm{ECR}} + J_0 \,. \tag{2.3}$$

Figure 4 shows calculated J-V curves using the equation (2.2) and the typical values. In case the illuminated solar cell is operated in open-circuit condition $V = V_{\mathrm{oc}}$, with V_{oc} being the open-circuit voltage, then: $J(V_{\mathrm{oc}}) = 0$. In case the illuminated solar cell is operated in short-circuit condition $J = J_{\mathrm{sc}}$, with J_{sc} being the short-circuit current density, then: $J(V = 0) = J_{\mathrm{sc}}$. In open-circuit condition, assuming $J_{\mathrm{PH}} \approx J_{\mathrm{sc}}$ and $R_{\mathrm{sh}} \geq 10000$ Ωcm², we obtain an important relation for the so-called *ideal* V_{oc} ($V_{\mathrm{oc_ideal}}$):

$$V_{\mathrm{oc_ideal}} = n_{\mathrm{id}}V_{\mathrm{T}} \ln\left(\frac{J_{\mathrm{sc}}}{J_0} - 1\right). \tag{2.4}$$

Another important solar cell parameter is the fill factor (*FF*), which is defined by the quotient:

$$FF = \frac{J_{\mathrm{MPP}} \times V_{\mathrm{MPP}}}{J_{\mathrm{sc}} \times V_{\mathrm{oc}}}. \tag{2.5}$$

Figure 4 show an exemplary *J-V* curve, a J_{sc}-V_{oc} curve shifted by J_{sc} and a *P-V* curve. The J_{sc}-V_{oc} plot corresponds to the *J-V* curve without the influence of the series resistance.

Extrinsic conditions for an operating solar cell are temperature, illumination spectra and illumination power density. A widely-used set of measurement conditions for solar cells are the standard testing conditions (STC) that imply a temperature of 25°C, the AM1.5G illumination spectrum, and a power density of 1000 W/m² (international standard IEC 60904-3-Ed2). AM1.5G means that the sun light passes 1.5 times the earth's atmosphere (which corresponds to a zenith angle of 48.2°) and the global spectra (partially diffuse and direct light). In the present thesis all solar cells are measured as close as possible to STC.

Combining equations (2.1) and (2.5), we obtain a useful relation:

$$\eta = \frac{J_{\mathrm{sc}} \times V_{\mathrm{oc}} \times FF}{100\ \mathrm{mW/cm^2}}, \tag{2.6}$$

where the importance of the essential three solar cell parameters J_{sc}, V_{oc} and *FF* becomes evident. In order to achieve high energy conversion efficiencies, J_{sc}, V_{oc} and *FF* have to be optimized at the same time.

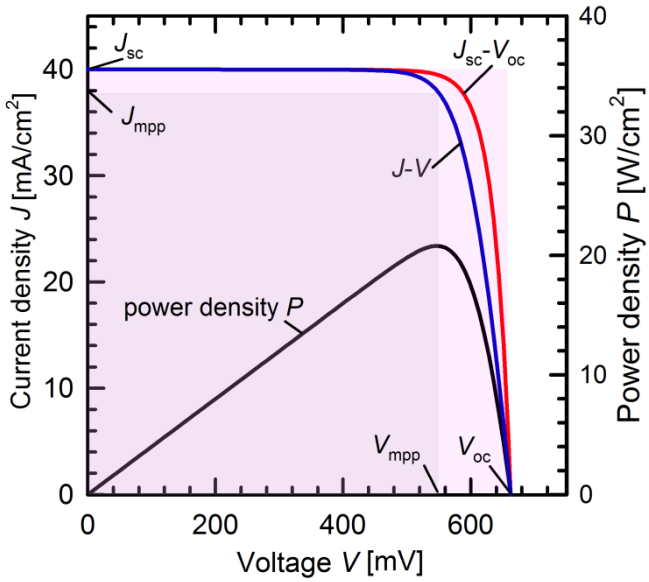

Figure 4: Current voltage *J-V* curve (blue), short-circuit current open-circuit voltage J_{sc}-V_{oc} curve shifted by J_{sc} (red) and power density voltage *P-V* curve (black).

2.2 Solar cell characterization

All *J-V* and QE measurements of solar cells in this thesis are performed using the LOANA tool (*PV-tools* GmbH, Germany) [6].

2.2.1 Quantum efficiency (QE)

The quantum efficiency (QE) is defined as the ratio of extracted charge carriers from a solar cell to the amount of irradiated photons of a certain wavelength. In the external quantum efficiency [EQE(λ)] all irradiated photons arriving at the surface of a solar cell are taken into account. For the internal quantum efficiency [IQE(λ)] only the absorbed photons in a solar cell are taken into account:

$$\mathrm{IQE}(\lambda) = \frac{\mathrm{EQE}(\lambda)}{1 - R(\lambda)}, \tag{2.7}$$

where $R(\lambda)$ is the wavelength-dependent reflectance. We do not consider transmittance since all solar cells used in this work have a metal layer covering the entire rear surface.

2.2.2 Current-density voltage characterization (*J-V*)

Solar cell characteristics are measured on a temperature-controlled brass chuck which is used to contact the rear. The front bus bar is contacted by two needles (while the other two contacts are on the rear) to measure the solar cell in the four-point probe method. The *J-V* curve is measured in the dark and under illumination. The illumination is kept constant to acquire a *J-V* plot or is varied to acquire a J_{sc}-V_{oc} plot. Illuminated *J-V* curves are measured at a constant light intensity of 1000 W/m² (also denoted as 'one sun') and at a temperature of 25°C to match STC. The light intensity in our measurement setup is adjusted by using a calibrated reference solar cell, calibrated at the *CalLab* (Fraunhofer ISE in Freiburg, Germany) under STC. The exact AM1.5G spectrum is not realized in the LOANA tool. Differences between our light source and the AM1.5G spectrum are compensated by employing a *spectral mismatch* correction. Hereby, the external quantum efficiency [EQE(λ)] of our solar cell is measured and compared to the EQE(λ) of the reference solar cell. With the knowledge of the EQE(λ) the difference between the known spectra of our light source and the AM1.5G spectrum can be corrected. For the measurement of the J_{sc}-V_{oc} curve, a light source with variable intensity is required. The variable light intensity at different points in time t_i in the LOANA tool is realized by an LED-array, where a family of functions $J_{sc}(V_{oc}(t_i))$ is acquired.

2.3 Dependence of open-circuit voltage on excess carrier concentration $V_{oc}(\Delta n)$

The electron concentration in silicon conduction band is calculated using the following equation:

$$n = \int_{E_C}^{\infty} dE\, D(E) f(E)\,, \tag{2.8}$$

where E is the energy, $D(E)$ is the density of states, $f(E)$ is the Fermi-Dirac distribution and E_C is the conduction band edge. Calculation for holes is performed in a similar way. Assuming that the difference between E_C and the Fermi level E_F is much larger than $k_B T$, the Boltzmann statistics can be applied and the solution of equation (2.8) for the electrons and holes is:

$$n = N_C e^{\frac{(E_{Fn} - E_C)}{k_B T}} \tag{2.9}$$

for the electron density in the conduction band, and

$$p = N_V e^{\frac{(E_V - E_{Fp})}{k_B T}} \tag{2.10}$$

for the hole density in the valence band.

$N_C = 2.8 \times 10^{19}$ cm^{-3} and $N_V = 3.1 \times 10^{19}$ cm^{-3} are the effective density of states in the conduction and valence band, respectively, and E_{Fn} and E_{Fp} are the Quasi-Fermi energies of electrons and holes, respectively. At room temperature and in an excited state (for example due to illumination) $n = n_0 + \Delta n$ and $p = p_0 + \Delta p$, where Δn and Δp are the excess carrier concentrations for electrons and holes, respectively, and n_0 and p_0 are the electron and hole concentration in equilibrium. We assume that no trapping states for charge carriers are present and therefore $\Delta n = \Delta p$. By multiplying the electron and hole concentration we obtain:

$$np = (n_0 + \Delta n)(p_0 + \Delta n) = N_C N_V e^{-E_G/k_B T} e^{(E_{Fn} - E_{Fp})/k_B T} = n_i^2 e^{qV_A/k_B T}. \tag{2.11}$$

V_A is the potential between E_{Fn} and E_{Fp}, $E_G = E_C - E_V$ is the band gap and n_i is the intrinsic carrier concentration. In the case that no current is extracted, V_A is the open-circuit voltage (V_{oc}). After we solve the equation (2.11) for V_{oc} we obtain:

$$V_{oc} = \frac{k_B T}{q} \ln\left(\frac{(n_0 + \Delta n)(p_0 + \Delta n)}{n_i^2}\right). \tag{2.12}$$

Except the extrinsic parameters like temperature, V_{oc} is a function of the excess carrier concentration Δn. To realize high V_{oc} it is important to achieve a high Δn. For further information see [7], [8].

2.4 Recombination channels

The excess carrier density Δn increases with an increasing electron-hole pair generation rate G. The counterpart of the generation rate is the net recombination rate U, which is defined as the total recombination rate R minus the thermal generation rate G_{th}: $U \equiv R - G_{th}$. Recombination is the process where an electron in the conductance band recombines with a hole in the valence band. Furthermore, extraction of charge carriers from the solar cell reduces Δn, which can also be seen from the continuity equation:

$$\frac{\partial \Delta n}{\partial t} = G - R + \frac{1}{q}\mathrm{div}(J)\,. \tag{2.13}$$

Equation (2.13) highlights the importance of the reduction of the recombination rate (besides a high generation rate) which is the limiting factor to achieve a high Δn. In a silicon wafer or solar cell typically all recombination mechanisms occur simultaneously. The dominant recombination channels in silicon solar cells are the intrinsic (radiative and Auger) recombination, Shockley-Read-Hall (SRH) recombination and the recombination at the surfaces.

A useful correlation between Δn and U is the carrier lifetime (τ) defined through the equation:

$$\tau = \frac{\Delta n}{U}\,. \tag{2.14}$$

In following, the lifetimes for different recombination channels are described.

2.4.1 Radiative recombination

In the process of the radiative recombination, the energy set free during one electron-hole recombination event is transferred to a photon. The net recombination rate is proportional to the concentration of electrons and holes $U_{\mathrm{rad}} \propto np$ and the lifetime is hence described by the equation:

$$\tau_{\mathrm{rad}} = \frac{1}{B(n_0 + p_0) + B\Delta n}\,, \tag{2.15}$$

where $B \approx 1 \times 10^{-14}$ cm^3/s [9] is the coefficient of radiation recombination of crystalline silicon. Silicon is an indirect semiconductor and this recombination process is typically not the dominant one.

2.4.2 Auger recombination

In the process of the Auger recombination, the energy set free in a recombination event is transferred to a further carrier, which thermalizes within the conduction or valence band. The recombination rate involves three carriers and the net recombination rate is hence given by $U_{\mathrm{Auger}} \propto n^2 p$ for n-type and $U_{\mathrm{Auger}} \propto p^2 n$ silicon and p-type silicon. The lifetime is described by the equation:

$$\tau_{\mathrm{Auger}} = \frac{1}{c_1 + c_2\Delta n + c_3\Delta n^2}\,. \tag{2.16}$$

For doped silicon ($n_0 + p_0 >> n_i$) are $c_1 = C_n n_0^2 + C_p p_0^2$, $c_2 = C_n n_0 + C_p p_0 + (C_n + C_p)(n_0 + p_0)$, and $c_3 = (C_n + C_p)$, with $C_n = 2.8 \times 10^{-31}$ cm^6/s and $C_p = 9.9 \times 10^{-32}$ cm^6/s [10]. To account the Coulomb-enhanced Auger recombination, the factor C_n is to be replaced with $g_{eeh} \times C_n$ and the factor C_p is to be replaced with $g_{ehh} \times C_p$ [11]. The state-of-the-art parameterization is published by Richter et al. [12], where Auger and radiative recombinations are considered. The intrinsic lifetime τ_{int} is described by the equation:

$$\frac{1}{\tau_{\text{int}}} = \frac{1}{\tau_{\text{rad}}} + \frac{1}{\tau_{\text{Auger}}}. \tag{2.17}$$

2.4.3 Shockley-Read-Hall recombination

In the process of the Shockley-Read-Hall (SRH) recombination an electron in the conductance band recombines with a hole in the valence band via a defect with energy level (E_t) within the silicon band gap. The lifetime is described by the equation:

$$\tau_{\text{SRH}} = \frac{\tau_{p0}(n_0 + n_1 + \Delta n) + \tau_{n0}(p_0 + p_1 + \Delta n)}{p_0 + n_0 + \Delta n}, \tag{2.18}$$

$$n_1 = N_{\text{C}} e^{(E_{\text{t}} - E_{\text{C}})/k_{\text{B}}T} \quad , \quad p_1 = N_{\text{V}} e^{(E_{\text{V}} - E_{\text{t}})/k_{\text{B}}T}, \tag{2.19}$$

where the $\tau_{n0} = (\sigma_n v_{th} N_t)^{-1}$ and $\tau_{p0} = (\sigma_p v_{th} N_t)^{-1}$ are capture time constants for electrons and holes, respectively. N_t is the defect concentration, v_{th} is the thermal velocity and σ_n and σ_p are the capture cross section for electrons and holes, respectively.

2.4.4 Recombination at the surface

One way to describe recombination at the surface is the saturation current density J_0. This nomenclature is often used to describe recombination at electron/hole contact regions. The lifetime for a *p*-type silicon wafer of doping density N_A, thickness W and with the identically fabricated surfaces is then described by the equation [13]:

$$\tau_{\text{S}} = \frac{qWn_i^2}{2J_0(N_{\text{A}} + \Delta n)} \tag{2.20}$$

An alternative description of this recombination channel is the surface recombination velocity S. This quantity is often used to describe recombination in non-contacted regions. For a sufficiently low S [14], the lifetime τ_S is described by the equation:

$$\tau_{\text{S}} = \frac{W}{2S} \tag{2.21}$$

Combining equation (2.20) with (2.21) results in a relation between S and J_0:

$$J_0 = \frac{qn_i^2 S}{N_{\text{A}} + \Delta n}. \tag{2.22}$$

2.4.5 Total lifetime

The total recombination rate is the sum of all recombination rates present. The total lifetime, also referred to an effective lifetime τ_{eff} is hence described by the equation:

$$\frac{1}{\tau_{\text{eff}}} = \frac{1}{\tau_{\text{rad}}} + \frac{1}{\tau_{\text{Auger}}} + \frac{1}{\tau_{\text{SRH}}} + \frac{1}{\tau_{\text{S}}} \tag{2.23}$$

2.4.6 Determination of the saturation current density J_0

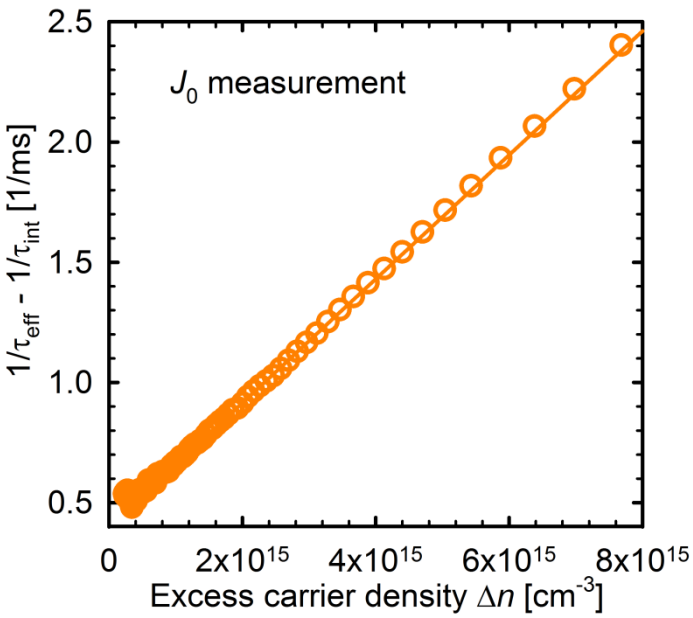

Figure 5: Plotted measured inverse τ_{eff} minus inverse τ_{int} to determine the J_0 value of a lifetime sample after the method of Kane and Swanson [15].

The recombination parameter J_0 is of special interest to the characterization of the electron contact regions and hole contact regions. A widely used method based on effective lifetime measurement to determine J_0 was proposed by Kane and Swanson [15]. This method is applicable if following requirements are fulfilled:

- The base is in high-level injection $\Delta n > N_A$ (here for *p*-type silicon)
- The SRH lifetime is constant at high-level injection $\tau_{SRH} \neq f(\Delta n)$
- The excess carrier lifetime is homogeneously distributed in the bulk $\Delta n = \Delta n_{average}$

Rearranging the equations (2.20), (2.17) and (2.23) we obtain:

$$\frac{1}{\tau_{\text{eff}}} - \frac{1}{\tau_{\text{int}}} = \frac{1}{\tau_{\text{SRH}}} + 2J_0 \frac{(N_A + \Delta n)}{qWn_{\text{i}}^2} \tag{2.24}$$

for a symmetrical lifetime sample where the emitter (described by the J_0) is on both surfaces of the wafer. The intrinsic lifetime τ_{int} is calculated according to the Auger parameterization by Richter et al. [12]. Figure 5 show plotted $1/\tau_{eff} - 1/\tau_{int}$ values as function of Δn. The τ_{eff} values are experimentally measured as function of Δn. A J_0 value of 80 fA/cm² is determined from the slope of the $1/\tau_{eff} - 1/\tau_{int}$ plot in Figure 5.

2.5 Photoconductance-based lifetime measurements

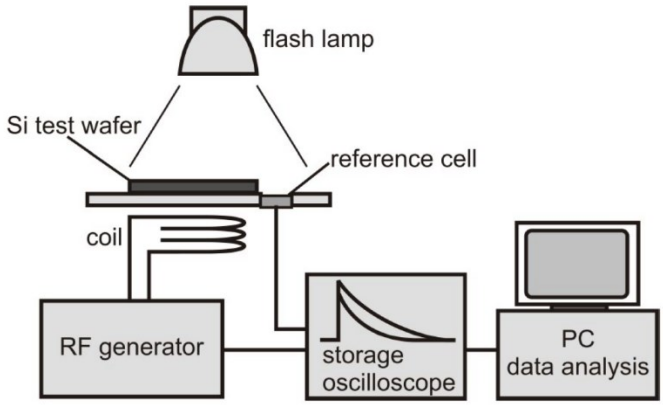

Figure 6: Schematic of the PCD measurement setup (image taken from Ref. [16]).

One lifetime measurement technique predominantly used in this work is based on the photoconductance decay (PCD) method [17]. Figure 6 shows a schematic of the PCD measurement setup developed by Sinton [17]. To perform this measurement, a lifetime sample is placed on a coil, which is part of an RF circuit. The lifetime sample and coil are inductively coupled and the conductivity of the lifetime sample is measured. A flash lamp is positioned above the lifetime sample. A reference solar cell integrated into the measurement equipment monitors the time-resolved illumination intensity during the measurement. A flash lamp illuminates the sample and the reference solar cell simultaneously. The illumination changes the conductivity (σ) of the lifetime sample. To determine the effective lifetime, knowledge of the time dependent excess carrier density (Δn) is required which is a function of σ:

$$\Delta n = \frac{\sigma}{qW(\mu_n + \mu_p)}, \tag{2.25}$$

where W is the wafer thickness, μ_n and μ_p are the mobilities of electrons and holes in silicon, respectively. By rearranging the equations (2.13) and (2.14) and by neglecting lateral current flow div(J) = 0 in the lifetime sample, the effective lifetime can be described by the following equation:

$$\tau_{\text{eff}} = \frac{\Delta n}{G - \partial \Delta n / \partial t}, \tag{2.26}$$

where G is the generation rate within the lifetime sample. G is determined by the measurement of the light intensity with the reference solar cell and by scaling the different optical properties of the reference solar cell and the lifetime sample. By using a 'long' (decay time ~ 2.1 ms [18]) light pulse compared to the decay time of Δn, the measurement is performed in a quasi-steady-state condition, where $\partial \Delta n / \partial t \approx 0$. Equation (2.26) for the quasi-steady-state photoconductance (QSSPC) measurement is hence simplified to:

$$\tau_{\text{eff}} = \frac{\Delta n}{G}. \tag{2.27}$$

By using a 'short' (decay time ~ 30 µs [18]) light pulse compared to the decay time of Δn, the measurement is performed in a transient condition. Hereby, the decay time of Δn exceeds that of the light pulse and therefore $G \approx 0$ can be assumed. Equation (2.26) for the transient measurement is hence:

$$\tau_{\text{eff}} = -\frac{\Delta n}{\partial \Delta n / \partial t}. \tag{2.28}$$

The elegancy of the transient measurement is that only the absolute value of Δn and the derivative of Δn with respect to time is required. The limitation of the transient method is the case where the duration of the decay of Δn is not significantly longer than the duration of the 'short' light pulse. A rule of thumb is a that transient measurement is applicable for lifetimes exceeding ~100 µs. The commercial lifetime-tester used in this work is the WCT-120 [19] (*Sinton Instruments* Inc., USA) which is the standard wafer lifetime tool employed in photovoltaic research today.

2.6 Camera-based lifetime measurement techniques

One disadvantage of the lifetime measurement using the WCT-120 – as described in the previous Section – is the relatively large detection area of a few square centimeters. To obtain spatially resolved lifetime mappings, two camera-based techniques are used in this work.

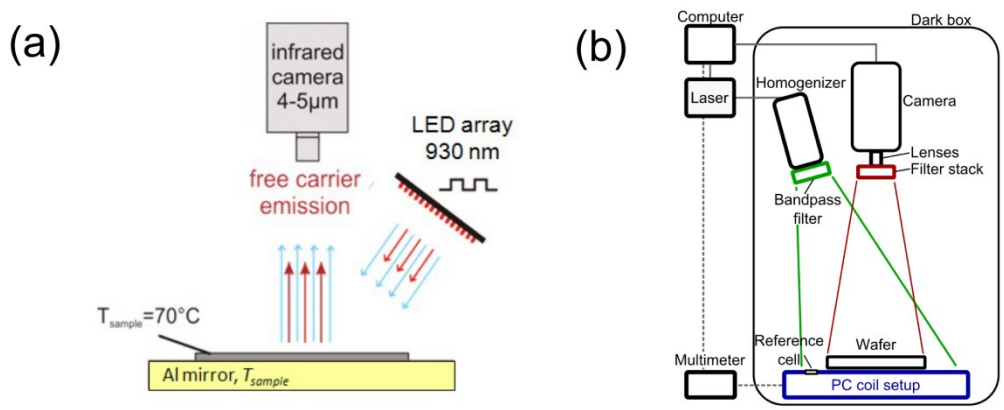

Figure 7: Schematics of the camera-based lifetime measurements setups (a) the infrared lifetime mapping (ILM) (image taken from Ref. [20]) and (b) the photoconductance-calibrated photoluminescence lifetime imaging (PC-PLI) (image taken from Ref. [21]).

2.6.1 Dynamic infrared lifetime mapping (ILM)

Figure 7 (a) shows a schematic of the infrared lifetime mapping (ILM) setup [20]. A lifetime sample is positioned on an aluminum mirror at a temperature of 70°C. The elevated temperature improves the signal-to-noise ratio. An LED array ($\lambda = 930$ nm) periodically generates excess carriers (Δn) in the lifetime sample. An infrared camera positioned above the sample detects the change in the free-carrier emission (λ-range of 4 - 5 µm) that is proportional to the change of Δn. Applying the lock-in technique, the effective lifetime is determined. The dynamic approach of the ILM method does not require calibration. Further details on the method can be found in publication of Ramspeck et al. [20], [22].

2.6.2 Photoconductance-calibrated photoluminescence lifetime imaging (PC PLI)

Figure 7 (b) shows a schematic of the photoconductance-calibrated photoluminescence lifetime imaging (PC-PLI) setup [21]. A lifetime sample is positioned on a coil setup similar to the PCD to calibrate the measurement. An laser beam ($\lambda = 808$ nm) homogenized over the entire lifetime sample excites excess carriers. A Si-CCD camera positioned above the sample detects the band-to-band photoluminescence (PL) radiation. A stack of filters in front of the Si-CCD camera lens blocks the 808 nm excitation wavelength. The detected PL signal can be converted into Δn. The light generation G is measured by the reference solar cell positioned in the coil setup table. The effective lifetime is calculated using the quasi-steady-state approach. Further details on the method can be found in publication of Herlufsen et al. [21], [23].

3 Contact passivation with ALD-AlO_x tunneling layer

In this Chapter, a novel passivation scheme for the metal-semiconductor contact of the n^+-emitter is introduced. The possibility of using ultrathin atomic-layer-deposited (ALD) aluminum oxide (AlO_x) films as tunneling layer for the passivation of solar cell metal contacts is shown for the first time. The advantage of ALD is the thickness control on the atomic layer scale. This precise thickness control is one essential requirement for the formation of a tunneling layer. The ALD-AlO_x tunneling layer is successfully applied to a high efficiency solar cell process. Comparing the solar cell results and the lifetime sample measurements, we determine the effectiveness of the AlO_x contact passivation.

3.1 Experimental details

In this Section, we present fabrication sequence of n^+-emitter and passivation schemes.

3.1.1 n^+-emitter fabrication

The front-surface of a typical solar cell has a non-metallized light-transparent area and a metallized area. The majority of n^+-emitters in the photovoltaic industry are fabricated by a phosphorus diffusion in a quartz-tube furnace [24].

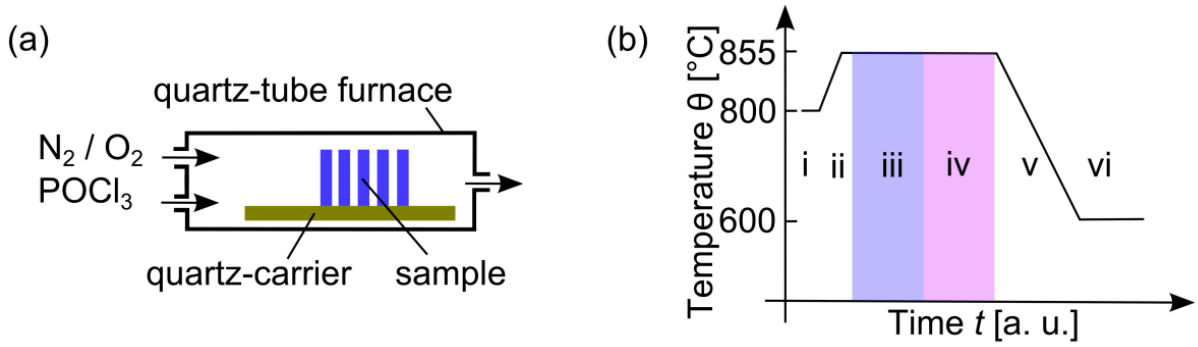

Figure 8: (a) Schematic of a quartz-tube furnace. (b) Temperature profile during a phosphorus diffusion.

Figure 8 (a) schematically shows a cross section of a quartz-tube furnace. The main components are an electrically heated quartz-tube, a quartz-carrier for the sample storage and gas inlets. Figure 8 (b) shows a temperature profile with the corresponding process steps during the n^+-emitter formation sequence. Prior to the diffusion, all samples are RCA-cleaned [25]. In step (i), the silicon samples are loaded into a quartz-carrier and moved to the 800°C pre-heated quartz-tube furnace. A nitrogen flow is maintained during each process step as carrier gas. In step (ii), the furnace is heated up to a temperature of 855°C. In step (iii), oxygen (O_2) and the phosphoryl chloride ($POCl_3$) are injected into the furnace. On the silicon surface, the O_2 and $POCl_3$ react to phosphorus silicate glass (PSG) which is the source of phosphorus during the diffusion. In step (iv), the O_2 and $POCl_3$ injection is stopped and phosphorus continues to diffuse from the PSG into the silicon surface and forms the n^+-emitter. In step (v), the temperature is reduced to $\theta = 600$°C and in step (vi), the samples are unloaded at $\theta = 600$°C

from the furnace. Figure 9 (a) shows an n^+-emitter profile with a sheet resistance of ~100 Ω/□ as typically used in this work. The emitter profile shows the electrically active phosphorus-atom concentration as function of the depth from the silicon surface. The measurement is performed with an electrochemical capacitance voltage (ECV) profilometer (WEP, Wafer Profiler *CVP21*). Figure 9 (b) shows a scanning electron microscopy (SEM) image of a RP-textured front surface of a solar cell with a phosphorus-diffused n^+-emitter. In the SEM image, the n^+-emitter appears darker compared to the *p*-type base, as a result of the work-function difference between the base and the n^+-emitter.

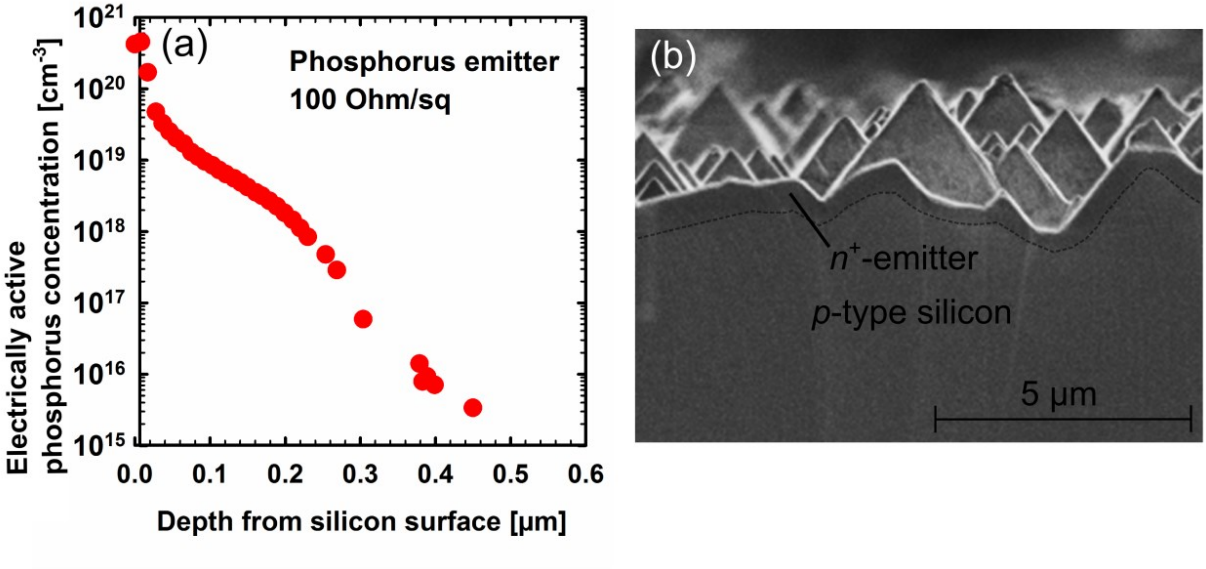

Figure 9: (a) Phosphorus-diffused n^+-emitter profile with a sheet resistance (R_{sh}) of ~100 Ω/□ as typically used in this work. (b) Scanning electron microscopy (SEM) image of a RP-textured front surface of a solar cell with a phosphorus-diffused n^+-emitter. In the SEM image, the n^+-emitter appears darker compared to the *p*-type base. Black-dotted line indicates the boundary between *p*-type base and n^+-emitter.

3.1.2 Passivation schemes

A well passivated silicon surface is a necessary prerequisite for a highly efficient solar cell. The surface passivation is frequently realized by the deposition of an amorphous dielectric layer on the silicon surface. The deposited dielectric layer has two purposes: (i) saturation of dangling bonds ('*chemical*' passivation) and (ii) repulsion of one carrier type from the silicon surface ('*field-effect*' passivation). Repulsion of the carriers is realized by the fixed charge density within the dielectric layer. Silicon nitride layers contain e.g. fixed positive charges while aluminum oxide has a fixed negative charge density. In this Section, deposition of passivating silicon nitride and aluminum oxide layers will be discussed.

3.1.2.1 Plasma-enhanced chemical vapor deposition (PECVD) of silicon nitride (SiN_x)

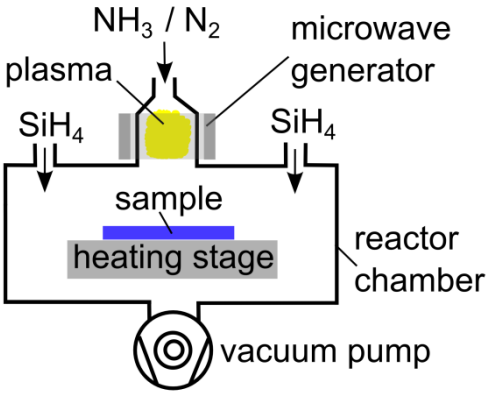

Figure 10: Schematic of microwave-remote plasma-enhanced chemical vapor deposition (PECVD) chamber for silicon nitride (SiN_x) deposition.

Figure 10 shows a schematic of a microwave-remote plasma-enhanced chemical vapor deposition (PECVD) reactor as used in this work (Oxford Instruments, *Plasmalab 80+*). NH_3/N_2 gas mixture is ionized by a microwave generator with a power $P = 150$ W in a quartz-tube above the process chamber with a frequency $f = 2.455$ GHz. SiH_4 flows separately into the process chamber. NH_3 ions react with SiH_4 molecules within the reactor chamber to amorphous SiN_x and H_2. Through the ratio of SiH_4/NH_3 the amount of nitrogen in the deposited silicon nitride films can be adjusted. The ratio is a crucial factor to the performance of the SiN_x layers. In photovoltaics, there are two basic functions of the SiN_x layers: (i) as an anti-reflectance-coating (ARC) and (ii) as a surface passivating layer.

(i) Antireflecting properties of SiN_x

The optimal refractive $n_{\mathrm{ARC_optimal}}$ index for a single-layer ARC coating is calculated using the following equation:

$$n_{\mathrm{ARC_optimal}} = \sqrt{n_{\mathrm{Si}} \times n_{\mathrm{air}}} = \sqrt{3.6 \times 1} = 1.9.$$

A single-layer ARC with a refractive index $n \approx 1.9$ can be realized using stoichiometry SiN_x layers with $n = 1.9$ show further a low parasitic light absorption and is optimal for anti-reflection coating applications. Unfortunately, SiN_x with $n = 1.9$ provides typically a relatively poor passivation of a silicon surface.

(ii) Surface-passivating properties of SiN_x

A SiN_x film with a refractive index of $n \approx 2.4$ shows excellent passivation properties [26], [27]. SiN_x layers with a refraction index of $n \approx 2.4$ can be realized by a SiN_x layer with an increased silicon content.

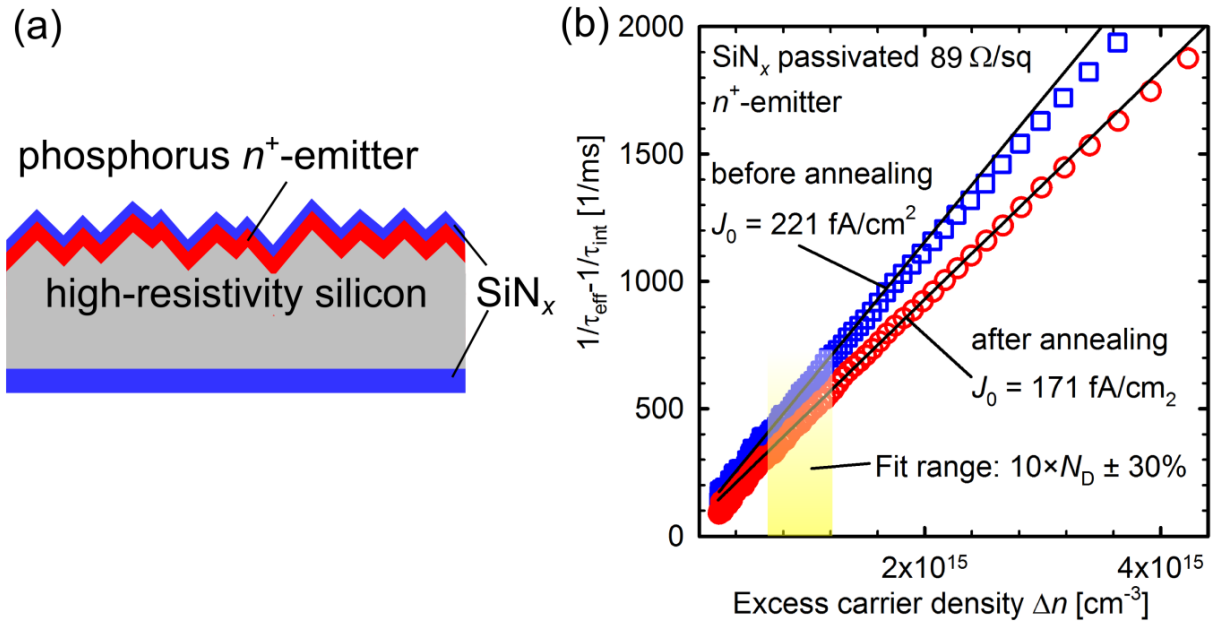

Figure 11: (a) Schematic of an asymmetrical saturation current density J_0 sample. (b) Inverse effective lifetime $1/\tau_{eff}$-$1/\tau_{int}$ as a function of the excess carrier density Δn of a representative J_0 sample before (blue squares) and after (red circles) annealing at 350°C in air for 2 mins. The black lines show linear fits in the Δn range from 6.7×10^{14} cm^{-3} – 1.2×10^{15} cm^{-3} (yellow area).

Figure 11 (a) shows a schematic of an asymmetrical saturation current density J_0 sample. The J_0 value within this test structure represents the saturation current density of the non-metallized front surface of our solar cell. We start with a high-resistivity (~150 Ωcm) boron-doped 300 µm thick float-zone (FZ) silicon wafer. The wafer is laser-cut into five equally processed 2.5 × 2.5 cm² samples. After RCA cleaning, a SiN_x (n = 1.9 at λ = 632 nm) protection layer is deposited onto the entire rear surface. The protection layer prevents the later texture and diffusion. Next, the front surface is random-pyramid-textured in a KOH/2-propanol solution. After RCA cleaning, an n^+-emitter is formed in a quartz-tube furnace. Next, the phosphorus silicate glass (PSG) is removed in a 5% dilute HF solution for 1 hour. After an additional RCA cleaning the rear surface is passivated by a 100 nm PECVD-SiN_x layer (n = 2.4 at λ = 632 nm) at a temperature of 400°C. Then, the front surface is passivated by a PECVD-SiN_x double-layer consisting of a 10 nm thick well passivating layer (n = 2.4 at λ = 632 nm) and a 70 nm thick layer (n = 1.9 at λ = 632 nm) at a temperature of 330°C. The 70 nm SiN_x layer (n =1.9 at λ = 632 nm) serves as the ARC in our solar cell architecture.

Figure 11 (b) shows the measured inverse effective lifetime $1/\tau_{eff}$ minus inverse intrinsic lifetime $1/\tau_{int}$ as a function of the excess carrier density Δn of a representative sample before (blue squares) and after (red circles) annealing at 350°C for 2 mins. The saturation current density J_0 is extracted using the method proposed by Kane and Swanson [15] (see Section 2.4). A linear fit is performed within the fit range of $10 \times N_D \pm 30\%$ [15], [28], which is in our case : 6.7×10^{14} cm^{-3} – 1.2×10^{15} cm^{-3} for $N_D = 8.9 \times 10^{13}$ cm^{-3}. The average J_0 has a value of (221 ± 19) fA/cm^2 and (171 ± 47) fA/cm^2 before and after annealing, respectively. Assuming a realistic J_{sc} value of 40 mA/cm^2, we calculate an ideal open-circuit voltage [equation (2.4)] V_{oc_ideal} = (666 ± 2) mV and (673 ± 10) mV for cells before and after annealing, respectively. By annealing, the V_{oc_ideal} increases by 7 mV. In addition, using the WCT-120 tool, an average emitter sheet resistance of R_{sheet} = (89 ± 9) Ω/□ was determined.

3.1.2.2 Atomic layer deposition (ALD) of aluminum oxide (AlO_x)

Aluminum oxide (AlO_x) deposited by atomic layer deposition (ALD) receives high interest for photovoltaic applications due to its unique homogeneity, its precise thickness control on atomic scale and its high level of surface passivation on *p*- and *n*-type crystalline silicon (c-Si) wafers, as determined from carrier lifetime measurements [29], [30], [31], [32]. On device level, an excellent ALD-AlO_x rear side passivation of *p*-type c-Si PERC was demonstrated [33], [34]. The excellent passivation property of ALD-AlO_x originates from the high fixed negative charge density of $Q_f = -(4 \pm 1) \times 10^{12}$ cm^{-3} [32] and a low midgap interface defect density of $D_{it_midgap} = (2 \pm 1) \times 10^{11}$ eV^{-1}cm^{-2} [32].

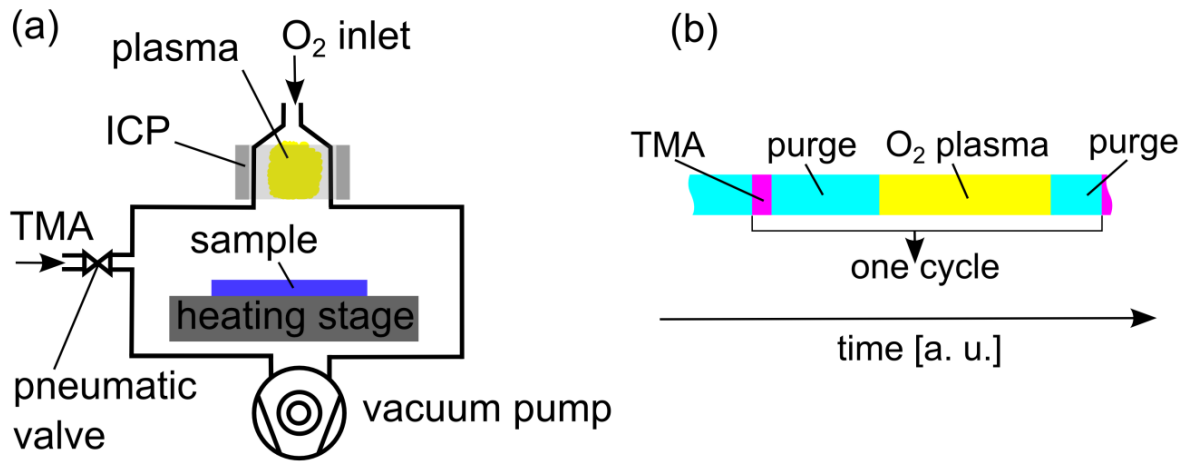

Figure 12: (a) Schematic of a plasma-assisted (PA) atomic layer deposition (ALD) reactor chamber for AlO_x deposition. (b) PA-ALD process sequence.

ALD is a cyclic deposition process, whereby the ALD of AlO_x consists of two half-reactions. Figure 12 (a) shows a schematic of a plasma-assisted (PA) ALD reactor chamber for AlO_x deposition. The vacuum in the process chamber is maintained by a turbo molecular pump. The metal-organic precursor tri-methyl-aluminum [TMA with the chemical structure $Al(CH_3)_3$] is dosed by a pneumatic valve. O_2 plasma is generated remotely by an inductively coupled plasma (ICP) source. After each precursor injection the chamber is purged with oxygen. During the entire deposition process the sample is positioned on a heated stage.

Figure 12 (b) shows schematically one cycle of the PA-ALD of AlO_x consisting two half reactions. Each one is a self-limiting reaction. In the first half-reaction, the silicon surface is exposed to the TMA precursor. TMA molecules react with the OH-terminated silicon surface but not with the other TMA molecules. That allows the growth of only one monolayer. Please note that one methyl group is removed during the oxidation process. A saturation occurs when one monolayer of $Al[CH_3]_2$ covers the surface. In the second half-reaction, the $Al[CH_3]_2$-saturated surface is exposed to the plasma-ionized oxygen which removes the residual methyl groups and oxidizes the aluminum. After each half-reaction the residual reactants are purged with oxygen. Two half-reactions result in one monolayer of AlO_x. The final AlO_x thickness is determined by multiplying the number of cycles with the growth-rate per cycle (GPC). For our plasma-assisted ALD setup (Oxford Instruments, FlexAl™) the GPC is 0.12(1) nm [35]. Note that all passivating layers applied in this work have an amorphous structure. To achieve an excellent surface passivation, annealing at 425°C for 15 mins is performed [35].

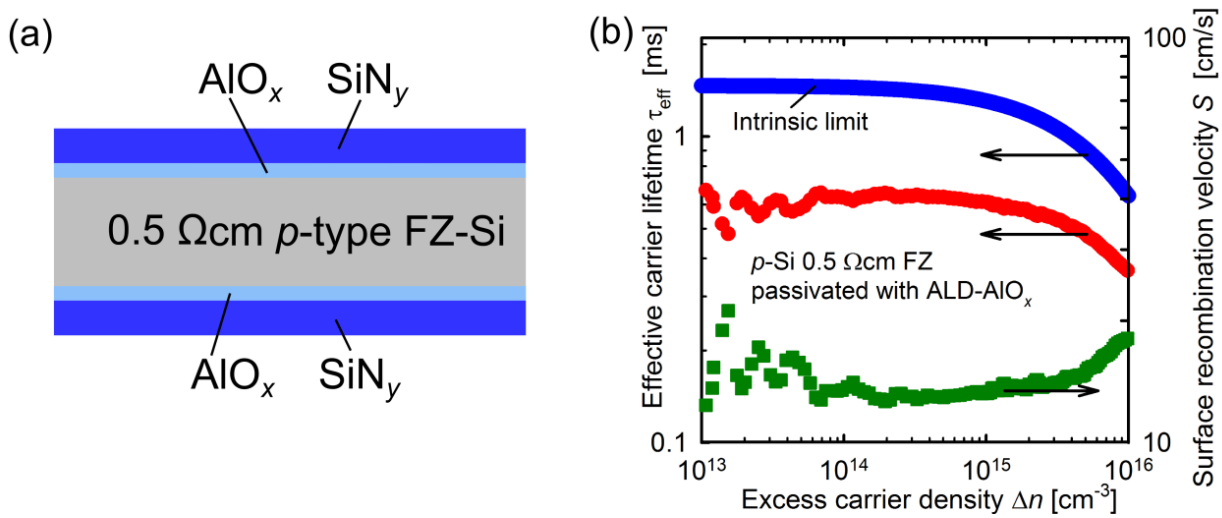

Figure 13: (a) Schematic of a symmetrical lifetime sample. (b) Measured effective lifetimes τ_{eff} as a function of the excess carrier density Δn (red circles) and calculated surface recombination velocity (green squares). The blue symbols show the intrinsic lifetime according to the parameterization of Richter et al. [12].

Figure 13 (a) shows symmetrical lifetime samples. Boron-doped float-zone (FZ) silicon wafers with a resistivity of 0.5 Ωcm and a thickness of 300 µm are used as base material. After RCA cleaning, both surfaces are passivated by a 30 nm ALD-AlO$_x$ layer. After deposition, the samples are annealed at 425°C for 15 min. After annealing, a 100 nm PECVD-SiN$_x$ layer [n = 2.05 at λ = 632 nm] is deposited at a temperature of 400°C on both surfaces.

Figure 13 (b) shows the measured effective lifetime τ_{eff} and calculated intrinsic lifetime τ_{int} [12] for the FZ-Si and the calculated surface recombination velocity S of a symmetrical AlO$_x$/SiN$_y$ lifetime sample. For the AlO$_x$/SiN$_x$ lifetime sample we measure a τ_{eff} = 630 µs at Δn of 1×10^{15} cm^{-3}. Based on measured τ_{eff} and a τ_{int} value of 1300 µs (according to the parametrization given in Ref. [12]) and using the equation:

$$S = \frac{W}{2}\left(\frac{1}{\tau_{\mathrm{eff}}} - \frac{1}{\tau_{\mathrm{int}}}\right) \tag{3.1.2.1}$$

we determine an S value of 14 cm/s. The τ_{eff} and consequently S are quite constant over the Δn range between 1×10^{13} (approximately J_{sc} condition) to 1×10^{15} cm^{-3} (approximately V_{oc} condition) which is the typical operating range of our solar cells. Consequently, we can use this determined S value for the entire solar cell operation range. Note that the equation (3.1.2.1) is an approximation for sufficient low S values [14].

3.2 Solar cells with AlO_x tunneling contacts

In this work, the thermally grown SiO_x tunneling layer traditionally used in MIS-n^+p solar cells [36], [37] is substituted by an ALD-AlO_x tunneling layer with its precise thickness control at the sub-nanometer scale. To mention is the starting ALD cycle that considerably differs from the later cycles described above. For the formation of an AlO_x tunneling layer, we start with the oxidation of the surface using the O_2 plasma followed by the TMA exposure. With increased cycle numbers, the aluminum content increases rapidly and saturates at a stoichiometric Al:O ratio of 2:3 [32]. In this work, we denote AlO_x and Al_2O_3 for layers with a thickness of less than 2 nm and more than 2 nm, respectively. Interestingly, the high oxygen-to-aluminum ratio at the AlO_x/c-Si interface is probably one important part of the formation of the high negative charge density within the ALD-AlO_x layers [31]. The high negative charge density is one major reason for the excellent passivation properties of ALD-AlO_x layers.

Werner et al. [32] showed a non-stoichiometric growth during the first ALD-AlO_x cycles. Prior to the ALD deposition, a native silicon oxide layer of ~1 nm was measured on the silicon surface. Therefore, we assume the final AlO_x layer thickness equals 1 nm SiO_x plus 0.12(1) nm AlO_x × amount of ALD cycles. For simplicity, we mention only the AlO_x layer with a thickness corresponding to the number of ALD cycles. In the following, we apply ALD-AlO_x with a varying thickness between the phosphorus-diffused n^+-emitter and the metal contact of our laboratory-scale PERC solar cells.

3.2.1 Experimental details

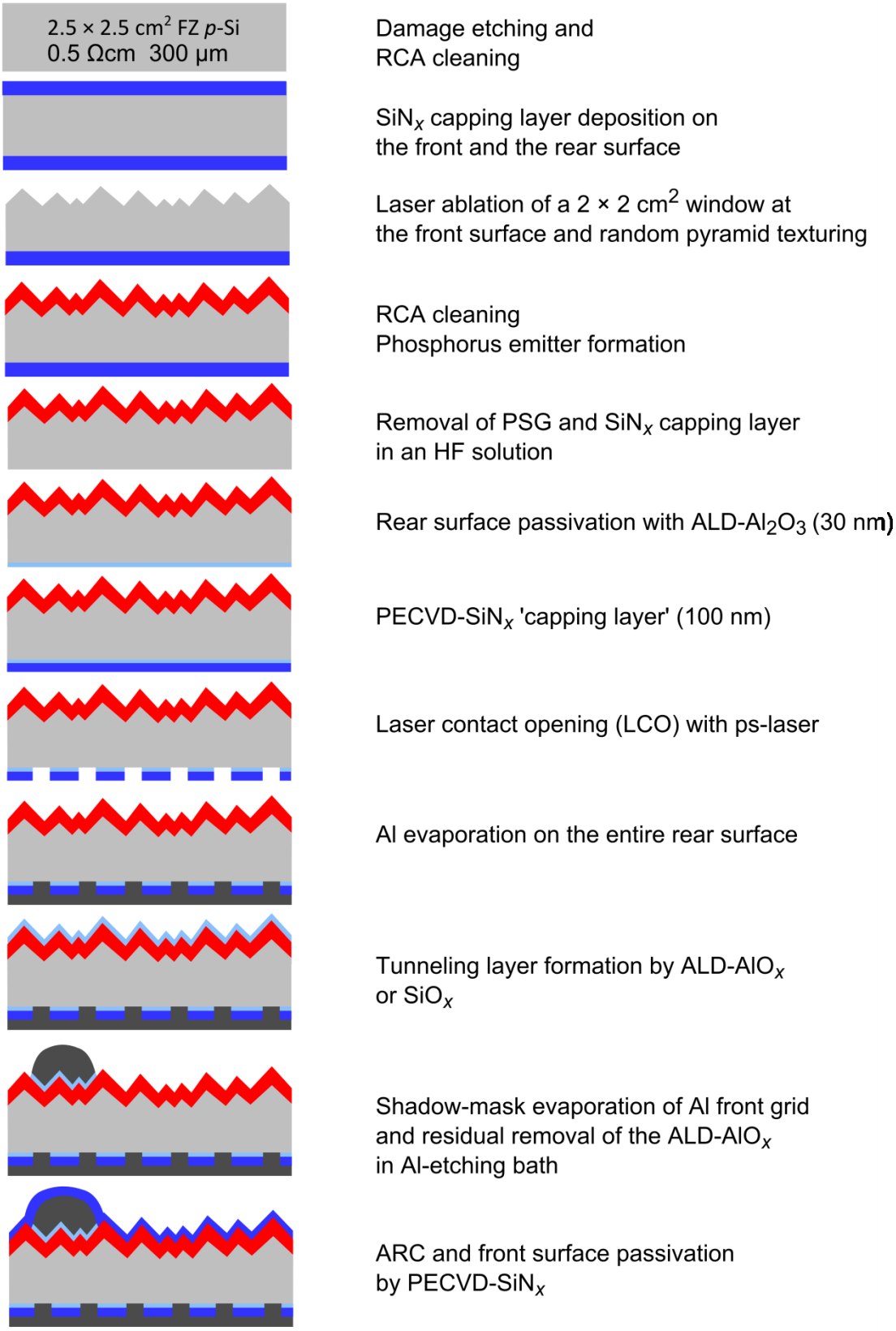

Figure 14: Process-flow diagram of our passivated emitter and rear cell (PERC) solar cell with AlO_x tunneling contact.

Figure 14 shows the process-flow diagram of our PERC devices with implemented AlO_x tunneling layer between the n^+-emitter and the Al front contact grid. We start with a (100)-oriented boron-doped float-zone (FZ) silicon wafer with a resistivity of 0.5 Ωcm and an initial thickness of 300 µm. After damage etching in a KOH solution and standard RCA cleaning, a 100 nm thick SiN_x protection layer (refractive index $n = 1.9$ at a wavelength $\lambda = 632$ nm) is deposited on both surfaces by plasma-enhanced chemical vapor deposition (PECVD, Roth & Rau SiNA). After SiN_x deposition, a 2×2 cm^2 window is opened by laser ablation ($\lambda = 532$ nm, pulse duration 9 ps, frequency-doubled Nd:YVO_4 SuperRapid Lumera Laser GmbH). The laser-ablated side defines the front side. Next, the front surface is random-pyramid-textured in a KOH/2-propanol solution. KOH-damage etching and texturing reduces the final wafer thickness to a value of 275 µm. After texturing, an n^+-emitter with a sheet resistance of (100 ± 4) Ω/□ is formed in a quartz-tube furnace at 855°C in a $POCl_3/O_2$ atmosphere. Next, the PSG and the SiN_x protection layers are removed in a diluted hydrofluoric acid (HF) solution. Subsequently, we passivate the rear surface with a 30 nm thick ALD-Al_2O_3 layer in a lab-type ALD reactor (FlexAL™, Oxford Instruments). Subsequently, a 100 nm thick PECVD-SiN_x capping layer [$n = 2.05$ at $\lambda = 632$ nm] is deposited at 400°C in a microwave-remote PECVD reactor (Oxford Instruments, Plasmalab 80$^+$) on the Al_2O_3 layer. Next, we locally open the Al_2O_3/SiN_x stack at the rear by ps-laser ablation. The opening geometry consists of squares with a size of 420 × 420 µm² rectangularly arranged with a pitch of 2.1 mm and an totally opened area of 4%. After a standard RCA cleaning with a short HF dip of ~15 sec (to prevent a substantial etch off of SiN_x), we deposit a 10 µm thick aluminum layer on the entire rear side by electron beam evaporation (BAK 600, Oerlikon Balzers AG). Subsequently, the cell batch is split into several groups, where AlO_x tunneling layers with nominal thicknesses between 0 and 0.96 nm are deposited on the n^+-emitter layer using plasma-assisted ALD. Thermally grown SiO_x tunneling layers are formed as a reference in a quartz-tube furnace at 500°C in O_2 atmosphere [36]. After the tunneling layer formation, a 20 µm thick Al grid is evaporated through a nickel shadow mask by electron-beam evaporation (BAK 600, Oerlikon Balzers AG). After evaporation, a short ~8 sec dip in a 70°C Al-etching bath [25 : 5 : 1; H_3PO_4 (85%) : CH_3COOH (100%) : HNO_3 (70%)] is performed in order to remove residual aluminum. During Al-etching, the AlO_x layer on the non-metallized area is removed. Note that under the Al front metal grid the AlO_x layer is not affected. Finally, we deposit a microwave-remote PECVD-SiN_x anti-reflection coating (ARC) at 300°C consisting of a 10 nm thick Si-rich SiN_x layer [$n = 2.4$ at $\lambda = 632$ nm] and a 70 nm thick stoichiometric SiN_x layer [$n = 1.9$ at $\lambda = 632$ nm] on the entire cell front.

3.2.2 Solar cell results and discussion

The illuminated current density - voltage (*J-V*) characteristics are measured under a diode array field at 100 mW/cm² at a temperature of 25°C with a commercial tool LOANA (*pv-tools* GmbH, Hameln). The solar cell results denoted by an asterisk (*) have been independently confirmed under standard testing conditions at Fraunhofer ISE CalLab (Freiburg, Germany). Table 2 summarizes the measured solar cell parameters with a thermally grown SiO_x tunneling layer with a thickness of ~1.5 nm [36] as reference process and an ALD-AlO_x layer with a nominal thickness ranging between 0 and 0.96 nm. The results are provided for solar cells before and after annealing. Median values, annealing times and standard deviations among equally processed solar cells are also provided. Annealing was performed on a hot plate in air at a temperature of 350°C. The optimal annealing time differs for different AlO_x layer thicknesses. For each cell batch of the same AlO_x layer thickness, the annealing time was successively raised until degradation in cell efficiency occurred, to determine the optimal annealing time. The annealing time where the maximum efficiency values were measured is given in Table 2.

Table 2: Measured parameters of PERC solar cells with thermally grown SiO_x and ALD-AlO_x tunneling layers with nominal thicknesses of 0, 0.12 (1 cycle), 0.24, 0.48 and 0.96 nm. For each AlO_x thickness the best results are presented before and after annealing at 350°C for 1-13 min. The median of all cells, the standard deviation (s. d.) and the annealing times are also provided. The aperture cell area is 4 cm². The cell parameters denoted by an asterisk (*) have been independently confirmed at Fraunhofer ISE CalLab (Freiburg, Germany).

SiO_x / ALD cycles		Annealing time [min]	V_{oc} [mV]	J_{sc} [mA/cm²]	*FF* [%]	η [%]
SiO_x	best cell	0	662	38.5	80.0	20.4
SiO_x	best cell	1	674	40.3	77.7	21.1
SiO_x	med. + s. d. of 4	0	659 ± 3	39.0 ± 0.1	76.9 ± 2.3	19.8 ± 0.7
SiO_x	med. + s. d. of 2	1	673 ± 1.4	40.3 ± 0	76.4 ± 1.2	20.7 ± 0.4
-	best cell	0	652	40.4	78.4	20.7
-	best cell	1	661	40.6	78.5	21.1
-	med. + s. d. of 7	0	646 ± 58	40.1 ± 0.1	69.1 ± 15.7	17.9 ± 4.9
-	med. + s. d. of 7	1	653 ± 124	40.0 ± 0.3	66.0 ± 17.9	17.5 ± 6.2
1	best cell	0	665	40.1	79.1	21.1
1	best cell	1	673	40.5	79.3	21.6
1	med. + s. d. of 6	0	662 ± 3	39.9 ± 0.8	78.5 ± 9.3	20.6 ± 2.7
1	med. + s. d. of 6	1	669 ± 1.5	40.4 ± 0.5	78.7 ± 9.2	21.3 ± 2.6
2	best cell	0	666	40.1	79.3	21.2
2	best cell	4	673*	40.3*	79.9*	**21.7***
2	med. + s. d. of 6	0	660 ± 3	39.9 ± 0.2	79.0 ± 1.1	20.6 ± 0.4
2	med. + s. d. of 6	4	672 ± 1	40.3 ± 0.1	79.6 ± 0.7	21.5 ± 0.2
4	best cell	0	661	40.1	64.7	17.1
4	best cell	10	674	40.4	73.9	21.1
4	med. + s. d. of 4	0	664 ± 2	39.9 ± 0.1	53.7 ± 4.6	14.2 ± 1.2
4	med. + s. d. of 4	10	673 ± 1	40.4 ± 0.1	73.5 ± 0.5	19.8 ± 0.1
8	best cell	0	658	9.7	23.4	1.50
8	best cell	13	672	40.8	77.5	21.3
8	med. + s. d. of 2	0	659 ± 1	8.8 ± 0.8	24.2 ± 0.8	1.4 ± 0.1
8	med. + s. d. of 2	13	673 ± 0.8	40.8 ± 0.1	72.7 ± 4.8	20.0 ± 0

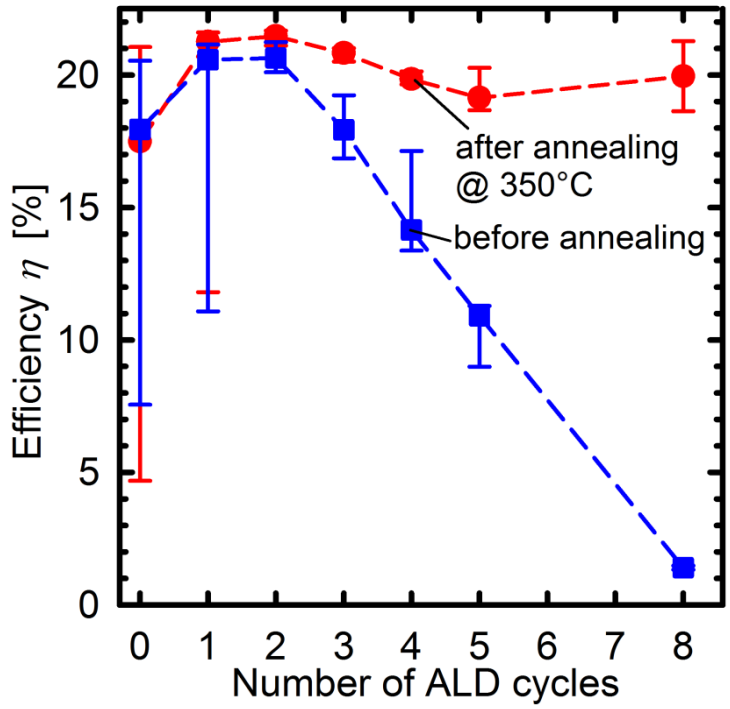

Figure 15: Median solar cell conversion efficiencies (η) for all solar cells before (blue symbols) and after (red symbols) annealing as a function of the number of ALD cycles. The error bars are defined by the maximal and minimal measured efficiencies. Dashed lines are guide-to-the-eye.

Figure 15 shows median solar cell conversion efficiencies (η) for all solar cells before and after annealing as a function of the number of ALD cycles. The uncertainty range is defined by the maximal and minimal measured efficiencies. The highest solar cells conversion efficiencies (η) before annealing are 21.1% and 21.2% for an AlO_x layer deposited by one and two ALD cycles, respectively, corresponding to nominal AlO_x thickness values of 0.12 nm and 0.24 nm (i.e. excluding the interfacial SiO_x thickness as previously discussed). The highest η before annealing for a solar cell with thermally grown SiO_x layer is 20.6%. The thermally grown SiO_x layer has a thickness of ~1.5 nm [36]. After annealing all median solar cell efficiencies increase except for the solar cells without a tunneling layer. After annealing we achieved our record efficiency of 21.7% for a solar with a 2-cycle ALD-AlO_x tunneling layer. Note that our record solar cell was independently confirmed by ISE CalLab. The η gain after annealing increases with an increasing number of ALD cycles. The η gain is $0.9\%_{abs}$ for 2 cycles ALD and $18.5\%_{abs}$ (!) for 8 cycles ALD. This tremendous increase in efficiency for 8 cycles might be explained by Al spike through the AlO_x layer during annealing, enabling an electrical contact to the n^+-emitter. The risk is that Al also spikes through the n^+-emitter during annealing leading to a shunt. Nevertheless, the highest median efficiency and the highest efficiency were achieved with a solar cell made with a ALD-AlO_x tunneling layer formed by two cycles of ALD-AlO_x [38], [39].

The short-circuit current density J_{sc} shows the weakest dependence on the tunneling layer thickness. This fact is not surprising since a transparent ultrathin layer has practically no influence on the optical properties of the solar cell. Before annealing, the J_{sc} value of nearly all solar cells has a median value between 39.9 and 40.1 mA/cm^2. The only exception are cells with a 0.96 nm thick AlO_x layer where a median J_{sc} of 8.8 mA/cm² was measured before annealing due to a large series resistance R_{s_dlt} of 53.5 Ωcm². Measurements of R_{s_dlt} were performed using the double-light method [40]. For thermally grown SiO_x-passivated solar cells we obtain a median J_{sc} value of 39.0 mA/cm². After annealing the median J_{sc} value exceeds 40 mA/cm² for all solar cells.

Figure 16 (a) shows the fill factor (*FF*) for all solar cells before and after annealing as a function of the number of ALD cycles. The uncertainty range is defined by the maximal and minimal measured fill factors. The solar cells with a tunneling layer deposited by two ALD cycles show the highest median *FF* value of 79% (among 6 equally processed cells). Furthermore, these solar cells show better reproducibility with a standard deviation of only 1.1%$_{abs}$ (among 6 cells). For an AlO_x layer deposited by less than two ALD cycles we observe decreasing median *FF* values and an increased scattering of the *FF* values. We obtain a median *FF* of 78.5% (among 6 cells) and 69.1% (among 7 cells) for one cycle and 0 ALD cycles, respectively, and a standard deviation of ±9.2%$_{abs}$ and ±15.7%$_{abs}$ for one cycle and 0 ALD cycles, respectively. The large scattering in *FF* with an AlO_x layer less than 0.24 nm for cells before annealing is most likely caused by aluminum spiking during the anti-reflection-coating SiN_x deposition at 300°C for ~ 6 mins on the front side. Additional thermal treatment during the post fabrication annealing increases the probability of aluminum spiking and therefore the scattering in efficiency. Figure 17 shows an scanning electron microscopy (SEM) image of an evaporated Al layer on a planar silicon bulk without a tunneling layer. The SEM image shows two inverted pyramid-shaped Al spikes. The Al-spike formation occurs during post-fabrication annealing at 350°C. A relatively shallow (thickness of ~400 nm) 100 Ω/□ n^+-emitter as typically implemented in this work would be severely shunted by such Al spiking formation.

For solar cells with an AlO_x layer larger than 0.24 nm the solar cell efficiency before annealing decreases significantly with increasing AlO_x layer thickness, caused by an increasing *FF*. The decrease in *FF* with increasing AlO_x layer thickness is likely caused by a reduced tunneling probability through the AlO_x layer and therefore an increasing series resistance. Solar cells with thermally grown SiO_x layer have a 2%$_{abs}$ lower *FF* value of 76.7% compared to a cell with an optimal ALD-AlO_x thickness.

After optimal annealing, the *FF* and therefore the efficiency of cells with an AlO_x layer thicker than 0.24 nm are improved, which can be attributed to a decrease in series resistance R_{s_dlt}. For cells with an AlO_x layer of 0.24 nm before annealing we obtain an R_{s_dlt} of (1.1 ± 0.1) Ωcm² and for cells with an 0.34 nm AlO_x layer an R_{s_dlt} of (4.1 ± 0.9) Ωcm². After annealing we obtain for cells with an AlO_x layer of 0.24 nm an R_{s_dlt} of (1.0 ± 0.1) Ωcm² and for cells with an 0.34 nm AlO_x layer an R_{s_dlt} of (1.7 ± 0.2) Ωcm².

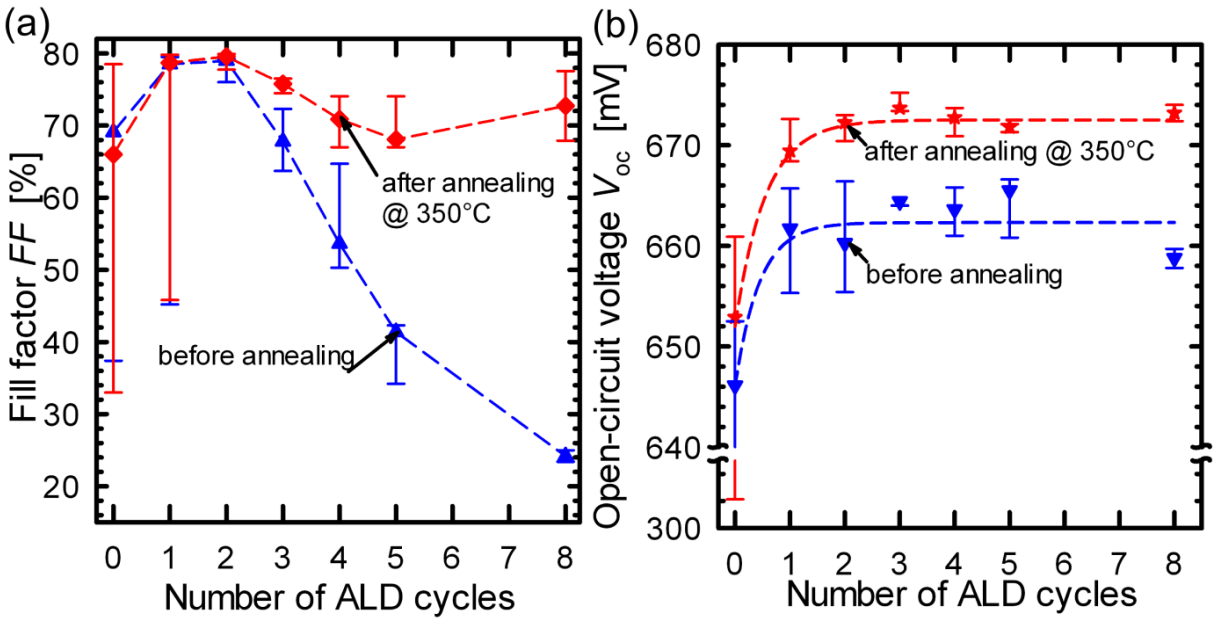

Figure 16: Median (a) fill factor (*FF*) and (b) open-circuit voltages (V_{oc}) for all cells before (blue symbols) and after (red symbols) annealing as a function of the numbers of ALD cycles.

Figure 16 (b) shows the median open-circuit voltages V_{oc} of all cells before and after annealing. The uncertainty range is defined by the maximal and minimal measured V_{oc} values. Before annealing a low median V_{oc} of 646 mV (median of 7 cells) with a very large scatter of ±58 mV is achieved for cells without AlO_x tunneling layer. After applying an AlO_x layer deposited by only one ALD cycle we achieve a clearly higher median V_{oc} of 662 mV (6 cells) and a clearly reduced scatter of ±3.4 mV. A further increase in AlO_x layer thickness has no significant effect on the V_{oc} due to an apparent saturation of the passivation quality under the aluminum contacts. Comparing the median V_{oc} values of the solar cells with 0 and 2 cycles of ALD-AlO_x we observe an improvement of 14 mV. This result shows a clear passivation effect of our optimal ALD-AlO_x layer.

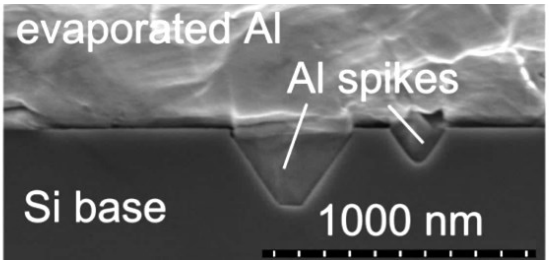

Figure 17: SEM-image of an evaporated Al layer on a silicon surface. Al spikes are visible as inverted pyramid-shaped structures penetrating the silicon surface.

Annealing at 350°C improves the median V_{oc} of all solar cells by 7 - 12 mV. This effect can be partially attributed to an improved passivation of the non-metallized emitter area (Chapter 3.1.2.1) where an improvement of 7 mV was determined.

The AlO_x layers show a clear passivation effect due to significantly higher V_{oc} values of 668 mV to 675 mV of all 24 solar cells with an AlO_x layer compared to V_{oc} values of 321 mV to 661 mV of all 7 solar cells without AlO_x layer. The highest efficiency of (21.7 ± 0.4)%, independently confirmed at Fraunhofer ISE CalLab, was achieved for a solar cell with a 0.24 nm thick AlO_x layer.

For a decreasing solar cell volume the surface recombination becomes more dominant. We implemented our optimal ALD-AlO_x layer deposited by 2 cycles in a 43 µm-thin PERC solar cell. The achieved solar cells efficiency of 19.1% [41] was at that time the world record for a thin-film transfer solar cell [42].

To determine the shunt resistance R_{sh} and the saturation current density J_{0_total} of all cells without AlO_x layer and with 0.24 nm thick AlO_x layer, we fit a one-diode model [equation (2.2.)] to the measured *J-V* curves shifted by J_{sc} into the fourth quadrant. Thereby, R_s is the series resistance obtained from double-light measurements [40], V_T = 25.69 mV is the thermal voltage and $J_{ph} \approx J_{sc}$ is the photo-generated current density obtained from the *J-V* curve. Furthermore, the ideality factor of the solar cell is assumed to be 1. Figure 18 shows an example of a semi-logarithmic plot of the measured one-sun *J-V* curves and model fits for a typical solar cell from the batch without tunneling layer (circles) and for an 0.24 nm thick AlO_x tunneling layer (squares) deposited using two ALD cycles before (blue symbols) and after (red symbols) annealing at 350°C.

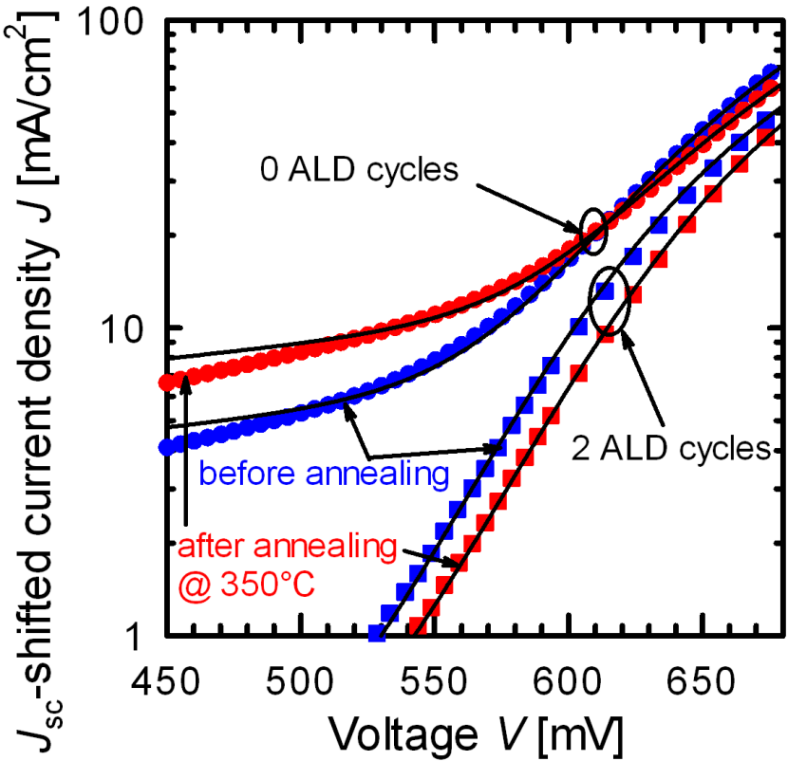

Figure 18: J_{sc} - shifted *J-V* curves of a solar cell without tunneling layer (circles) and with a AlO_x tunneling layer (squares) deposited by two ALD cycles before (blue symbols) and after (red symbols) annealing. Black lines show fit to the measured data.

The analysis of the shifted *J-V* curves reveals an shunt resistance R_{sh} between 1.3 kΩcm^2 and 4.1 kΩcm^2 for the solar cells with a 0.24 nm thick AlO_x layer and $R_{sh} < 0.87$ kΩcm^2 for solar cells without AlO_x tunneling layer [38]. The nearly 8 times lower average values of R_{sh} for solar cells without AlO_x layer can be explained by aluminum shunts and this causes a reduced *FF,* as was indicated in Figure 17. After optimal annealing, R_{sh} decreases to values between 0.58 kΩcm^2 and 2.7 kΩcm^2 for solar cells with 0.24 nm thick AlO_x and to $R_{sh} < 0.67$ kΩcm^2 for solar cells without an AlO_x layer. This shows that the AlO_x layer can successfully reduce the aluminum spiking through the n^+-emitter during annealing.

The analysis of the shifted *J-V* curves reveal an overall J_{0_total} value of (326 ± 75) fA/cm^2 for solar cells with a 0.24 nm thick AlO_x layer and J_{0_total} = (410 ± 47) fA/cm^2 for solar cells without AlO_x layer. After the optimal annealing, the J_{0_total} values decrease to (174 ± 11) fA/cm^2 for solar cells with AlO_x layer and to (320 ± 41) fA/cm^2 for solar cells without an AlO_x layer. The J_{0_total} value of (174 ± 11) fA/cm^2 clearly indicates a contact passivation effect of the AlO_x layer, reported for the first time within this thesis.

3.3 Efficacy of AlO_x contact passivation

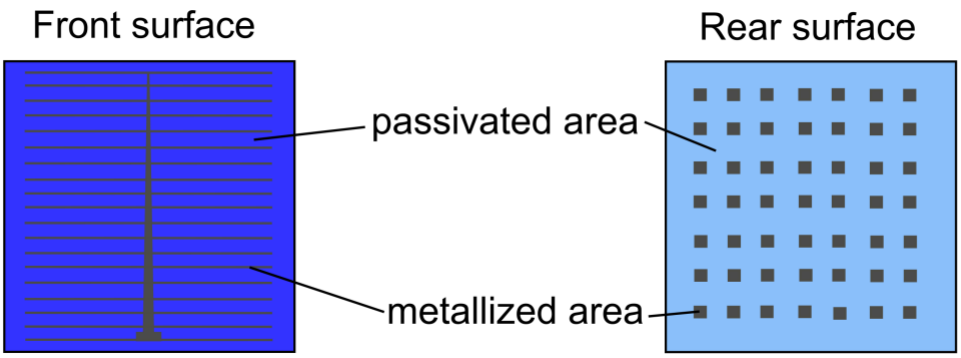

Figure 19: Metallization of our lab-type PERC devices at the front (left) and at the rear (right).

Figure 19 shows the metallization at the front and the rear surface of our PERC devices. Each area contributes a specific part to the total saturation current density J_{0_total} of our PERC solar cells. In this Section, we determine the effectiveness of the AlO_x contact passivation of the saturation current density of the non-passivated metal contact $J_{0_cont_unpass}$ and the saturation current density of the passivated metal contacts $J_{0_cont_pass}$. As a figure of merit we use the ratio:

$$\frac{J_{0_cont_unpass}}{J_{0_cont_pass}} = \frac{J_{0_total_unpass} - J_{0_bulk} - J_{0_rear} - (1-f)J_0}{J_{0_total_pass} - J_{0_bulk} - J_{0_rear} - (1-f)J_0}, \tag{3.3.2}$$

where $f = 2\%$ is the metallization fraction of the front metal grid. J_{0_rear}, J_{0_bulk}, J_0, and J_{0_cont} are J_0 contributions of the rear, the bulk, the non-metallized emitter, and at the emitter contacts, respectively. The quotient $J_{0_cont_unpass} / J_{0_cont_pass}$ represents the improvement due to the implementation of the ALD-AlO_x tunneling layer.

The saturation current density of a solar cell is determined from the *J-V* plot analysis in the previous Section. For the solar cell with passivated front metal contact a value of $J_{0_total_pass} = (174 \pm 11)$ fA/cm^2 was determined. For the solar cell with non-passivated front metal contact a value of $J_{0_total_unpass} = (320 \pm 41)$ fA/cm^2 was extracted.

Saturation current density in the bulk is calculated using following equation:

$$J_{0_bulk} = q\,\frac{n_i^2\,W}{N_A\,\tau_{int}}\,, \tag{3.3.3}$$

where $W = 275$ µm is the silicon thickness and $N_A = 3.25 \times 10^{16}$ cm^{-3} is the doping concentration. The FZ-Si bulk lifetime τ_{bulk} is assumed to be limited by intrinsic recombination. Therefore, applying the recent Auger parameterization of Richter et al. [12], we calculate a $\tau_{int} = 1.3$ ms and using equation (3.3.3) we obtain a J_{0_bulk} value of 8 fA/cm².

The rear surface of our PERC solar cells have two distinct areas, either passivated by an Al_2O_3/SiN_x stack or directly metallized by evaporated aluminum as depicted in Figure 19. Each area is described by different SRV values S_{met} or S_{pass}, for metallized and passivated areas, respectively. Therefore, the solution for a lumped SRV S is a two-dimensional problem. A one-dimensional approximation is described using the equation [43]:

$$S = \frac{D_e}{W}\left[\frac{p}{2W\sqrt{\pi f}}\arctan\left(\frac{2W}{p}\sqrt{\frac{\pi}{f}}\right) - e^{-\frac{W}{p}} + \frac{D_e}{fWS_{\text{met}}}\right]^{-1} + \frac{S_{\text{pass}}}{1-f}\,. \tag{3.3.4}$$

For the metallized area we assume $S_{\text{met}} = 1 \times 10^7$ cm/s, which is the thermal velocity of electrons in silicon, and $S_{\text{pass}} = 14$ cm/s has been determined in Section 3.1.2.2. $D_e = 23$ cm²/Vs is the electron diffusion coefficient for *p*-type silicon with a doping concentration of $N_A = 3.25\times10^{16}$ cm^{-3}, $W = 275$ µm is the solar cell thickness, $p = 2.1$ mm is the pitch, $f = 4\%$ is the rear metallization fraction. Using equation (3.3.4) and assuming low-level injection we obtain an S value of 86 cm/s for the rear surface. Using equation (2.22) we obtain:

$$J_{0_\text{rear}} = q\frac{n_i^2}{N_A}S\ , \tag{3.3.5}$$

where $n_i = 8.6\times10^9$ cm^{-3} is the intrinsic carrier concentration of silicon. Using equation (3.3.5) we calculate a J_{0_rear} value of 31 fA/cm^2.

The saturation current density of the non-metallized passivated emitter J_0 is determined from a lifetime sample, as previously described in Chapter 3.2.2. For our calculations we consider the J_0 value of (171 ± 47) fA/cm² among 5 equally processed samples after annealing. The minimum J_0 value is 124 fA/cm² and the maximum J_0 value is 192 fA/cm². Compared to the saturation current densities at the rear and in the bulk the recombination at the emitter is the major limiting factor for the open-circuit voltage of our lab-type PERC solar cells.

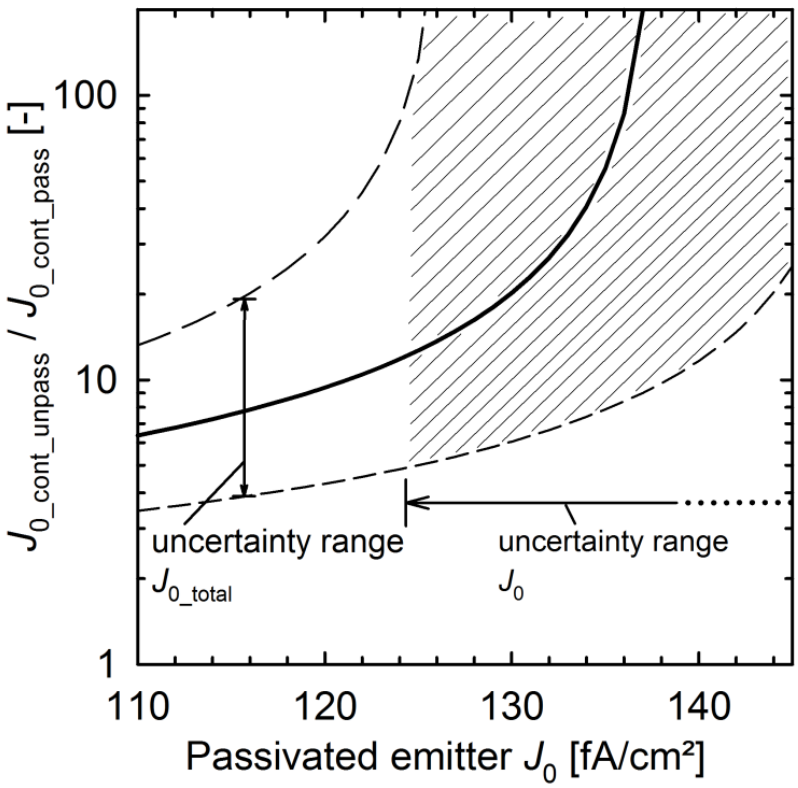

Figure 20: Relative $J_{0_cont_unpass}$ /$J_{0_cont_pass}$ quotient (solid line) as function of the passivated J_0 value. The uncertainty range of the J_0 values is marked by a horizontal arrow. Allowed $J_{0_cont_unpass}$ /$J_{0_cont_pass}$ values range is highlighted by the hatched area.

Figure 20 shows the $J_{0_cont_unpass}/J_{0_cont_pass}$ quotient (solid line) as a function of the passivated emitter J_0. The uncertainty range of the $J_{0_cont_unpass}/J_{0_cont_pass}$ quotient originates from the uncertainty of the J_{0_total} values and is marked by the dashed lines. Another value with a relative high uncertainty are the J_0 values which is in the range between 124 fA/cm² and 192 fA/cm². The uncertainty range of the J_0 values is marked by a horizontal arrow starting at 124 fA/cm². The $J_{0_cont_unpass}/J_{0_cont_pass}$ values which are within the allowed uncertainty range are highlighted by the hatched area. The $J_{0_cont_unpass}/J_{0_cont_pass}$ values describes the increased saturation current density on the non-passivated metal contacts comparing to the ALD-AlO_x passivated metal contacts.

The relatively high uncertainty range of the saturation current densities $J_{0_total_unpass}$, $J_{0_total_pass}$ and J_0 results in a high uncertainty in the ratio $J_{0_cont_unpass}/J_{0_cont_pass}$. The uncertainty range for the minimum J_0 value ranges from 4.8 to 86. For increased J_0 values the ratio even further increases. We conclude that by introducing an ultrathin AlO_x layer deposited by only two ALD cycles between the n^+-emitter and the Al metal grid the recombination at the contact is reduced by at least a factor of 4.8.

3.4 Comparison with other groups

In this Chapter, passivation properties of our ALD-AlO_x tunneling layers are compared with later results achieved by other research groups.

Loozen et al. [44] used a thermal ALD system (NanoTech, Savannah) for AlO_x deposition. Thermal ALD system uses H_2O vapor (instead of O_2 plasma compared to the plasma-assisted ALD) in the second half-reaction. Passivation was determined on lifetime samples. The front surface (light facing side) of the lifetime samples was passivated by PECVD-SiN_x. The rear surface consisted of an n^+ phosphorus-diffused emitter/AlO_x tunneling layer/metal stack. The emitter had a sheet resistance of ~100 Ω/□. The metallization was performed using evaporated Ti/Pd/Ag. The lifetime was determined through photoluminescence measurements. Loozen et al. [44] measured an effective lifetime of $\tau_{eff} < 7.5$ µs for a non-passivated metal contact and a τ_{eff} value > 15 µs for an ALD-AlO_x passivated metal contact with a thickness of 1.5 – 3 nm. In the 1.5 – 2 nm range they observed an increased lifetime by a factor of almost 3. Furthermore, *J-V* characteristics were measured on planar n^+-emitters with $R_{sheet} = 120$ Ω/□. They observed an ohmic behavior for layers with a thickness of less than 1.5 nm. For AlO_x layers with a thickness > 2 nm a deviation from the strict ohmic behavior was observed. An optimal AlO_x thickness of 1.5 nm (15 cycles) was determined [44].

Deckers et al. [45] used thermal ALD (spatial ALD system, SoLayTec) for AlO_x deposition. Passivation was determined on lifetime samples. An n^+-phosphorus emitter on planar surface with a R_{sheet} value of 45 Ω/□ and with a surface concentration of 3×10^{19} cm^{-3} active phosphorus atoms was passivated with 1 to 15 cycles of ALD-AlO_x. The metallization was realized by sputtering of an Al : 1% Si alloy. The lifetime measurement was performed by PCD and the saturation current density J_0 was determined using the method of Kane and Swanson [15]. The contact resistance was determined by TLM measurements. A decrease in J_{0_cont} with increasing numbers of ALD cycles was observed. Non-passivated metal contacts showed a J_{0_cont} of ~ 320 fA/cm^2. After 7 cycles J_{0_cont} value of ~ 250 fA/cm^2 were measured. After 7 cycles, a sharp increase of the contact resistance by two orders of magnitude was observed. 7 cycles of ALD corresponded to a thickness of 0.6 nm SiO_x + 0.96 nm AlO_x.

Bullock et al. [46] used thermal ALD (Beneq, TFS200 ALD) for the AlO_x deposition. The passivation was determined on symmetrical lifetime samples. An etched-back n^+-phosphorus emitter on a planar surface with an R_{sheet} of 103 Ω/□ and a surface concentration of 3×10^{19} cm^{-3} active phosphorus atoms

was passivated with 1 to 35 cycles of ALD-AlO_x. Only 10 nm thick Al metal films were evaporated on both surfaces. These thin Al layers provide a sufficient light transparency necessary for PCD lifetime measurements. Symmetrical lifetime samples were measured using the WCT-120 Sinton tool and the J_0 values were determined after the method of Kane and Swanson [15]. Non-passivated metal contacts showed a $J_{0_cont_unpass}$ of 1250 fA/cm^2. A severe decrease in J_{0_cont} values was observed for AlO_x thicknesses exceeding 1.5 nm. $J_{0_cont_pass}$ values saturated at 85 fA/cm² at an AlO_x thickness of 3 nm. The resulting $J_{0_cont_unpass}$ /$J_{0_cont_pass}$ ratio was 14.7 ± 0.4. Furthermore, TLM measurements where performed to determine the contact resistances. In the AlO_x thickness range 1.5 nm to 2.7 nm, a sharp increase of the ρ_{cont} value by three orders of magnitude was measured. The optimal AlO_x thickness of ~2.2 nm (22 cycles) was determined with a relatively low ρ_{cont} value of 0.3 mΩcm² and a $J_{0_cont_pass}$ value of 300 fA/cm². The resulting $J_{0_cont_unpass}$ /$J_{0_cont_pass}$ ratio is 4.2 ± 0.2. Assuming a front grid metallization fraction of 5%, a V_{oc} gain of 15 mV due to contact passivation was calculated.

All authors observed a tradeoff between a minimal amount of cycles required for improved passivation and a maximal amount of cycles which still allows for a sufficiently good ohmic contact with suitably low contact resistance. Saturation currents of all authors are within the same order of magnitude. The main difference between the results of the different authors is the optimal amount of ALD cycles: 2 in this work, 7 in the study of Deckers et al., and 22 in the work of Bullock et al. For calculations in this thesis we use saturation current density values determined by Bullock et al. In their work, a reliable approach based on the PCD method is used.

Discrepancies between the authors are the different ALD reactor types, different surfaces texturing, different metals as contact, different cleaning sequence prior to the AlO_x deposition and different doping surface concentrations. Regarding the ALD system, only in this work plasma-assisted ALD was implemented. The growth rate per cycle is smaller for the thermal ALD compared to the plasma-assisted ALD for depositions up to 40 cycles [47]. In contrast to plasma, ALD thermal ALD has shown an island growth behavior for the first 10 cycles ALD [48]. This island-like growth at the beginning of every deposition may explain a reduced GPC for thermal ALD. Therefore, depending on the ALD reactor type, on whether thermal or plasma-assisted ALD is used and depending on the silicon surface preparation more or less cycles are required to achieve an AlO_x thickness which is optimal for contact passivation. However, up to now ours is the only work implementing the ALD-AlO_x tunneling passivation layer into actual solar cells.

3.5 Chapter summary

We have demonstrated the application of ultrathin ALD-AlO_x as a contact-passivating-layers between the n^+-emitter of a solar cell and the front metal grid. We identified an optimal ALD-AlO_x layer thickness of 0.24 nm, which passivates the Al-contacts, prevents the Al-spiking and allows for a good current transport from the n^+-emitter into the Al-metal contact. Increasing the AlO_x thickness above 0.24 nm led to a drastic increase in series resistance, and hence a reduced conversion efficiency caused by a decreasing tunneling probability. The best PERC solar cell with implemented AlO_x tunneling layer fabricated in this work showed an independently confirmed record-high efficiency of 21.7% and a V_{oc} of 673 mV. Importantly, the solar cells with implemented AlO_x layers showed an improved reproducibility and only small variations in the cell parameters. A 0.24 nm thick AlO_x layer leads to a nearly 8 times larger R_{sh} value compared to cells without AlO_x layer, preventing aluminum to spike through the n^+-emitter during the SiN_x deposition at 300°C and annealing at 350°C. The very low J_{0_total} values of (171 ± 47) fA/cm^2 clearly demonstrate an effective contact passivation. Comparing the J_{0_total} values of PERC solar cells calculated from our solar cell results and J_0 values of test samples we

have determined the efficacy of the AlO_x contact passivation. Applying our ultrathin AlO_x layer deposited by only two ALD cycles between the n^+-emitter and the Al metal grid, we were able to reduce the recombination under the contact by at least a factor of 4.8. For the first time, we have hence successfully reduced the recombination at the metal contact of an electron contact region by introducing a passivation layer based on ALD-AlO_x.

4 PEDOT:PSS/c-Si heterojunctions

The interest in combining organic and inorganic materials for photovoltaic applications has skyrocketed in recent years. A tremendous attention was paid to perovskite materials, where methylammonium is incorporated into an inorganic matrix of lead and iodide. Within only a few years an impressive efficiency of 20.1% [49], [50], [51] has been achieved. However, those remarkable results were obtained on extremely small areas of 0.1 cm^2. Further limitations are implementation of lead, degradation in air and a hysteresis in the *J-V* curve. A very attractive organic-inorganic alternative is the combination of the hole-conducting polymer poly(3,4-ethylenedioxythiophene) : poly(styrenesulfonate) [PEDOT:PSS] with crystalline silicon to form a new type of heterojunction. First promising results of the PEDOT:PSS/c-Si heterojunction were presented by Avasthi et al. in 2011 [52] and He et al. in 2012 [53], [54]. They achieved energy conversion efficiencies of around 10% by implementing a PEDOT:PSS layer on the planar front surface of an *n*-type silicon wafer.

In this Chapter, we give a brief introduction into the chemistry of conductive polymers and particularly that of PEDOT:PSS. We then estimate the reasonable short-circuit current density (J_{sc}) using ray-tracing simulation and demonstrate the advantages of implementing the polymer on the rear side of the solar cell. Moreover, we propose a novel solar cell architecture with the organic-silicon junction on the rear: the so-called '*BackPEDOT*' solar cell and demonstrate its potential for highly efficient solar cells. For the first time, we characterize the organic-silicon junction in terms of saturation current densities (J_0) and contact resistances (R_C). We also optimize the PEDOT:PSS composition and the surface pre-treatment of silicon towards reduced J_0 and R_C values. We apply the adapted PEDOT:PSS composition and silicon pre-treatment on *p*-type and on *n*-type *BackPEDOT* solar cells and show that our *BackPEDOT* approach has the potential to provide comparable efficiencies to industrial PERC solar cells, however, with a simplified fabrication sequence. With this novel solar cell architecture we demonstrate an efficiency of 20.6%.

4.1 Organic conductive polymers

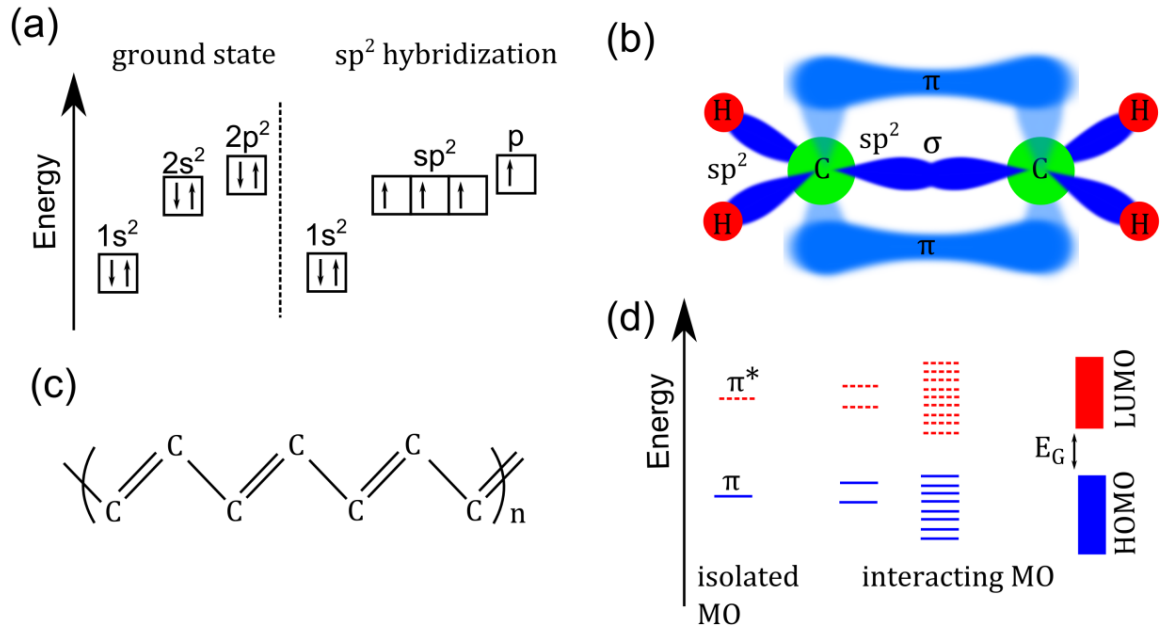

Figure 21: (a) Energy levels of electrons in a carbon atom. (b) Molecular orbitals (MO) of an ethylene molecule. (c) Structural formula of polyacetylene. (d) The energy levels of MOs are split in a conjugated polymer with an increasing interaction between MO (taken from [55]).

A polymer is a large molecule consisting of repeated subunits called monomers. Organic monomers are based on carbon atoms. In the ground state of a single carbon atom, the electrons are in the $1s^2 2s^2 2p^2$ energy configuration. In a chemical bond, the energy state of the carbon electrons alters – hybridizes – compared to the ground state. For example, in the diamond structure, electrons are $2sp^3$ hybridized. In this hybridization, carbon atoms form the diamond cubic crystal structure. In polymers, the $2sp^2$ hybridization is typical. Figure 21 (a) shows the energy levels of the ground state and the $2sp^2$ hybridization. Figure 21 (b) shows a schematic of the $2sp^2$ orbitals in an ethylene molecule. In the $2sp^2$ hybridization, three of the valence electrons are at equal energy level. The 2p orbital of the forth electron is perpendicular to the $2sp^2$ plane. The overlap of two $2sp^2$ orbitals of two different atoms is called σ bond. The overlap of two 2p orbitals of two different atoms is called π bond. A σ bond of carbon atoms is depicted in a chemical structure as C-C and called a single bond. A σ+π bond of carbon atoms is depicted in the chemical structure as C=C and called a double bond.

A polymer chain with alternating single and double bonds is called conjugated polymer. Figure 21 (c) shows the most simple conjugated polymer chain: polyacetylene [56]. After the molecular orbital (MO) theory, the 2p orbitals form a bonding π and an antibonding π* MO. The electrons in the π MO are in an energetically lower state as the electrons in the π* MO. The π orbitals of alternating single and double bonds form a mesomeric structure where the double bonds overlap with the single bonds. The electrons in the π bond can move from one bond to another via *hopping*. Figure 21 (d) shows the energy levels of MO orbitals in a conjugated polymer. With increased interaction between MO the energy levels are split after the *Peierls* distortion [57]. The highest occupied MO is called HOMO and the lowest unoccupied MO is called LUMO, similar to the valence and conduction bands in inorganic semiconductors with the corresponding energy gap E_G. A conjugated polymer with an E_G between HOMO and LUMO is an organic semiconductor.

The electrical conductivity (σ) of a pristine organic semiconductor is relatively low with σ values ranging from of 10^{-11} to 10^{-7} S/cm [58]. However, the conductivity of organic semiconductors can be increased by orders of magnitude through primary and secondary doping. Primary doping is a chemical reaction where the conjugated polymer is oxidized or reduced by a doping additive creating a *p*-doping or *n*-doping, respectively. Secondary doping further increases the conductivity of the primary-doped conjugated polymer. Secondary doping may be a structural modification of the organic matrix which improves the conductivity or/and incorporation of secondary doping-agents. Secondary doping is irreversible and after the removal of the secondary doping agents the increased conductivity remains.

A tremendous progress towards conductive polymers was achieved in 1977 by the successful doping of polyacetylene. The significance of the work of Heeger, MacDiarmid, and Shirakawa [58] was recognized in the year 2000 with the Noble Prize in chemistry '*for the discovery and development of conductive polymers*'. Further materials where investigated through the 1980s like polypyrrole [59], polythiophene [60] and polyaniline [56]. However, the electrical conductivity of those materials demonstrated an insufficient stability. An enormous progress was achieved by the invention of polymers based on 3,4-ethylenedioxithiophene.

The hole-conductive polymer poly(3,4-ethylenedioxythiophene)

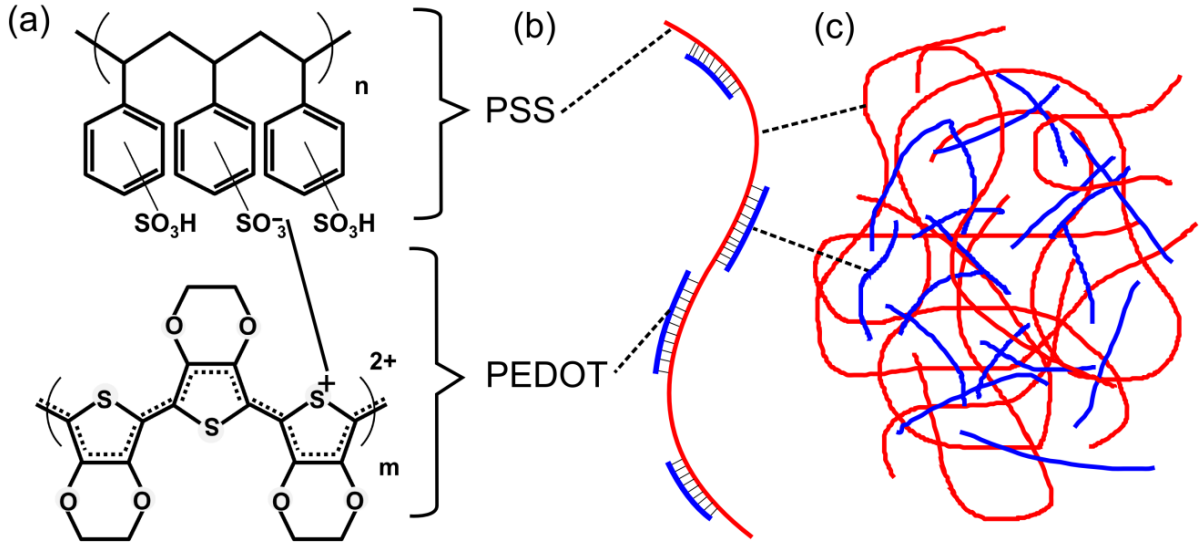

Figure 22: (a) Chemical structures of PEDOT and PSS. Shown is the oxidation of sulfur (S^+) in the PEDOT polymer (b) PEDOT staking on PSS molecule and (c) incorporation of PEDOT:PSS network (taken from Ref. [61]).

The synthesis and application of poly(3,4-ethylenedioxythiophene) (PEDOT) was patented by *BAYER* AG in 1988 [62]. Polymerization with poly(styrenesulfonate) (PSS) as a counter-ion forms a stable and water soluble PEDOT:PSS complex. PSS provides also the doping source in form of metallic ions. A positive charge is found every three to four thiophene rings [56]. Secondary dopants like dimethyl sulfoxide (DMSO) increase the conductivity to values of up to 1000 S/cm. DMSO slows down the polymerization reaction and increases the interconnection between PEDOT molecular strains. Figure 22 (a) shows the chemical structure of PEDOT and PSS molecules, (b) a schematic of the PEDOT:PSS complex and (c) a PEDOT:PSS network. As a result, short PEDOT polymers are attached to long PSS chains. The PEDOT:PSS chains form gelled particles (size of 10 nm to 1 μm) in

water. The typical water concentration in a PEDOT:PSS dispersion is 98%. The following properties made PEDOT:PSS so far the only mass-produced conductive polymer [56]:

- Conductivity of up to 1000 S/cm
- Long-term stability of the film properties
- Thermal stability of up to 200°C
- Transparency over 80% in the visible wavelengths spectrum
- Adjustable work function in the range between 4.7 and 5.6 eV
- Water-based non-toxic dispersion
- Vast variety of deposition methods, such as: spin-coating, spray-coating, dip-coating, slot-die-coating, screen-printing, and ink-jetting

Today, PEDOT:PSS is commercially applied as antistatic coating on plastic surfaces and as anode material in low equivalent series resistance electrolytic capacitors. The market leaders and patent holders for various PEDOT:PSS dispersions are *Heraeus Deutschland* GmbH & Co. KG (Leverkusen, Germany) and *Agfa-Gevaert Group* E. N. (Mortsel, Belgium) .

4.2 Deposition of PEDOT:PSS from the aqueous solution

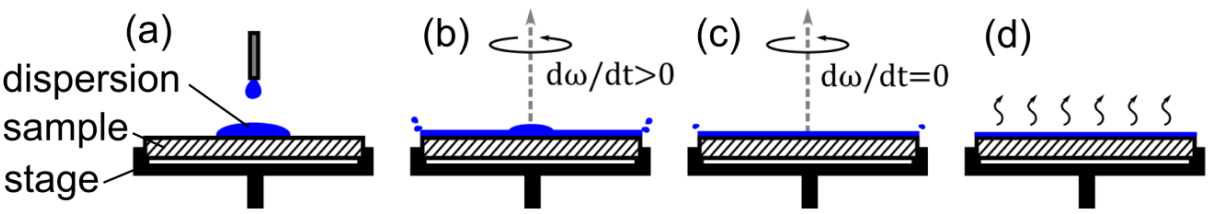

Figure 23: Deposition of PEDOT:PSS using spin-coating. (a) Positioning of the dispersion on the silicon wafer, (b) acceleration of the stage, (c) definition of the film thickness by a rotation velocity, (d) evaporation of the residual solvents on a hot plate [63].

Figure 23 schematically shows the deposition of a thin polymer film from an aqueous solution using the spin-coating method (SUSS SM 240, *KarlSuss*, Germany). First, the silicon sample is mounted on a stage. Next, the aqueous PEDOT:PSS solution is injected on the middle of the sample. The stage with the adjusted sample is accelerated to an angular velocity ω. Through centripetal force the dispersion is spread over the entire surface of the sample. The major part of the polymer dispersion is centrifuged out of the samples surface. The thickness of the deposited film depends mainly on the viscosity of the dispersion and ω. Finally, solvents are evaporated from the dispersion in an annealing step on a hot plate. We study the resulting PEDOT:PSS thickness after spin-coating and drying on silicon wafers with the commercially available PEDOT:PSS composition *F HC Solar* (*Heraeus Deutschland*, Germany).

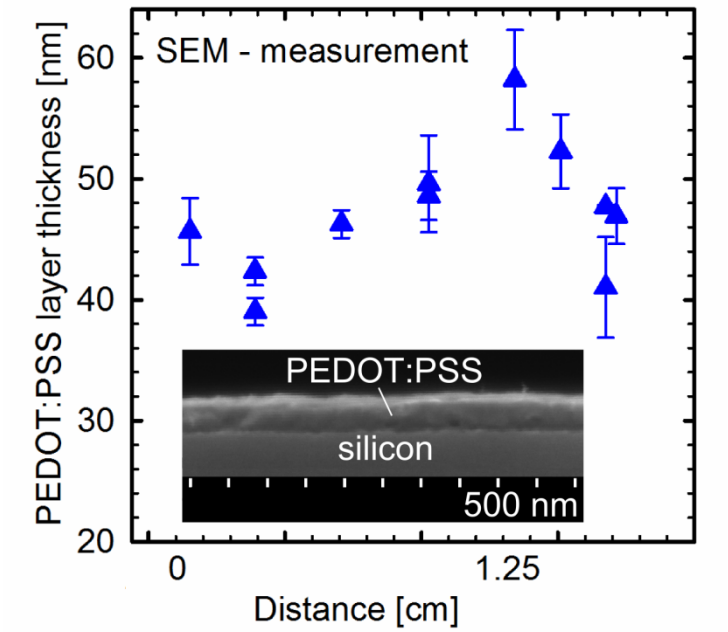

Figure 24: Scanning electron microscopy (SEM) measured thickness of spin-coated PEDOT:PSS layer as function of the position on a silicon wafer. The distance of 0 cm and 1.25 cm correspond to the sample edge and center, respectively. The inset shows an SEM image of a PEDOT:PSS layer on a silicon wafer [64].

Figure 24 shows the PEDOT:PSS thicknesses determined from scanning electron microscopy (SEM) images on different positions along the sample. The PEDOT:PSS layer was spin-coated at 1000 RPM for 10 sec and 3000 RPM for 30 sec. After spin-coating, the sample was annealed at a temperature of 130°C for 30 sec on a hot plate in air. The distance of 0 cm and 1.25 cm correspond to the sample edge and center, respectively. The PEDOT:PSS layer has a maximal thickness of ~60 nm in the sample center. The thickness decreases to a value of 40 nm close to the sample edge. This effect is caused by an increased centripetal force away from the center. At the samples edge the thickness increases slightly to a value of ~45 nm. This increased thickness is caused by a rough silicon edge which appears as the result of the laser cutting. The inset of Figure 24 shows a scanning electron microscopy (SEM) image of a PEDOT:PSS layer spin-coated at 3000 RPM on top of a silicon wafer [64]. The SEM image reveals a closed and compact PEDOT:PSS layer.

4.3 PEDOT:PSS/c-Si heterojunction solar cells

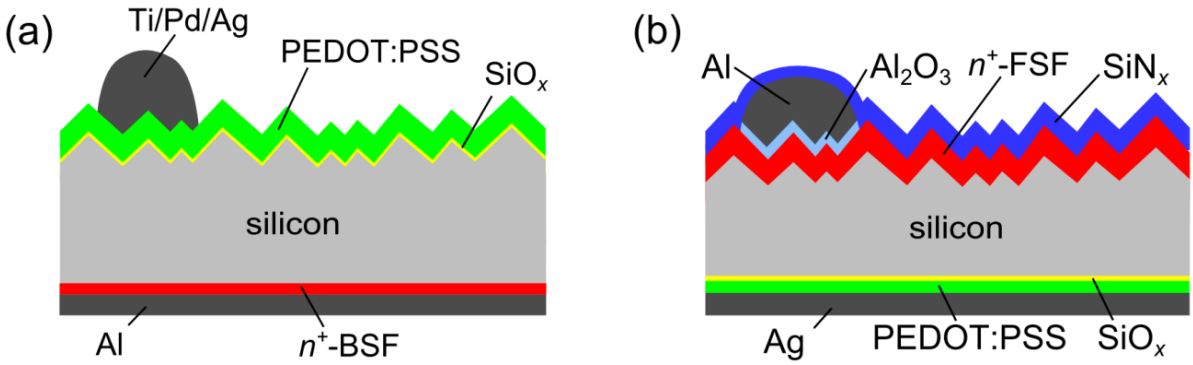

Figure 25: Schematic drawings of heterojunction organic-silicon solar cells with (a) front junction (the so-called *FrontPEDOT* solar cell) and (b) back junction (the so-called *BackPEDOT* solar cell).

Figure 25 shows the schematic drawings of (a) a front junction organic-silicon heterojunction solar cell (the so-called *FrontPEDOT* solar cell) and (b) a back junction organic-silicon heterojunction solar cell (the so-called *BackPEDOT* solar cell). Both types of solar cells are made on crystalline silicon with random-pyramid (RP)-textured front. An electron-conducting phosphorus-diffused n^+ region was either positioned on the front ('front surface field'-FSF) or on the rear ('back surface field'-BSF). The so-called 'surface field' forms an ohmic contact between the silicon base and the metal. In the case of an n^+-BSF/FSF, hole concentration is strongly reduced at the silicon/metal interface and therefore carrier recombination is reduced. In-between the silicon wafer and the PEDOT:PSS layer, we introduced an ultrathin passivation layer. In this study, we used a silicon oxide (SiO_x) layer grown in air at room temperature ('native oxide'). The PEDOT:PSS layer was deposited either on the front surface creating a front junction or on the rear surface creating a back junction solar cell. The n^+-BSF of the front junction solar cell was fully metallized by evaporated aluminum through a Ni shadow mask. The n^+-FSF of the *BackPEDOT* solar cell was passivated by SiN_x. Additionally, an ultrathin AlO_x tunneling layer improves passivation between metal and silicon as discussed in Chapter 3.2. Front metallization of the front junction solar cell was realized by titanium/palladium/silver (Ti/Pd/Ag) evaporation through a Ni shadow mask, whereas the rear surface of the back junction solar cell was fully metallized with silver.

4.4 Efficiency potential of PEDOT:PSS/c-Si solar cells

In this Section, we examine the efficiency potential of organic-silicon solar cells. The optical properties of the PEDOT:PSS layer are measured using ellipsometry and transmission techniques. Using ray-tracing simulations of realistic solar cell geometries and measured optical properties of PEDOT:PSS as the input parameters, we determine the upper short-circuit current density ($J_{sc.max}$) limit for the *FrontPEDOT* and the *BackPEDOT* solar cell concepts. The passivation properties of the PEDOT:PSS layer are measured using the photoconductance decay (PCD) technique [19] on reference samples with planar and textured surfaces. Using the method of Kane and Swanson [15] we determine the saturation current density, corresponding to an open-circuit voltage limit ($V_{oc.max}$). Combining $J_{sc.max}$ and $V_{oc.max}$ we calculate a realistic energy conversion efficiency potential assuming typical series resistance.

4.4.1 Investigation of optical properties of the PEDOT:PSS layer

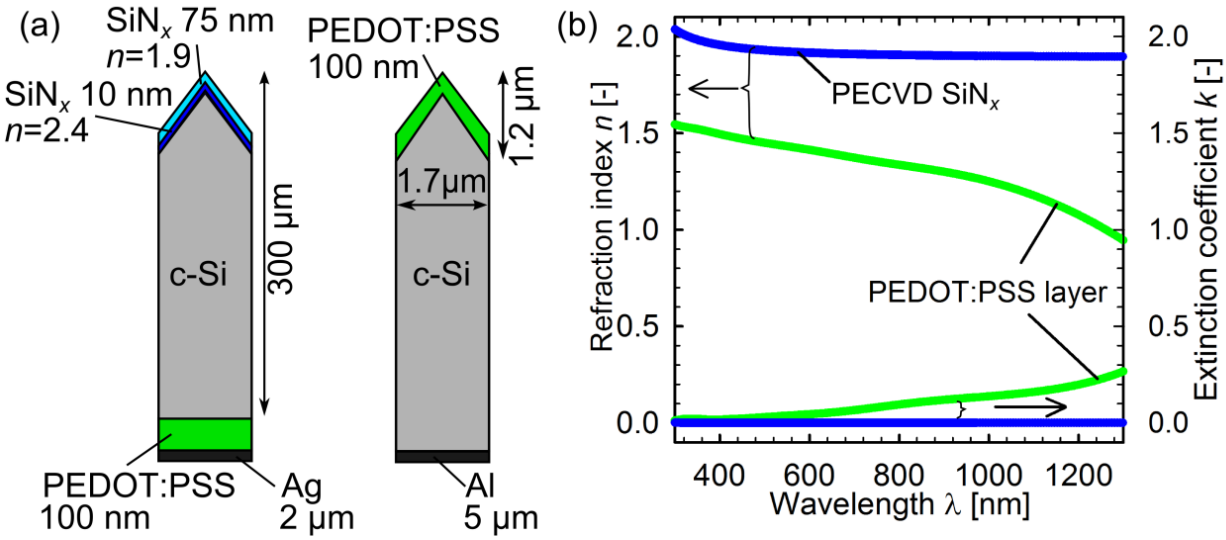

Figure 26: (a) Cross section of the simulated structures of an organic-silicon solar cell with PEDOT:PSS layer on the back (left image) and on the front (right image). (b) Measured spectrally resolved $n(\lambda)$ and $k(\lambda)$ curves for a PEDOT:PSS (*Clevious F HC Solar*) layer and for a SiN_x antireflection coating (ARC).

We calculate the maximal achievable $J_{sc.max}$ values of our organic-silicon solar cells by simulating the light absorption using the ray-tracing simulation tool Sunrays 1.3 [65]. The silicon bulk has a thickness of 300 µm. The pyramidal geometry is deduced from SEM images. Figure 26 (a) shows the simulated structure and dimensions of our *FrontPEDOT* (right) and *BackPEDOT* (left) solar cells. In our model, the base edge of a pyramid is 1.7 µm wide and the height of a pyramid is 1.2 µm. The index of refraction $n(\lambda)$ and the extinction coefficient $k(\lambda)$ of silicon as well as the dielectric layers have been measured on reference samples. We determine the optical constants of a 100 nm PEDOT:PSS layer (*F HC Solar*) using spectral ellipsometry (M-2000, *J.A. Woollam Co.*, Inc.) and transmission measurements (Cary 5000, *Varian* Inc.). Additionally, the reflection and transmission of three PEDOT:PSS layers with different thicknesses on float-glass were measured and fitted simultaneously using the ellipsometry data and the WVASE software (*J.A. Woollam Co.*, Inc., v. 3.774). The model consisted of a dominant Gaussian oscillator in the UV region outside the measurement data range and a Lorentz oscillator in the IR region. Four additional very broad Gaussian oscillators were used in the visible and NIR to account for the measured absorption. Figure 26 (b) shows measured $n(\lambda)$ and $k(\lambda)$ curves of our PEDOT:PSS material and for comparison that of an SiN_x antireflection coating [66].

In our, simulation we neglect any recombination losses and shading by the front metallization to estimate the upper $J_{sc.max}$ limit given by our front- and back junction geometries. Since recombination is absent, the current density generated by absorbed light in silicon $A(\lambda)$ equals the external quantum efficiency EQE(λ) of the solar cell.

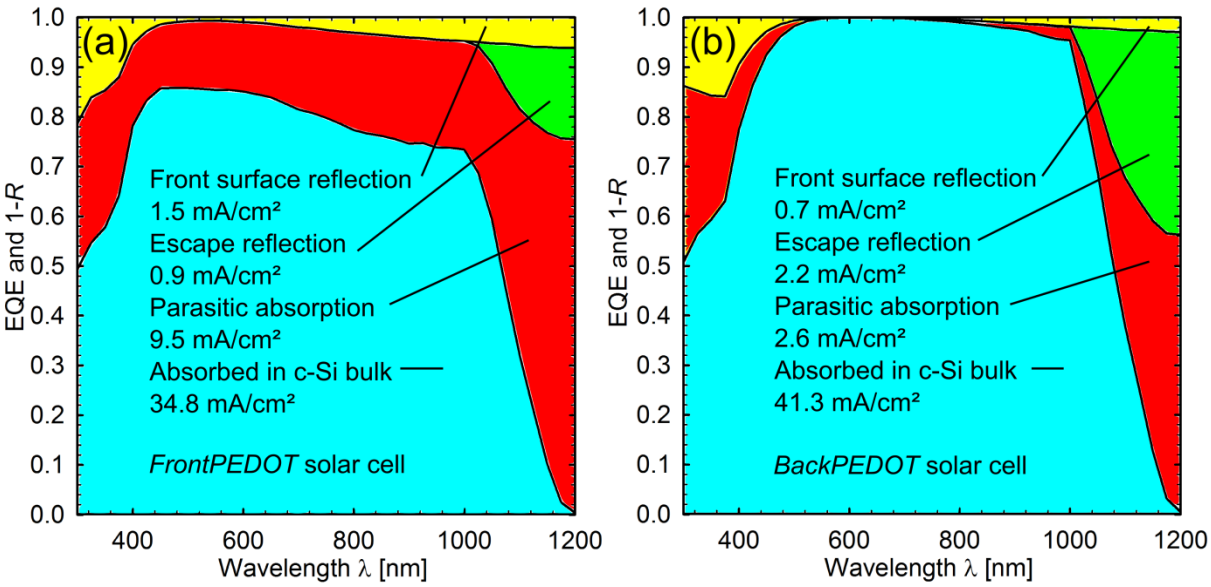

Figure 27: Simulated relative absorption in silicon $A_{Si}(\lambda)$, front surface reflection $R_{front}(\lambda)$, escape reflection $R_{esc}(\lambda)$ and parasitic absorption $A_{par}(\lambda)$ for the (a) *FrontPEDOT* and (b) *BackPEDOT* organic-silicon solar cells.

Figure 27 shows the simulated relative absorption in silicon $A_{Si}(\lambda)$, the front surface reflection $R_{front}(\lambda)$, the escape reflection $R_{esc}(\lambda)$ and the parasitic absorption $A_{Par}(\lambda)$ for (a) a *FrontPEDOT* and (b) a *BackPEDOT* organic-silicon solar cell. The total reflection is the sum of the front surface and the escape reflections. The simulated light source has a photon flux $\Phi(\lambda)$ at an intensity of 1000 W/m^2 and an AM1.5G spectrum. We obtain our maximal short-circuit current density ($J_{sc.max}$) generated through absorption in silicon by integrating the $\Phi(\lambda)$ with the relative absorption:

$$J_{\mathrm{sc.max}} = \int_{300\,nm}^{1200\,nm} \mathrm{d}\lambda\, A_{\mathrm{Si}}(\lambda) \times \Phi(\lambda)\,. \qquad (4.4.1.1)$$

For the *FrontPEDOT* geometry, the $J_{sc.max}$ loss due to the front surface reflection is 1.5 mA/cm^2. The $J_{sc.max}$ loss due to the escape reflection is 0.9 mA/cm^2. The parasitic light absorption of the front junction geometry cell results in a total $J_{sc.max}$ loss of 9.5 mA/cm^2. This tremendous amount of parasitic light absorption is largely caused by higher extinction coefficient of the PEDOT:PSS layer compared to a SiN_x antireflection coating, as shown in Figure 26 (b). This relatively large $J_{sc.max}$ loss limits $J_{sc.max}$ in the *FrontPEDOT* device to only 34.8 mA/cm^2.

For the *BackPEDOT* geometry, the $J_{sc.max}$ loss due to the front surface reflection is 0.7 mA/cm^2. The J_{sc} loss due to the escape reflection is 2.2 mA/cm^2. The optimal anti-reflection coating of the *BackPEDOT* solar cell causes a 0.9 mA/cm² lower surface reflection loss compared to the *FrontPEDOT* solar cell where the thickness and refractive index of the PEDOT:PSS layer is not optimized as an anti-reflecting-coating. The back junction geometry causes a 1.3 mA/cm² higher escape reflection loss compared to the front junction solar cell geometry caused by different rear surface metallization. So far, the PEDOT:PSS layer cannot be directly contacted by Al due to an oxidation effect of the acid component of the organic layer [56]. The parasitic light absorption of the back junction geometry cell results in a total $J_{sc.max}$ loss of 2.6 mA/cm^2. This substantially lower parasitic absorption loss of 6.9 mA/cm² compared to the *FrontPEDOT* solar cell is a significant advantage of the *BackPEDOT* solar cell. For the *BackPEDOT* solar cell a maximal $J_{sc.max}$ value of 41.3 mA/cm^2 is reachable. As we can observe in Figure 27 (b) we still have a significant amount of parasitic light absorption in the

wavelength of over 1000 nm. One possible improvement in future development could be incorporation of back-reflecting nano particles into the PEDOT:PSS layer [67], [68].

Our solar cells has a metal grid on the front surface with a metallization fraction of 2%. Assuming a wavelength-independent loss of 2%, we obtain a realistic $J_{sc.max}$ value of 34.1 mA/cm^2 and 40.5 mA/cm^2 for the *FrontPEDOT* and *BackPEDOT* solar cells, respectively.

4.4.2 Passivation properties of PEDOT:PSS on c-Si

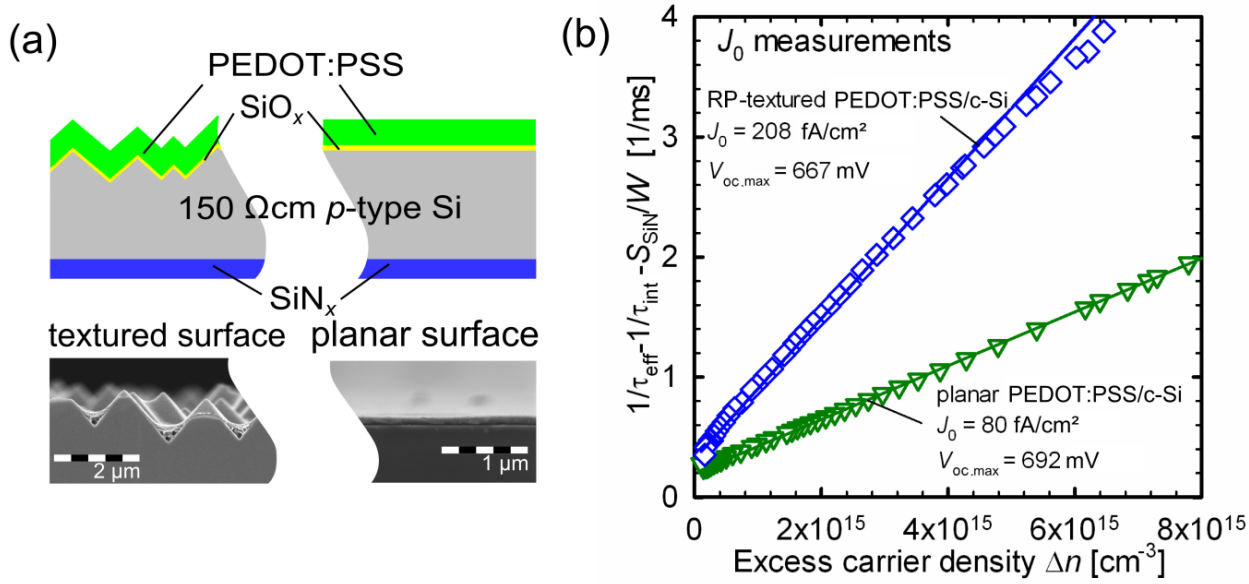

Figure 28: (a) Schematic cross section and SEM image of a textured and a planar lifetime test sample used for saturation current density (J_0) measurements. (b) Inverse effective lifetime $1/\tau_{eff}$ minus the inverse intrinsic lifetime $1/\tau_{int}$ minus the surface-related lifetime on the SiN_x-passivated surface S_{SiNx}/W as function of excess carrier density Δn of PEDOT:PSS on the passivated textured (blue diamonds) and on the planar (green triangles) silicon surface.

Figure 28 (a) shows the lifetime test structure used to extract the saturation current densities (J_0) of the organic-silicon junctions on random pyramid (RP)-textured and planar surfaces, respectively. We use virtually undoped (~150 Ωcm) single-crystalline (100)-oriented 300 µm thick *p*-type float-zone (FZ) silicon wafers. After RCA cleaning of the silicon wafers, we deposit a 110 nm thick SiN_x surface-passivating layer by means of plasma-enhanced chemical vapor deposition (PECVD, *Oxford Instruments*, *Plasmalab* 80+) on one side of the single-crystalline silicon (c-Si) wafer. Some c-Si wafers are then RP-textured on the bare wafer side in an anisotropic KOH/2-propanol etching solution. In order to form a passivating tunneling layer between the organic layer and the c-Si wafer, a native oxide (SiO_x) is then grown by storing the wafer for 24 hours in ambient air. Subsequently, the samples are coated with the PEDOT:PSS precursor (*F HC Solar*, *Clevios Heraeus GmbH*) by spin-on technique (SUSS SM 240, *KarlSuss,* Germany) and dried on a hotplate at 130°C for 30 seconds.

Furthermore, we fabricate reference samples passivated with SiN_x with a refractive index n of 2.4 (at $\lambda = 632$ nm) on both surfaces, where we measure an effective surface recombination velocity of $S_{SiN} = 14$ cm/s (at an excess carrier density ranging between 10^{14} and 10^{16} cm^{-3}) for the SiN_x-passivated surface (see Chapter 3.1.2.1). Saturation current densities J_0 are deduced from transient photoconductance decay (PCD) measurements using a WCT-120 lifetime tester from Sinton Instruments [19] and applying the method of Kane & Swanson [15].

Figure 28 (b) shows the inverse effective lifetime $1/\tau_{eff}$ minus the inverse intrinsic lifetime $1/\tau_{int}$ minus the surface-related lifetime on the SiN_x-passivated surface S_{SiNx}/W as a function of the excess carrier concentration Δn of a planar and a textured silicon-PEDOT:PSS sample, respectively. We extract a saturation current density J_0 of only 80 fA/cm^2 for the planar sample [69]. Random-pyramid texturing of the silicon surface increases J_0 to a value of 208 fA/cm^2. We explain the increased J_0 value for textured samples by the increased surface area and the fact that PEDOT:PSS does not completely cover the textured surface as shown in the SEM image in Figure 28 (a).

4.4.3 Realistic Efficiency potential of PEDOT:PSS/c-Si solar cells

Regardless of the cell architecture, we can calculate a V_{oc} potential based on our J_0 measurements and J_{sc} estimations presented in the previous Section. We can now calculate the highest reachable $V_{oc.max}$ of our organic-silicon solar cells using the equation:

$$V_{\mathrm{oc.max}} = V_{\mathrm{T}} \times ln\left(\frac{J_{\mathrm{sc.max}}}{J_0} + 1\right) \qquad (4.4.2.2)$$

where V_T = 25.7 mV is the thermal voltage at a temperature of 25°C and $J_{sc.max}$ equals 34.1 mA/cm^2 and 40.5 mA/cm^2 for the *FrontPEDOT* and *BackPEDOT* solar cell, respectively. These $J_{sc.max}$ values were determined in Section 4.4.1 based on our optical measurement of PEDOT:PSS properties and ray-tracing simulation considering the 2% front surface shading by the metal grid. In the following, we calculate the highest reachable $V_{oc.max}$ of our *FrontPEDOT* and *BackPEDOT* solar cells, respectively. The V_{oc} of our *FrontPEDOT* solar cell is largely limited by the fully metallized n^+-BSF rear side exhibiting a $J_{0_cont_unpass}$ of 1250 fA/cm^2 [46], whereas the V_{oc} of our *BackPEDOT* solar is limited by the SiN_x passivated n^+ front exhibiting a J_0 of 124 fA/cm^2 (see Section 3.1.2.1).

The total $J_{0_FrontPEDOT}$ of the *FrontPEDOT* solar cell is calculated by adding the recombination current contributions of the random-pyramid-textured PEDOT:PSS/c-Si front with $J_{0_PEDOT_RP}$ = 208 fA/cm^2, the fully metallized n^+-BSF rear with $J_{0_cont_unpass}$ of 1250 fA/cm^2 [46] and the saturation current density within the bulk J_{0_bulk} = 8 fA/cm²:

$$J_{0_\mathrm{FrontPEDOT}} = J_{0_\mathrm{PEDOT_RP}} + J_{0_\mathrm{bulk}} + J_{0_{\mathrm{cont_unpass}}} = 1466\ \frac{\mathrm{fA}}{\mathrm{cm}^2} \qquad (4.4.2.3)$$

The total $J_{0_BackPEDOT}$ of our *BackPEDOT* solar cell is calculated by adding the recombination current contributions of the planar PEDOT:PSS/c-Si rear surface with $J_{0_PEDOT_pl}$ = 80 fA/cm^2, of the passivated metal contacts on the n^+-FSF $J_{0_cont_pass}$ = 300 fA/cm^2 [46], of the SiN_x-passivated n^+-FSF front with J_0 = 124 fA/cm^2, of the saturation current density within the bulk J_{0_bulk} = 8 fA/cm² and the metallization fraction of the front grid f = 2%:

$$J_{0_\mathrm{BackPEDOT}} = fJ_{0_\mathrm{cont_pass}} + (1-f)J_0 + J_{0_\mathrm{bulk}} + J_{0_\mathrm{PEDOT_pl}} = 218\ \frac{\mathrm{fA}}{\mathrm{cm}^2} \qquad (4.4.2.4)$$

Combining results of the equations (4.4.2.3) and (4.4.2.4) we calculate using equation (4.4.2.2) the maximum reachable open-circuit voltages $V_{oc.max}$ of 613 mV and 667 mV for our *FrontPEDOT* and *BackPEDOT* solar cells, respectively.

To calculate the efficiency we need to determine the fill factor. At first we calculate the ideal fill factor FF_0 using the empirical equation [70]:

$$FF_0 = \frac{v_{\mathrm{OC}} - \ln(v_{\mathrm{OC}} + 0.72)}{v_{\mathrm{OC}} + 1}. \tag{4.4.2.5}$$

Thereby v_{OC} is defined as:

$$v_{\mathrm{OC}} = \frac{qV_{\mathrm{oc}}}{k_{\mathrm{B}}T}. \tag{4.4.2.6}$$

Using the equation (4.4.2.5) we calculate FF_0 of 83.1% and 84.1% for our *FrontPEDOT* and *BackPEDOT* solar cells, respectively. However, these FF_0 values do not include any influence of the series resistance which is omnipotent in every device powered at room temperature. A reasonable area-weighted series resistance R_s value is 0.5 Ωcm² [71]. Using the FF_0 values and this realistic R_s we can now calculate a realistic *FF* using following equation:

$$FF = FF_0\left(1 - \frac{R_{\mathrm{s}} \times J_{\mathrm{sc}}}{V_{\mathrm{oc}}}\right). \tag{4.4.2.7}$$

Finally, using the equation (4.4.2.7) we calculate *FF*s of 80.8% and 81.5% for our *FrontPEDOT* and *BackPEDOT* solar cells, respectively.

Combining these J_{sc}, V_{oc} and *FF* values we calculate an efficiency potential of 16.9% for the *FrontPEDOT* and 22.0% for the *BackPEDOT* solar cell, respectively. Our estimation highlights the high efficiency potential of our *BackPEDOT* solar cell approach. Of course, higher efficiencies would be achievable if one of the dominant recombination losses could be further reduced. In our *BackPEDOT* solar cell the recombination on the passivated n^+-emitter is the major loss. The given solar cells efficiencies are not limited by the organic-silicon junction.

4.5 Fabrication of organic-silicon heterojunction solar cells

In this Section, we present the fabrication sequence and results of our *FrontPEDOT* and *BackPEDOT* solar cells. We compare the results of both approaches with the estimated realistic efficiency potential.

4.5.1 *FrontPEDOT* processing sequence

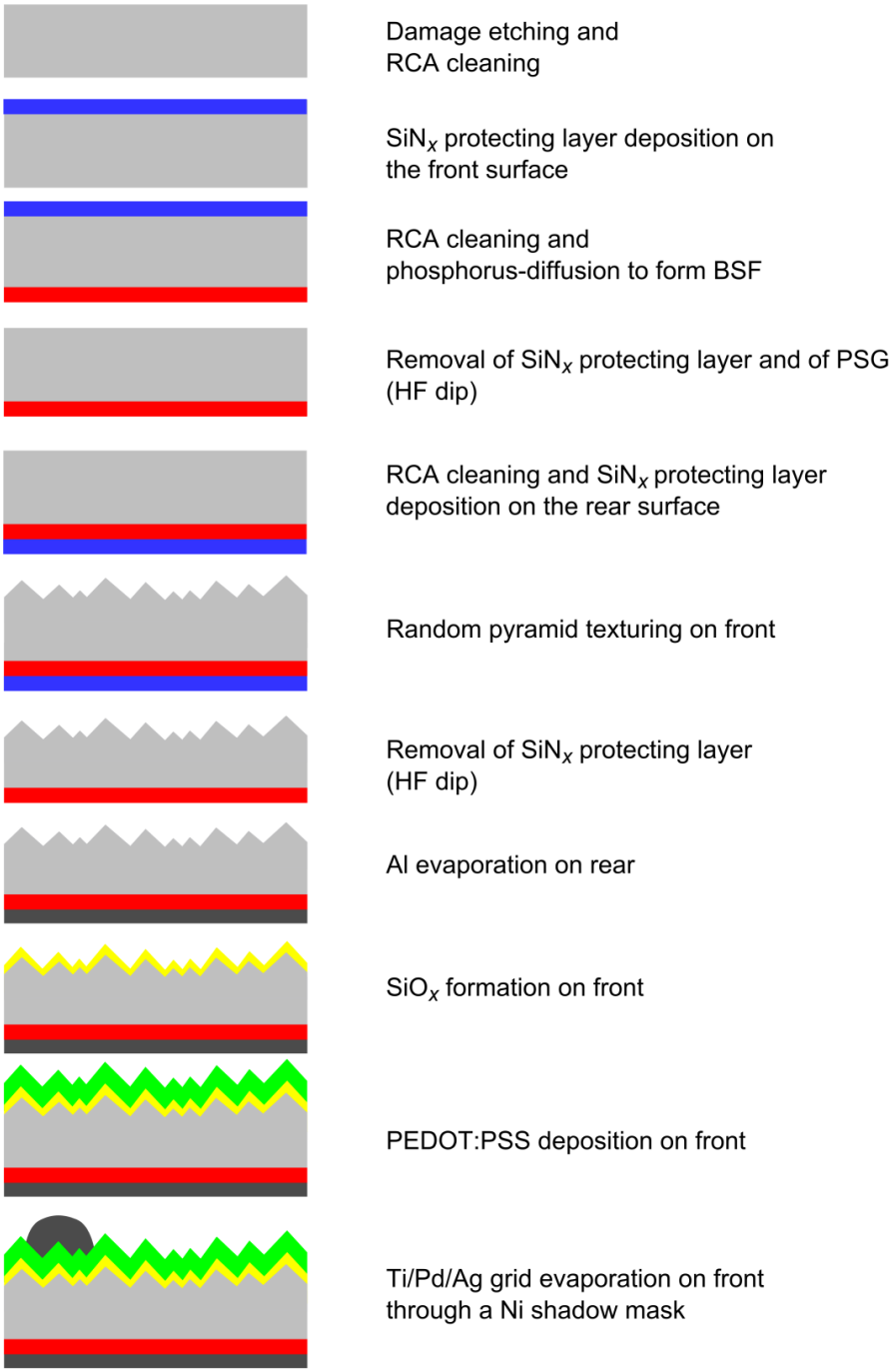

Figure 29: Process flow diagram of a *FrontPEDOT* solar cell.

Figure 29 shows the process flow of the *FrontPEDOT* solar cell. In the cell process, we start with a 300 µm thick phosphorus-doped (100)-oriented float-zone (FZ) *n*-type silicon wafer with a resistivity of 1.5 Ωcm. After RCA cleaning, the front surface is protected with a 100 nm thick SiN_x layer. Subsequently, after RCA cleaning, a back surface field (BSF) is formed by phosphorus diffusion from a $POCl_3$ source in a quartz-tube furnace at a temperature of 850°C. The resulting n^+-BSF has a sheet resistance of (152 ± 9) Ω/□. Next, the front SiN_x protecting layer and the phosphorus silicate glass (PSG) are removed in diluted hydrofluoric acid (HF) and the wafer rear side is protected by a SiN_x protection layer. After RCA cleaning, the front surface is RP-textured in a KOH/2-propanol solution and the SiN_x is removed in a diluted HF solution. Subsequently, aluminum is deposited on the entire rear surface by electron beam evaporation. After rear side metallization, the samples are stored in air for approximately 30 hours to grow a native tunneling oxide on the front side. Next, a PEDOT:PSS (*F HC Solar*) layer is deposited by spin-coating on the entire front surface at 1000 revolutions per minute (rpm) for 10 seconds and subsequently 2000 rpm for 30 seconds, which results in a thickness of approximately 100 nm. The thickness is measured on a planar glass reference sample by scratching a trench into the PEDOT:PSS layer. The depth of the trench is measured using a profilometer (Dektak 150, Veeco). Finally, a Ti/Pd/Ag grid with a finger spacing of 1 mm is evaporated onto the PEDOT:PSS through a Ni shadow mask by electron beam evaporation.

4.5.2 *BackPEDOT* processing sequence

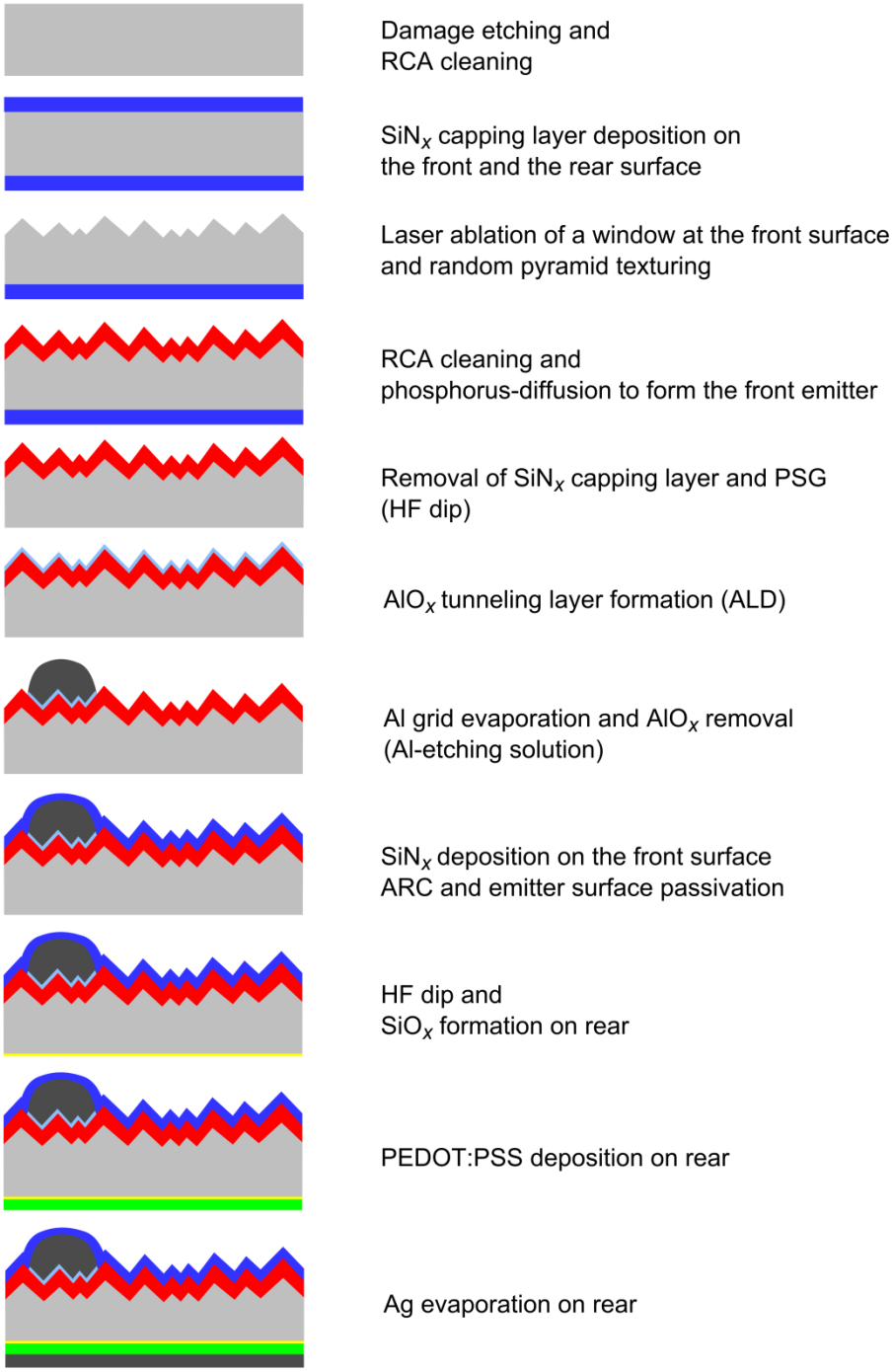

Figure 30: Process flow diagram of a *BackPEDOT* solar cell.

Figure 30 shows the process flow of the *BackPEDOT* solar cell. In our process, we start with an *n*-type Czochralski (Cz) grown phosphorus-doped silicon wafer with a resistivity of 4-5 Ωcm and a thickness of 160 µm. After RCA cleaning, the wafer is protected on both surfaces with a 100 nm thick SiN_x layer. On the front surface, a 2×2 cm^2 diffusion window is opened by laser ablation (frequency-doubled Nd:YVO_4 laser, SuperRapid, *Lumera Laser*). Within the ablated window, the silicon surface is RP-textured in a KOH/2-propanol solution. After RCA cleaning, a phosphorus diffusion is performed from a $POCl_3$ source in a quartz-tube furnace at 850°C forming a front-surface-field (FSF) with a sheet resistance of (114 ± 11) Ω/□. After removing the protecting SiN_x layer and the PSG in

diluted hydrofluoric acid, a 0.24 nm AlO_x tunneling layer is grown by atomic layer deposition (FlexAL, *Oxford Instruments*) on the front surface. Next, a 20 µm thick aluminum grid with a finger spacing of 1 mm is deposited through a nickel shadow mask by electron beam evaporation. After metallization, the front surface is covered by a 10 nm surface-passivating SiN_x layer with a refractive index n of 2.4 (at $\lambda = 632$ nm) and by a 75 nm SiN_x antireflection layer with a refractive index n of 1.9 (at $\lambda = 632$ nm) on top. Both SiN_x layers are deposited at a temperature of 330°C using PECVD. Next, the rear surface is dipped in 1% diluted HF solution for 1 min. Afterwards, the samples are stored in air for 24 hours to form a native oxide at the rear surface. Next, a PEDOT:PSS layer with a thickness of (140 ± 7) nm (*F HC Solar*, *Heraeus Deutschland*) is deposited by spin-coating on the entire rear at 500 revolutions per minute (RPM) for 10 seconds and subsequently 1500 rpm for 30 seconds. The sample is then dried on a hotplate in air at 130°C for 30 seconds. Finally, the entire rear surface is metallized by 2 µm thick electron-beam-evaporated silver.

4.5.3 Solar cell results and discussion

Illuminated current-voltage (*J-V*) characteristics at an illumination intensity of 100 mW/cm^2, external quantum efficiency [EQE(λ)], and reflectance are measured using a commercial measurement system (LOANA System, pv-tools [6], Hamelin, Germany) with an aperture area mask of 2 × 2 cm². We correct the spectral mismatch by comparing the EQE(λ) of our solar cell with an EQE(λ) reference solar cell measured under standard testing conditions at Fraunhofer ISE CalLab.

Table 3: Parameters of the *FrontPEDOT* and *BackPEDOT* organic-silicon solar cells calculated and measured at 100 mW/cm² at a temperature of 25°C. The aperture area of the organic-silicon solar cells is 4 cm².

Organic-silicon solar cell type	V_{oc} mV	J_{sc} mA/cm^2	*FF* %	p*FF* %	η %	pη %	R_{s_dlt} Ωcm²
FrontPEDOT	603	29.0	70.6	72.8	12.3	12.7	0.92
FrontPEDOT	601	29.2	69.6	72.6	12.2	12.7	0.99
BackPEDOT	653	39.7	67.2	82.0	17.4	21.2	2.88
BackPEDOT	663	39.0	66.3	81.3	17.1	21.0	3.35

Table 3 summarizes measured solar cell parameters of our *FrontPEDOT* and *BackPEDOT* organic-silicon solar cells. The best *FrontPEDOT* solar cell shows a V_{oc} of 603 mV and a J_{sc} of 29.2 mA/cm^2. Note that despite the moderate series resistance of $R_s = 0.92$ Ωcm^2 we obtain a relatively low fill factor *FF* of only 70.6% and a poor pseudo *FF* of only 72.8%. The achieved solar cell efficiency of 12.3% was amongst the highest *FrontPEDOT* organic-silicon solar cell efficiencies reported at that point in time [69].

In order to fully exploit the potential of combining organic photovoltaics with silicon-based photovoltaics, we apply the organic PEDOT:PSS layer to the planar rear of a c-Si wafer and implemented an n^+-FSF plus an effective dielectric passivation. With this novel *BackPEDOT* solar cell concept, we achieve a remarkably high open-circuit voltage V_{oc} of 663 mV and a very high short-circuit current density J_{sc} of 39.7 mA/cm^2. Despite the relative low fill factor *FF* of up to 67.2%, we achieve energy conversion efficiencies of up to 17.4%. By introducing the *BackPEDOT* concept, we improved the efficiency of organic-silicon solar cells by $5\%_{abs}$ compared to the best results reported at that time [66] for *FrontPEDOT* organic-silicon solar cells.

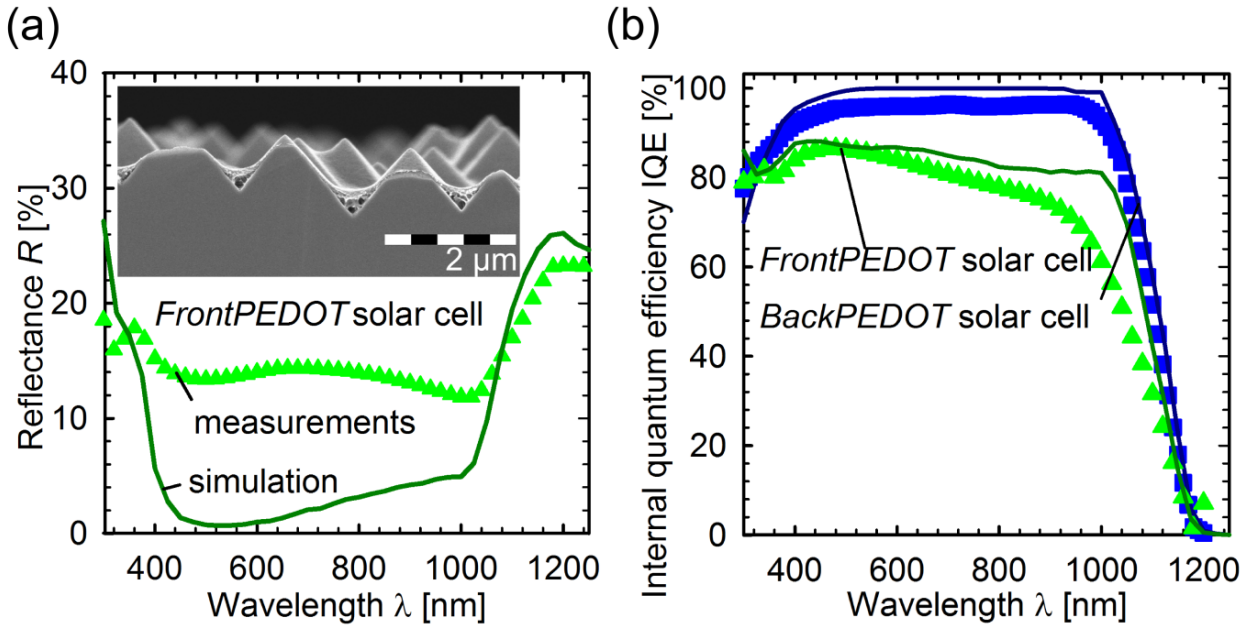

Figure 31: (a) Measured (symbol) and simulated (line) reflectance $R(\lambda)$ of our *FrontPEDOT* solar cell. The inset shows an SEM image of our PEDOT:PSS layer covering a random-pyramid-textured silicon surface. (b) Measured (symbols) and simulated (lines) internal quantum efficiencies IQE(λ) of a *FrontPEDOT* organic-silicon cell (green line/symbols) and a *BackPEDOT* (blue line/symbols).

Implementing PEDOT:PSS at the rear surface and passivating the n^+-FSF with SiN_x leads to a V_{oc} improvement in the range of 50 to 62 mV. This improvement correlates well with our estimations made in the previous Section (4.4.3), where a V_{oc} improvement between the *FrontPEDOT* and *BackPEDOT* solar cell architecture of 54 mV was calculated. The J_{sc} improvement in the range of 9.8 to 10.7 mA/cm^2, on the other hand, is larger than our simulated improvement of 6.4 mA/cm^2. There are two reasons for this discrepancy. First, light reflection from the *FrontPEDOT* solar cell is larger compared to the simulation. Figure 31 (a) shows the measured and simulated reflection. The inset of Figure 31 (a) shows an SEM image of our PEDOT:PSS layer covering a random-pyramid-textured silicon surface. It is obvious that the PEDOT:PSS layer flattens the surface morphology and therefore increases the reflection. The difference between the measured and the simulated reflectance leads to a J_{sc} loss of 4.25 mA/cm^2 for the *FrontPEDOT* solar cell. The second reason for the observed discrepancy is the increased surface recombination of our *FrontPEDOT* solar cell. Figure 31 (b) shows the measured and simulated IQE(λ) curves. Note that the IQE(λ) losses are not considered in our simulation. We observe a clear deviation between the simulated and measured IQE(λ) at higher wavelengths for the *FrontPEDOT* solar cell. Since high-purity float-zone silicon is used, this deviation can only be caused by an increased rear surface recombination. We are not surprised about high recombination at the rear surface since the n^+-BSF is not passivated and fully metallized. Increased recombination at the rear surface of our *FrontPEDOT* solar cell leads to a decreasing IQE(λ) curve for wavelengths larger than 600 nm. The difference between the measured and simulated IQE(λ) leads to a J_{sc} loss of 2.78 mA/cm^2 for our *FrontPEDOT* solar cell, compared to a J_{sc} loss of only 1.84 mA/cm^2 for our *BackPEDOT* solar cell.

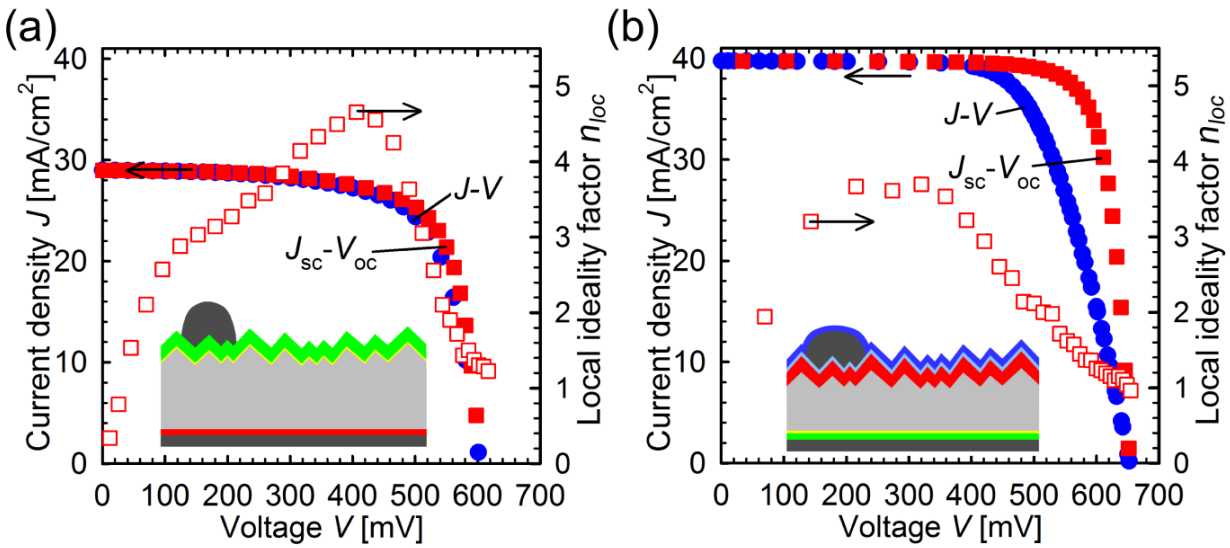

Figure 32: Illuminated current density-voltage (*J-V*) (red squares), short-circuit current density - open-circuit voltage (J_{sc}-V_{oc}) measurements (blue circles) and the local ideality factor n_{loc} (open squares) of the J_{sc}-V_{oc} curve for (a) a *FrontPEDOT* and (b) a *BackPEDOT* solar cell.

Figure 32 shows illuminated current density-voltage (*J-V*) and J_{sc}-V_{oc} measurements, as well as measurements of the local ideality factor n_{loc} of the J_{sc}-V_{oc} curve for our best (a) *FrontPEDOT* and (b) *BackPEDOT* solar cells, respectively. The ideality factor n_{loc} is the inverse slope of the semi-logarithmic J_{sc}-V_{oc} curve. Values larger than unity are caused by low shunt-resistances and/or by injection-dependent recombination parameters in the bulk and/or at the surfaces. The influence of the series resistance on n_{loc} can be avoided by analyzing the J_{sc}-V_{oc} curve.

For the *FrontPEDOT* solar cell, the ideality factor increases to n_{loc}= 3 at the pseudo maximum power-point voltage pV_{mpp} = 512 mV limiting the pseudo fill factor p*FF* to a value of only 72.8%. For the *BackPEDOT* solar cell – where front and rear surfaces are passivated – we obtain a relatively low n_{loc} = 1.5 at the pseudo maximum power-point voltage pV_{mpp} = 565 mV allowing p*FF* values of 82.0%. By comparing the J_{sc}-V_{oc} and the *J-V* curve of our *BackPEDOT* solar cell one can clearly notice a shift of the *J-V* curve towards lower voltages caused by the series resistance. Measurements of the series resistance (R_s) at the maximum power-point of the *J-V* curve using the double-light method reveal a strong scattering in R_s values between 2.88 Ωcm² and 3.35 Ωcm^2. For the lowest R_s value of 2.88 Ωcm^2 we measure a *FF* of 67.2% and an energy conversion efficiency of 17.4%, which was the highest reported value for organic-silicon heterojunction solar cells at the time of publication [66]. Analyzing the J_{sc}-V_{oc} curve and, hence, neglecting the influence of the series resistance, we measure a pseudo fill factor of p*FF* = 82.0% and a pseudo efficiency of pη = 21.2% for our best *BackPEDOT* cell.

4.6 Optimizing the PEDOT:PSS/c-Si interface

In the previous Section, we have shown that a PEDOT:PSS layer is capable of effectively passivating a crystalline silicon surface. This finding is quite surprising since the implemented commercial PEDOT:PSS dispersion *F HC Solar* was not developed for the application to crystalline silicon surfaces. To explore the full surface passivation potential of PEDOT:PSS, modified dispersions were created in a collaborative work with *Heraeus Deutschland*. Additionally, the silicon surface pre-treatment is optimized towards reduced saturation current densities and reduced contact resistance of the organic-silicon interface. The optimized PEDOT:PSS dispersion combined with the optimized silicon pre-treatment are implemented into our *BackPEDOT* solar cell.

4.6.1 Optimization of the PEDOT:PSS composition

One essential criteria for the desired PEDOT:PSS layer is an excellent passivation of the silicon surface. Therefore, we examine the passivation quality of PEDOT:PSS layers of different compositions on test structures, as described in Chapter 4.4.2. In a collaborative work with *Heraeus Deutschland* a variety of different PEDOT:PSS dispersions was created. One major varied parameter was the ratio between PEDOT and PSS. Furthermore, ingredients like dimethyl sulfoxide (DMSO), cross-linker, fluor-polymers and other components were partially added to the water-based solution. We were able to localize one type of PEDOT:PSS dispersion – which will be named '*optimized*' in the following – with an improved passivation ability compared to the commercial *F HC Solar* dispersion. Due to an ongoing industrial collaboration with *Heraeus Deutschland*, we will not disclose the exact composition of the *optimized* dispersion in this work.

Figure 33 shows the lowest measured saturation current density J_0 for the commercial PEDOT:PSS solution *F HC Solar* and the J_0 value for the newly developed *optimized* PEDOT:PSS dispersion.

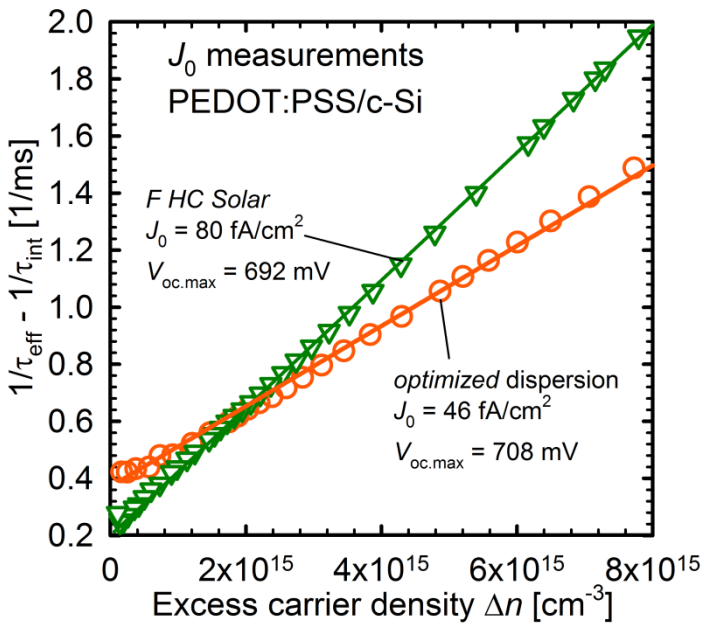

Figure 33: Inverse effective lifetime minus the inverse intrinsic lifetime as function of excess carrier dens1ity Δn of silicon wafers passivated by commercial *F HC Solar* (green triangles) and the *optimized* PEDOT:PSS dispersion (orange circles). Lines are linear fits to the measured data

The J_0 values were determined after the method proposed by Kane and Swanson [15]. The lowest measured J_0 value for the *F HC Solar* PEDOT:PSS is 80 fA/cm² [66] and the lowest measured J_0 value for the *optimized* PEDOT:PSS is 46 fA/cm² [72]. Analogous to the calculations made in Chapter 4.4.2 now implementing *optimized* PEDOT:PSS we obtain an ideal $V_{oc.max}$ increase of 16 mV compared to *F HC Solar*.

4.6.2 Optimization of the silicon surface pre-treatment

In this Section, the impact of different silicon surface pre-treatments before the PEDOT:PSS deposition on the saturation current density J_0 is examined. We use the *optimized* PEDOT:PSS dispersion throughout this Section.

We perform transient photoconductance decay (PCD) measurements on lifetime samples, as schematically shown in the inset of Figure 34 and extract the saturation current densities J_0 according to the Kane and Swanson method [15]. We use virtually un-doped 150 Ωcm *p*-type FZ-silicon wafers with a thickness of 300 µm as base material for our lifetime samples. After RCA cleaning, we deposit a 100 nm thick well-passivating SiN_x layer by means of PECVD at a deposition temperature of 400°C onto one side of the silicon wafer.

After the SiN_x deposition, we apply different treatments to the other side of the wafer [73] prior to the subsequent deposition of the PEDOT:PSS dispersion using spin-coating in ambient air and annealing at 130°C for 15 minutes. A first set of samples was (i) coated with PEDOT:PSS directly after the SiN_x deposition on the other side without any further pre-treatment. For the next three sets of samples, the wafers were HF dipped (1% HF solution, 1 minute) and stored in ambient air for (ii) 10 minutes, (iii) 20 hours, and (iv) 30 days prior to the PEDOT:PSS deposition. Furthermore, we included the following additional tunneling layers: (v) a chemically grown SiO_x by omitting the last HF dip in the RCA cleaning sequence, (vi) an O_2-plasma treatment of the silicon wafer surface using two cycles of plasma-assisted ALD (see Section 3.1.2.2) without using TMA, and (vii) a thermally grown SiO_x layer ('tunneling oxide') of ~1.5 nm thickens [37]. To grow this 'tunneling oxide' we first chemically grew SiO_x by omitting the last HF dip in the RCA cleaning sequence. Next, the chemically grown SiO_x was annealed in a quartz-tube furnace at 500°C for 15 mins in O_2 atmosphere.

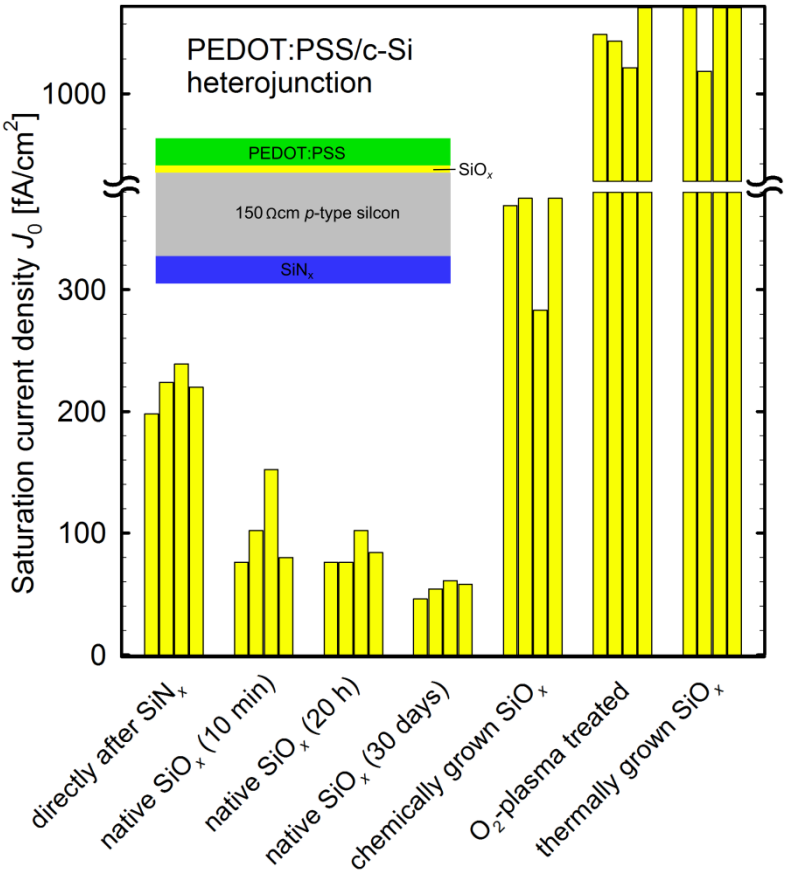

Figure 34: Saturation current densities J_0 of PEDOT:PSS passivated lifetime samples as function of different silicon surface pre-treatments. The inset schematically shows the lifetime test samples.

Figure 34 shows the saturation current density J_0 values of silicon samples with differently treated silicon surfaces. Each bar represents one lifetime sample. As a rule of thumb, for a successful application in solar cells, J_0 should not exceed values of ~100 fA/cm². We measure J_0 values of ~200 fA/cm² for the samples coated with PEDOT:PSS directly after the SiN_x deposition on the opposite surface. However, waiting for 10 minutes after an additional HF dip prior to the PEDOT:PSS deposition leads to significantly lower J_0 values of (80 – 130) fA/cm². Note that 10 minutes in air is the minimal time between HF dip and PEDOT:PSS deposition limited by the accessible laboratory infrastructure. The lowest J_0 values of below 50 fA/cm² are measured for the 30-days stored samples. The other three SiO_x tunneling layers show much higher J_0 values in the range of (400 – 1200) fA/cm² and are hence not suitable for the application to high-efficiency solar cells. Note that the measured J_0 values also include the non-negligible recombination losses of the SiN_x-passivated surface of the samples, which is ~20 fA/cm². The reported J_0 values are hence upper limits to the true J_0 values of the PEDOT:PSS/c-Si junction. The lowest J_0 value of 46 fA/cm² was achieved by storing the samples for ~30 days in air.

Re-passivated samples show J_0 values in the range between 116 and 140 fA/cm² for all treatments except for the thermally grown SiO_x, where the J_0 values are the range between 320 and 440 fA/cm². Re-passivation is performed by removing the PEDOT:PSS in water. After an HF-Dip, PEDOT:PSS is spin-coated onto the silicon surface and subsequently annealed.

4.6.3 Contact resistance

As shown in Sections 4.6.1 and 4.6.2, the optimal procedure towards low J_0 are (i) application of our *optimized* PEDOT:PSS dispersion and (ii) the formation of a native SiO_x as treatment prior to the PEDOT:PSS deposition. As described in Section 4.6.2, the saturation current density has lowest values for a native SiO_x formed at least for 20 hours storage in air. However, the efficiency of our *BackPEDOT* solar cells is so far limited by the increased series resistance, as described in Chapter 4.5.3. In the following, we examine the impact of the formation time of the native SiO_x in air on the contact resistance R_C. Native SiO_x is grown in air for 10 mins, 1 day and 4 days after a 1% HF dip for 2 mins.

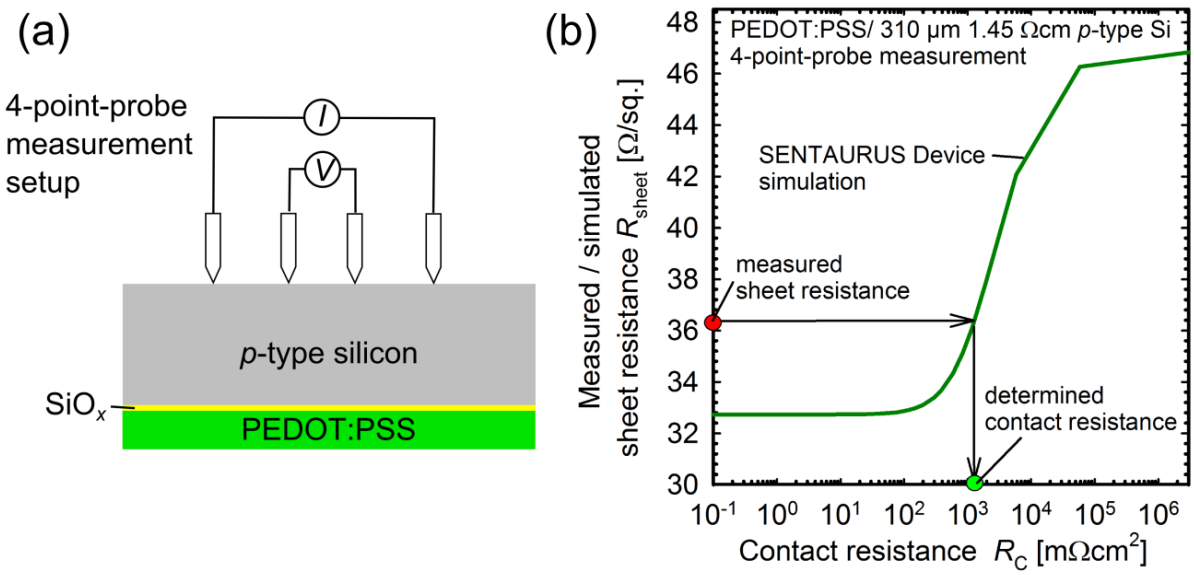

Figure 35: (a) Schematic drawing of the test sample and the measurement setup for the determination of the contact resistance R_C. (b) SENTAURUS Device simulated sheet resistance (R_{sheet}) to determine the R_C value.

In order to extract the contact resistance R_C, we apply the method introduced by Römer et al. [74]. Figure 35 (a) shows a schematic drawing of the R_C test sample and the measurement setup for the determination of the contact resistance R_C. The determination of an R_C value, visualized by Figure 35 (b) using an exemplary test structure, will be explained in following.

First, we determine input parameters for our SENTAURUS Device simulation. These are the sheet resistance of the PEDOT:PSS layer R_{sheet_PEDOT} and the sheet resistance of the silicon wafer R_{sheet_Si}. To determine R_{sheet_PEDOT} we use reference test samples. The base of these test samples is virtually un-doped *p*-type silicon with a resistivity of 150 Ωcm and a thickness of 300 µm. PEDOT:PSS is deposited on the rear surface of the silicon sample using a spin-coater. We measure R_{sheet} of our PEDOT:PSS/c-Si sample using a Sinton lifetime tester (WCT-120, Sinton instruments). The measured R_{sheet} equals the sheet resistance of the PEODT:PSS layer R_{sheet_PEDOT}, since the conductance of the PEDOT:PSS layer is two orders of magnitude larger compared to that of the 150 Ωcm silicon wafer. The sheet resistance R_{sheet_Si} of the *p*-type silicon wafer with a resistivity of 1.45 Ωcm and thickness of 310 µm – which is used as the base material for our R_C test sample – is measured using a 4-point-probe setup (RT-70/RG-7, *Napson Corporation*).

Second, R_{sheet} of the PEDOT:PSS/c-Si R_C test sample – as it would be measured with 4-point-probe setup – is simulated with SENTAURUS Device [74]. Figure 35 (b) shows the simulated R_{sheet} value as a function of R_C as a green line. Third, the sheet resistance R_{sheet} of our PEDOT:PSS/c-Si test sample is measured using a 4-point-probe setup as shown in Figure 35 (a). The measured R_{sheet} value is shown in Figure 35 (b) as a red circle. Fourth, the red circle is shifted horizontally along the black arrow until it crosses the simulated (green) line. Fifth, the crossover point of the measured R_{sheet} and simulated R_{sheet} value correspond to the sought R_C value. The two limiting cases are: (i) $R_C \rightarrow \infty \Rightarrow R_{sheet} \approx R_{sheet_Si} \approx$ 47 Ω/□ and (ii) $R_C \rightarrow 0 \Rightarrow R_{sheet} \approx 1/(1/R_{sheet_Si}+1/R_{sheet_PEDOT}) \approx$ 32 Ω/□ assuming a typical R_{sheet_PEDOT} = 100 Ω/□.

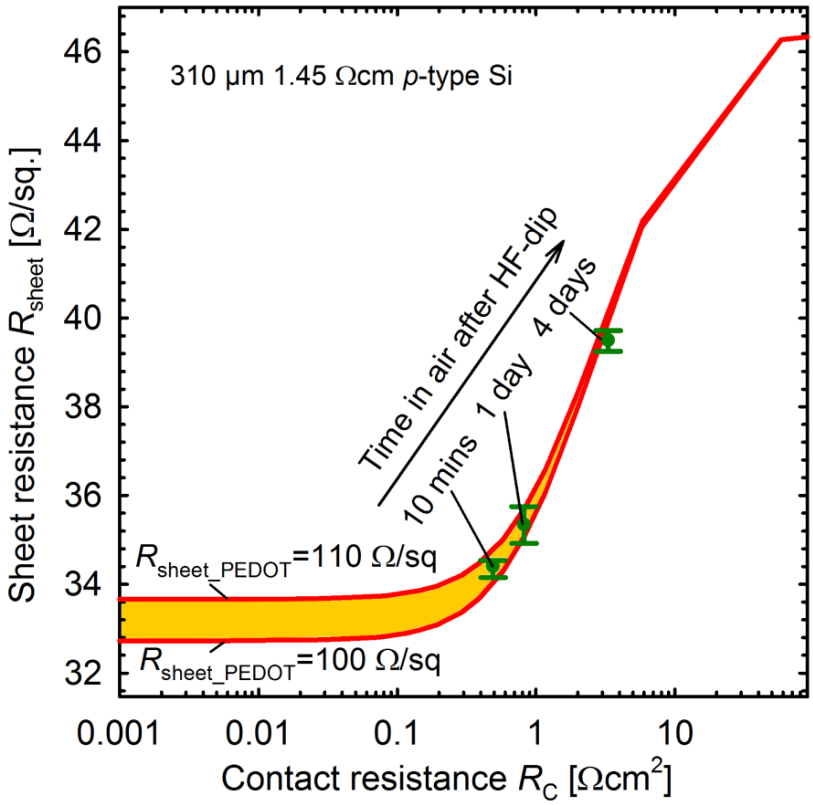

Figure 36: Measured (green symbols) and simulated (red lines) 4-point-probe sheet resistance R_{sheet} measurements as a function of the contact resistance R_C for three storage times in air after an HF dip prior to the PEDOT:PSS deposition.

In order to determine the contact resistance R_C of the PEDOT:PSS/c-Si interface, we apply the method as described above. After an RCA cleaning and an HF dip (1% HF solution, 1 minute) we deposit PEDOT:PSS onto one side of the silicon wafers after (i) 10 minutes, (ii) 24 hours, and (iii) 4 days storage in ambient air. Afterwards, we measure the sheet resistance R_{sheet} with a 4-point-probe setup (RT-70/RG-7A, *Napson Corporation*) on the uncoated side of the wafer. The measured R_{sheet} values are shown as green symbols in Figure 36. The error bars represent the standard deviation of four measurements on the same sample. The 4-point-probe sheet resistance is simulated in dependence of the interface contact resistances R_C using SENTAURUS device. The simulation results are shown as red lines in Figure 36 for typical sheet resistances of our PEDOT:PSS layers in the range of between 100 and 110 Ω/□.

Comparing the measured with the simulated R_{sheet} values, we determine contact resistances R_c of (0.49 ± 0.21) Ωcm², (0.82 ± 0.27) Ωcm² and (3.3 ± 0.4) Ωcm² for the 10 minutes, 24 hours and 4 days stored samples, respectively [73]. It becomes obvious that the contact resistance between the silicon wafer and the PEDOT:PSS layer increases with an extended native SiO_x formation time in air.

Consequently, for achieving a low series resistance the formation time of a native SiO_x has to be chosen as short as possible.

4.6.4 Optimized organic-silicon heterojunction solar cells

In this Section, we implement the *optimized* PEDOT:PSS dispersion and our optimal silicon surface pre-treatment into the *BackPEDOT* solar cell. As base material we use *n*-type Czochralski-grown (Cz) phosphorus-doped silicon wafers with a resistivity of 5 Ωcm and thicknesses of 300 µm and 160 µm, as well as *p*-type Float-zone (FZ) boron-doped silicon wafers with resistivities of 0.5 Ωcm and 1.5 Ωcm, and a thickness of 300 µm. More details on our *BackPEDOT* solar cell fabrication sequence were given in Chapter 4.5. As reference process we fabricate two PERC solar cells, as described in Chapter 3.2. As the base material for our PERC solar cells we use 0.5 Ωcm *p*-type FZ silicon. After the front surface of the *BackPEDOT* solar cells is finished, all samples are dipped in a 1% HF solution for 1 min. After the HF dip, some samples are processed within one hour while other samples are kept in air for ~ 48 hours. Next, a PEDOT:PSS layer is deposited via spin-coating onto the entire rear surface at 500 revolutions per minute (rpm) for 10 seconds and subsequently 1500 rpm for 30 seconds. Either *optimized* PEDOT:PSS or *F HC Solar* PEDOT:PSS dispersions were implemented into the *BackPEDOT* solar cells. The samples were then dried on a hotplate in air at 130°C for 15 mins to remove residual solvents. The resulting PEDOT:PSS thickness is in the range between 50 nm and 200 nm. Finally, the entire rear surface is metallized with silver (*BackPEDOT*) (*BAK 550*, *Oerlikon Balzers* AG) or aluminum (PERC reference solar cell) by means of e-gun evaporation (*BAK 600*, *Oerlikon Balzers* AG).

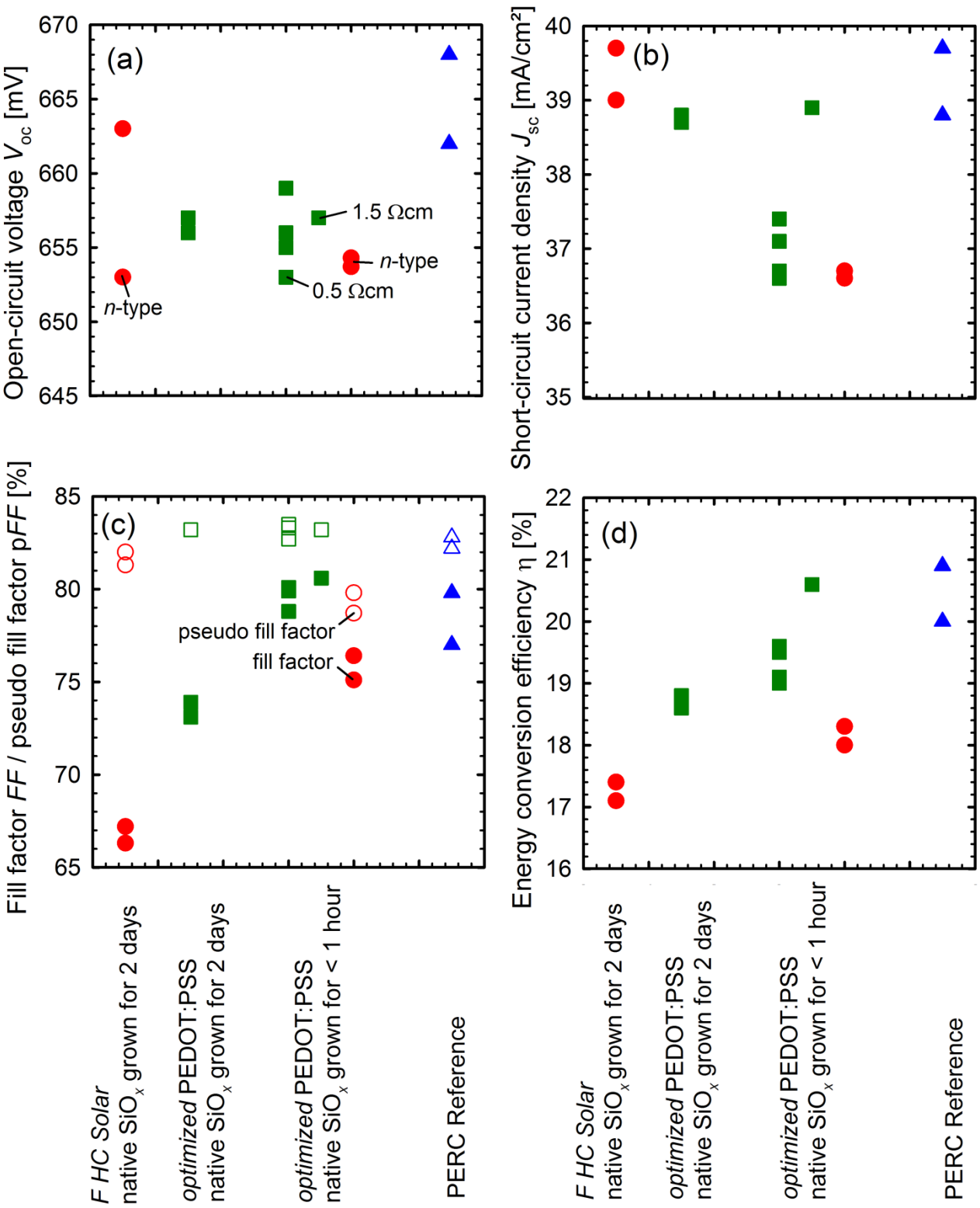

Figure 37: Measured (a) open-circuit voltages (V_{oc}), (b) short-circuit current densities (J_{sc}), (c) fill factors (filled symbols) (*FF*) and pseudo fill factors (open symbols) (p*FF*) and (d) energy conversion efficiencies (η) of *BackPEDOT* solar cells on *p*-type (green squares) and *n*-type silicon (red circles) and a PERC reference cell (blue triangles).

Table 4: Measured *BackPEDOT* and PERC solar cell parameters. The aperture cell area is 4 cm². All measurements were performed at an illumination intensity of 100 mW/cm² and a cell temperature of 25°C.

Silicon wafer	Cell type Time in air / PEDOT:PSS	V_{oc} [mV]	J_{sc} [$\frac{mA}{cm^2}$]	*FF* [%]	p*FF* [%]	η [%]	R_{s_dlt} [Ωcm²]
0.5 Ωcm *p*-type FZ-Si	PERC Reference	662	39.7	79.8	82.8	20.9	0.6
0.5 Ωcm *p*-type FZ-Si	PERC Reference	668	38.8	77.0	82.2	20.0	1.0
0.5 Ωcm *p*-type FZ-Si	<1 hour / *optimized*	659	36.6	78.8	83.3	19.0	0.9
0.5 Ωcm *p*-type FZ-Si	<1 hour / *optimized*	653	36.7	79.9	82.7	19.1	0.5
0.5 Ωcm *p*-type FZ-Si	<1 hour / *optimized*	655	37.1	80.1	83.3	19.5	0.7
1.5 Ωcm *p*-type FZ-Si	<1 hour / *optimized*	656	37.4	80.1	83.5	19.6	0.6
1.5 Ωcm *p*-type FZ-Si	<1 hour / *optimized*	657	38.9	80.6	83.2	**20.6**	0.5
1.5 Ωcm *p*-type FZ-Si	2 days / *optimized*	656	38.8	73.9	83.2	18.8	2.1
1.5 Ωcm *p*-type FZ-Si	2 days / *optimized*	657	38.7	73.1	83.2	18.6	2.2
1.5 Ωcm *n*-type Cz-Si	2 days / *F HC Solar*	653	39.7	67.2	82.0	17.4	2.9
1.5 Ωcm *n*-type Cz-Si	2 days / *F HC Solar*	**663**	39.0	66.3	81.3	17.1	3.6
5.0 Ωcm *n*-type Cz-Si	<1 hour / *optimized*	654	36.7	75.1	78.7	18.0	0.8
5.0 Ωcm *n*-type Cz-Si	<1 hour / *optimized*	654	36.6	76.4	79.8	18.3	0.7

Table 4 summarize the parameters of our *BackPEDOT* solar cells and two PERC reference solar cells. Figure 37 (a) shows the measured open-circuit voltages V_{oc} of our fabricated solar cells. V_{oc} values in the range between 653 and 663 mV are achieved with our *BackPEDOT* solar cells. The highest V_{oc} value of our *BackPEDOT* solar cell is comparable to the V_{oc} of 662 mV and 668 mV of the PERC reference. The similar V_{oc} values of our state-of-the-art Al_2O_3/SiN_x rear-surface-passivated PERC solar cell and the *BackPEDOT* cells highlight the excellent passivation quality of our organic-silicon junction. Furthermore, no relevant differences are observable between *n*-type and *p*-type silicon wafers as well as between solar cells on silicon wafers of different doping concentrations.

Figure 37 (b) shows the measured short-circuit current-densities J_{sc} of the fabricated solar cells. The PERC reference cell shows a high J_{sc} value of 39.7 mA/cm², whereas the J_{sc} values of our *BackPEDOT* cells is in the range between 36.6 mA/cm² and 39.7 mA/cm². We observe that J_{sc} depends on the type of pre-treatment and on the PEDOT:PSS composition. The highest J_{sc} values of 39.0 mA/cm² and 39.7 mA/cm² are achieved with native SiO_x grown for two days in combination with *F HC Solar* PEDOT:PSS. For *BackPEDOT* cells with native SiO_x grown for two days and *optimized* PEDOT:PSS we measure slightly reduced J_{sc} values of 38.7 and 38.8 mA/cm². Optimally processed silicon in combination with the *optimized* PEDOT:PSS results in J_{sc} values between 36.6 and 38.9 mA/cm², with a median value of 37.1 mA/cm² (9 *BackPEDOT* solar cells). The reason for the 2 mA/cm² reduced J_{sc} values of the optimally treated silicon in combination with the *optimized* PEDOT:PSS compared to the native SiO_x grown for two days with *F HC Solar* PEDOT:PSS is a topic of ongoing research. The differences in the adhesion properties between native SiO_x and the optimally pre-treated silicon surface may cause different thicknesses of the final PEDOT:PSS layer, which acts as parasitic light absorber [66].

Figure 37 (c) shows the fill factors (*FF*) (filled symbols) and pseudo fill factors (p*FF*) (open symbols) of our solar cells. The lowest *FF* values of 66.3% and 67.2% are measured on solar cells with native SiO_x plus *F HC Solar* PEDOT:PSS. The low *FF* is caused by increased series resistance (R_s) values of 2.9 and 3.6 cm², respectively. By optimizing the PEDOT:PSS composition, the *FF* was increased to values of 73.1% and 73.9%. The highest *FF* values between 78.8% and 80.6% were achieved by combining the silicon surface with a native SiO_x grown for less than 1 mins with the *optimized* PEDOT:PSS composition. On *n*-type silicon we observe lower *FF*s of 75.1% and 76.4% for our silicon surface with a native SiO_x grown for less than 1 mins with the *optimized* PEDOT:PSS composition caused by lower p*FF* values of 78.7 and 79.8%. The most likely reason for the reduced

p*FF* values are shunts within the PEDOT:PSS/c-Si interface. The *p*-type *BackPEDOT* and PERC solar cells show p*FF* values larger than 82.7%. Importantly, all 7 *BackPEDOT* solar cells with *p*-type silicon surfaces with a native SiO_x grown for less than 1 hour in combination with the *optimized* PEDOT:PSS show R_s values < 1 Ωcm².

Figure 37 (d) shows the measured one-sun energy conversion efficiency η of the fabricated solar cells. The efficiency follows the *FF* trend, where the shunted organic-silicon interface limits our *n*-type silicon *BackPEDOT* solar cells to η values of up to 18.3%. Consequently, for our optimally treated silicon surface with a native SiO_x grown for less than 1 hour plus the *optimized* PEDOT:PSS composition, we achieve outstanding efficiencies in the range between 19.0% and 20.6% on *p*-type silicon wafers, which are by far the highest efficiencies for organic-silicon solar cells to date [72].

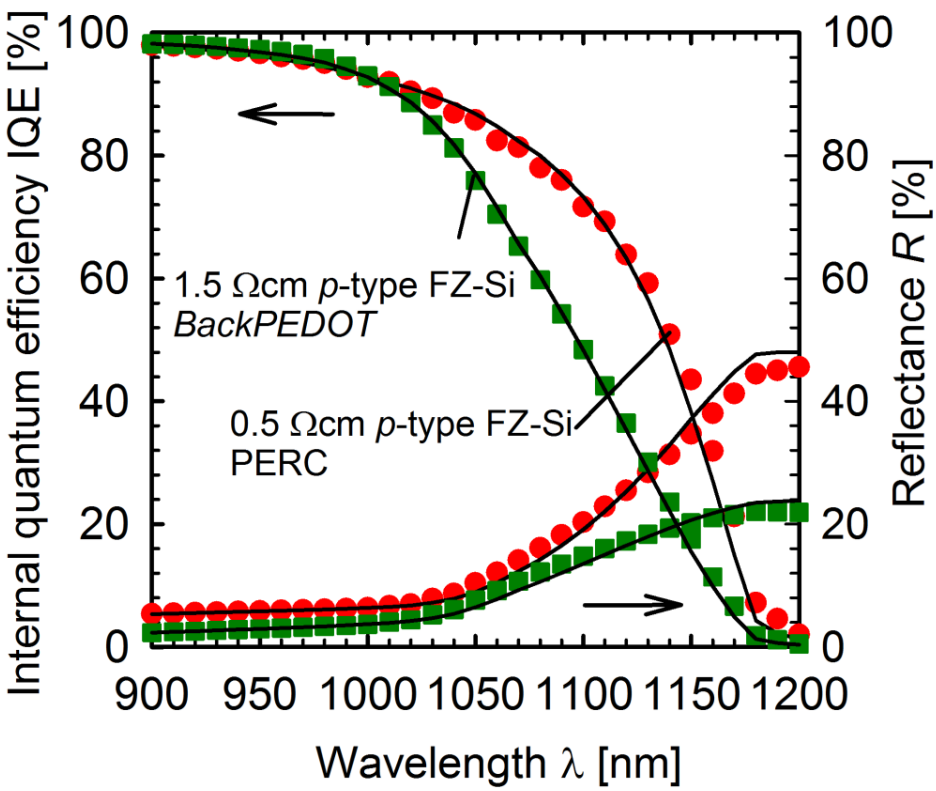

Figure 38: Measured spectrally resolved internal quantum efficiency IQE(λ) and reflectance *R*(λ) of our best *p*-type silicon *BackPEDOT* cell (green squares) in comparison with a PERC reference solar cell (red circles).

Figure 38 shows the measured spectrally resolved internal quantum efficiency [IQE(λ)] and the reflectance [*R*(λ)] of our best *BackPEDOT* cell (green squares) in comparison with the PERC reference cell (red circles). In the wavelength (λ) range between 900 and 1000 nm our *BackPEDOT* solar cell shows a very similar performance as the Al_2O_3/SiN_x-passivated PERC solar cell. In this λ range, the IQE(λ) curve is dominated by the rear surface recombination velocity S_{rear}. Using a parameter-confidence-plot, we determined S_{rear} values of (190 ± 60) cm/s and (165 ± 40) cm/s for the PERC and *BackPEDOT* cells, respectively. Note the relatively large uncertainty of the S_{rear} values that mainly originates form the non-optimal fit of the reflectance curves. Lower IQE(λ) values for the *BackPEDOT* solar cell at λ > 1000 nm lead to a reduced J_{sc} value. We attribute the lower IQE(λ) values of the *BackPEDOT* cell compared to the PERC reference to the non-optimized PEDOT:PSS layer thickness and hence a pronounced parasitic absorption within the PEDOT:PSS.

4.7 Chapter summary

We performed an in-depth investigation of the PEDOT:PSS/c-Si heterojunction. Using PCD measurements we determined for the first time the J_0 values of PEDOT:PSS/c-Si heterojunctions. We measured a J_0 value of 208 fA/cm² on the RP-textured silicon surface, and a J_0 value of 80 fA/cm² on a planar silicon surface, respectively. We have fabricated heterojunction solar cells with PEDOT:PSS on the *n*-type silicon wafers front surface and achieved a record efficiency at that time of 12.3%. This record-high efficiency was achieved by implementing an RP-texture on the front surface and an n^+-BSF on the rear surface. We have investigated the optical properties of the PEDOT:PSS layer via ellipsometry and transmission measurements. We performed ray-tracing simulations of a solar cell where the PEDOT:PSS layer is on the RP-textured front surface of a solar cell or on the planar rear surface. Optical measurements in combination with ray-tracing simulations have shown that the solar cell with PEDOT:PSS layer on the RP-textured front surface could realistically reach a J_{sc} of 34.1 mA/cm², and the solar cell with PEDOT:PSS layer on the planar rear surface could realistically reach a J_{sc} of 40.5 mA/cm². We have hence introduced a novel solar cell concept – the so-called *BackPEDOT* solar cell – where the advantage of a PEDOT:PSS layer on the planar rear could realistically reach a J_{sc} of 40.5 mA/cm², a V_{oc} of 667 mV and an efficiency of 22%.

We have realized our first *BackPEDOT* experimental devices, which achieved a remarkably high V_{oc} of 663 mV and a J_{sc} of 39.7 mA/cm^2. The *J-V* curves showed a good pseudo fill factor of up to 82.0%. However, the actual fill factors were largely limited by a high series resistance which was in the range between 2.88 Ωcm² and 3.35 Ωcm^2. By optimizing the PEDOT:PSS dispersion and the silicon surface pre-treatment we were able to achieve J_0 values of 46 fA/cm² and R_C values of 490 mΩcm². We successfully implemented our optimal silicon treatment which is a native SiO_x grown for less than 10 mins and the *optimized* PEDOT:PSS composition to *BackPEDOT* solar cells and achieved R_s values < 1 Ωcm² and V_{oc} values between 653 and 659 mV. Our lowest series resistance of 0.5 Ωcm² resulted in a *FF* of 80.6%. Combining the high *FF* value with a short-circuit current density of 38.9 mA/cm², an outstanding efficiency of 20.6% was experimentally achieved, which is by far the highest efficiency for any organic-silicon heterojunction solar cell to date.

Figure 39 shows published solar cell efficiencies (η) of PEDOT:PSS/c-Si solar cells based on silicon wafers over the time period from 2011 to 2015. Details on the published results are given in Table 5. Hybrid solar cells with efficiencies exceeding 10% [52] were realized for the first time in 2011 when PEDOT:PSS was deposited onto the front of *n*-type silicon wafers. Further optimization of the PEDOT:PSS dispersion [75] and/or implementation of an interfacial layer between silicon and PEDOT:PSS layer [54] resulted in a constant improvement in efficiency over the following years. However, parasitic light absorption of the PEDOT:PSS layer on the front and recombination losses at the insufficiently passivated rear surface limited the efficiency typically to values below 14%. Within this thesis, a substantial boost in the efficiency was achieved in 2014 by implementing the PEDOT:PSS layer at the planar rear surface, the so-called *BackPEDOT* concept [66]. In this thesis, efficiency of *BackPEDOT* heterojunction solar cells was very recently further increased from 17.4% [66] to 20.6% [72] by (i) adopting the PEDOT:PSS dispersion [63] and (ii) optimizing the silicon surface pre-treatment [73].

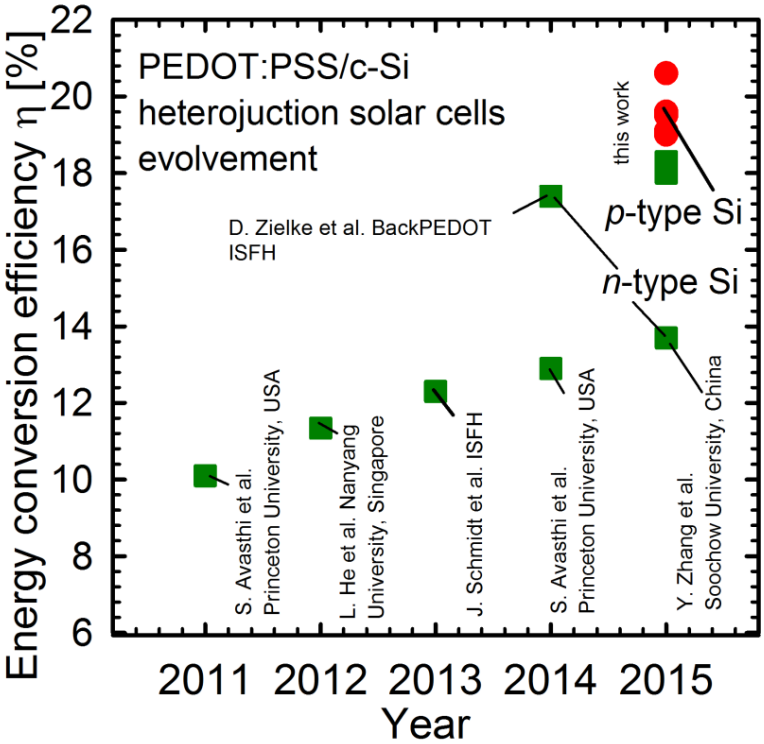

Figure 39: Reported solar cell efficiencies of PEDOT:PSS/c-Si solar cells based on *n*-type (green squares) and *p*-type (red circles) silicon wafers.

Table 5: Evolution of PEDOT:PSS/c-Si solar cells over time.

Authors	Innovation	Year	V_{oc} [mV]	J_{sc} $\left[\frac{mA}{cm^2}\right]$	*FF* [%]	η [%]
Avasthi et al. [52]	Silicon wafer as base material	2011	590	29.0	59.0	10.1
He et al. [54]	Native SiO_x as passivating interface between silicon and PEDOT:PSS	2012	600	26.3	70.9	11.3
Schmidt et al. [69]	Random-pyramid-textured front surface and back-surface-field	2013	603	29.0	70.6	12.3
Avasthi et al. [76]	TiO_2 passivating layer on the rear surface	2014	620	29.0	72.1	12.9
Zielke et al. [66]	*BackPEDOT* concept with PEDOT:PSS on planar rear	2014	653	39.7	67.2	17.4
Zielke et al. [72]	*BackPEDOT* with optimal pre-treated *p*-type silicon surface and *optimized* PEDOT:PSS	2015	657	38.9	80.6	20.6

5 PEDOT:PSS junction: degradation and stabilization

In this Chapter, we discuss the long-term stability of PEDOT:PSS/c-Si heterojunctions. The stability of organic-silicon solar cells in air and in a humidity-free environment is investigated on a time scale of up to three years. During this time span, *J-V* measurements are performed to monitor the degradation behavior of the solar cells. We observe that our organic-silicon solar cells show a rapid degradation in air. However, the absence of humidity drastically improves the stability. For the first time, we propose encapsulation methods and demonstrate long-term stability of encapsulated organic-silicon heterojunction solar cells. Finally, we discuss different possible degradation mechanisms.

5.1 Evolution of efficiency

In this Section, we examine the long-term stability of *FrontPEDOT* and *BackPEDOT* solar cells in terms of the relative energy conversion efficiency. For this purpose, we store the solar cells in air at approximately 23°C and 65% relative humidity.

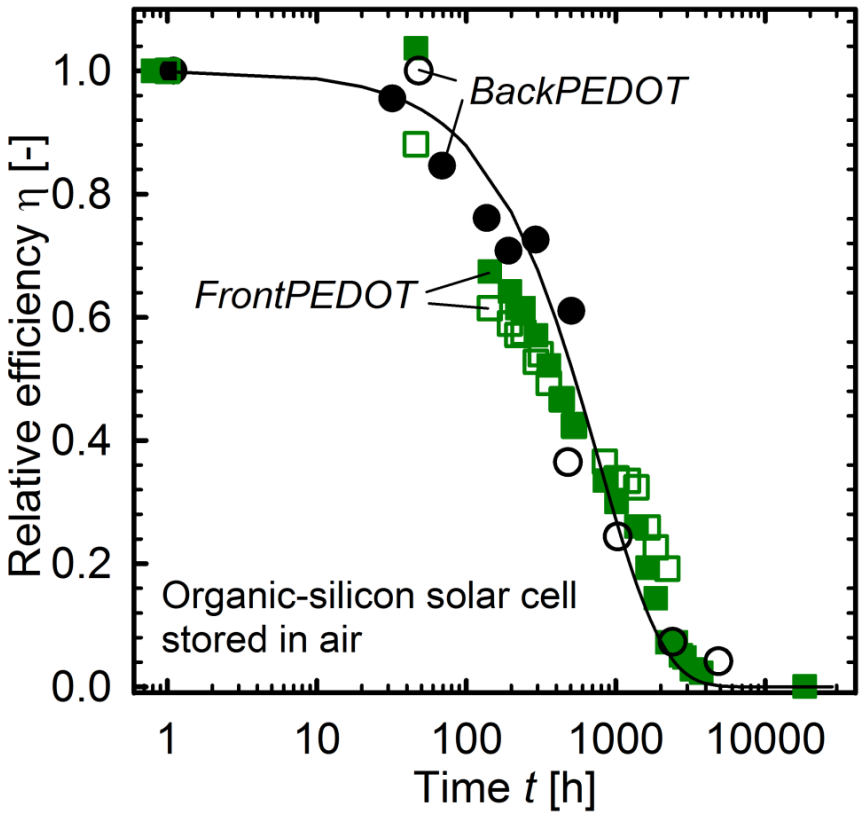

Figure 40: Relative efficiency of two *FrontPEDOT* (green squares) and of two *BackPEDOT* (black circles) solar cells stored in air. The black line is an exponential decay fit.

Figure 40 shows the relative energy conversion efficiency η of two *FrontPEDOT* (green squares) and two *BackPEDOT* (black circles) solar cells as a function of storage time. The efficiency is stable for both types of solar cells for up to 20 hours in ambient air. After this period we observe a rapid degradation in the efficiency for all cells. After ~ 3000 hours in ambient air the efficiency drops to zero. This degradation can be fitted by a simple exponential decay $\eta_{\mathrm{relative}}(t) = e^{-t/t_{\mathrm{deg}}}$ as shown by the black line in Figure 40 with an average time constant of $t_{\mathrm{deg}} = (28 \pm 1.6)$ days. As will be discussed further below in more detail, the humidity plays a major role in the observed degradation during storage.

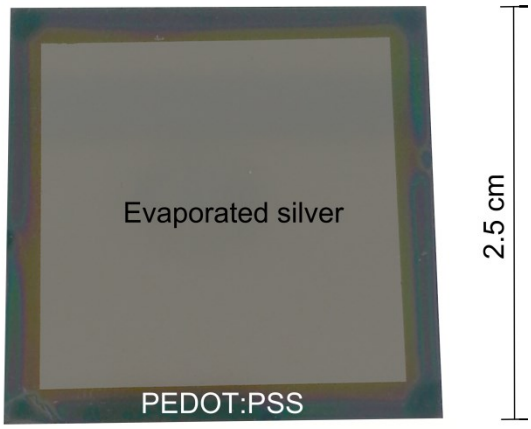

Figure 41: Photograph of the rear side of a *BackPEDOT* solar cell with the total size of 2.5 × 2.5 cm². PEDOT:PSS is deposited on the entire rear surface. The evaporated silver do not completely covers the entire PEDOT:PSS layer.

Surprisingly, the observed decay behavior is similar for both types of solar cells: *FrontPEDOT* and *BackPEDOT* solar cell, which means that the metal layer covering the PEDOT:PSS on the rear surface of the *BackPEDOT* solar cells has no beneficial effect concerning the stability. This might be explained by the fact that in our present *BackPEDOT* solar cells design, the metal layer does not completely cover the PEDOT:PSS layer. Figure 41 shows a photograph of the rear side of a *BackPEDOT* solar cell. We observe that at the edge the PEDOT:PSS layer is not covered by the Ag layer due to our metallization setup. Therefore, the PEDOT:PSS layer at the edge is exposed to the ambient air. As known from the literature [56] PEDOT:PSS is highly hygroscopic. Therefore, exposing one part of the PEDOT:PSS layer to a humid environment leads to an immediate saturation of the entire PEDOT:PSS bulk. Furthermore, the reduced light exposure during the illuminated *J-V* measurement of the *BackPEDOT* solar cell compared to the *FrontPEDOT* device has no significant effect on the degradation behavior and the doping of the c-Si wafer does not affect the degradation behavior as well.

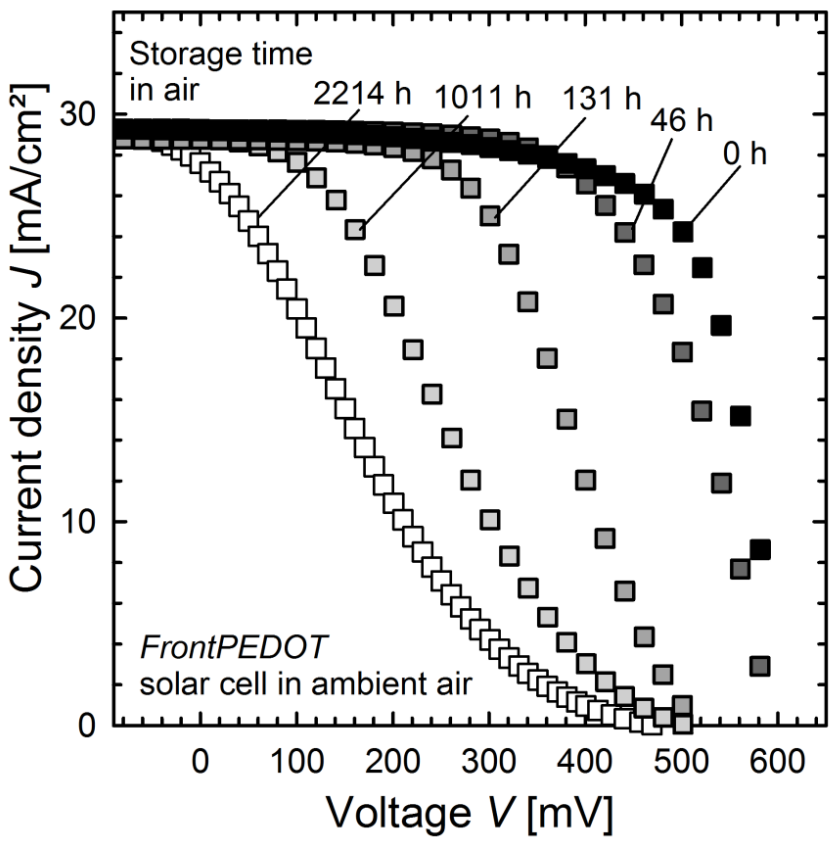

Figure 42: Illuminated *J-V* characteristics measured at STC of a *FrontPEDOT* solar cell as a function of storage time in ambient air.

Figure 42 shows the measured illuminated *J-V* curves of a *FrontPEDOT* solar cell as a function of the storage time in ambient air. A so-called '*S*-shaped' *J-V* curve forms during degradation. The hump in the *S*-shaped *J-V* curve shifts to lower voltages with progressing degradation. Consequently, the apparent series resistance at maximum power point increases drastically from 0.99 Ωcm² to 6.17 Ωcm^2 after 1011 hours of storage in ambient air, reducing the fill factor from 69.6% to 28.4%. Note that *S*-shaped *J-V* curves have also been reported for other organic solar cells [77], where they have been attributed to the formation of interface dipoles between the PEDOT:PSS and the absorber [78], [79] or with the increased recombination caused by an increased density of interface states [80], [81]. Additionally, *S*-shaped *J-V* curves are frequently associated with barriers at a-Si:H/c-Si interfaces [82]. Therefore, in this thesis we will propose a new model of the degradation mechanism of the PEDOT:PSS/c-Si heterojunction (see Section 5.3). Another degrading solar cell parameter is the open-circuit voltage V_{oc}. The V_{oc} value degrades from initially 601 to 505 mV after 1001 hours of storage in ambient air. For *BackPEDOT* solar cells we observe a comparable long-term behavior regarding the shape of the *J-V* curve.

The increased series resistance can be a result of an increased sheet resistance (R_{sheet}) of the PEDOT:PSS layer and/or an increased contact resistance (R_C) of the PEDOT:PSS/c-Si interface. In the following, we hence determine both resistance values as a function of the storage time in air.

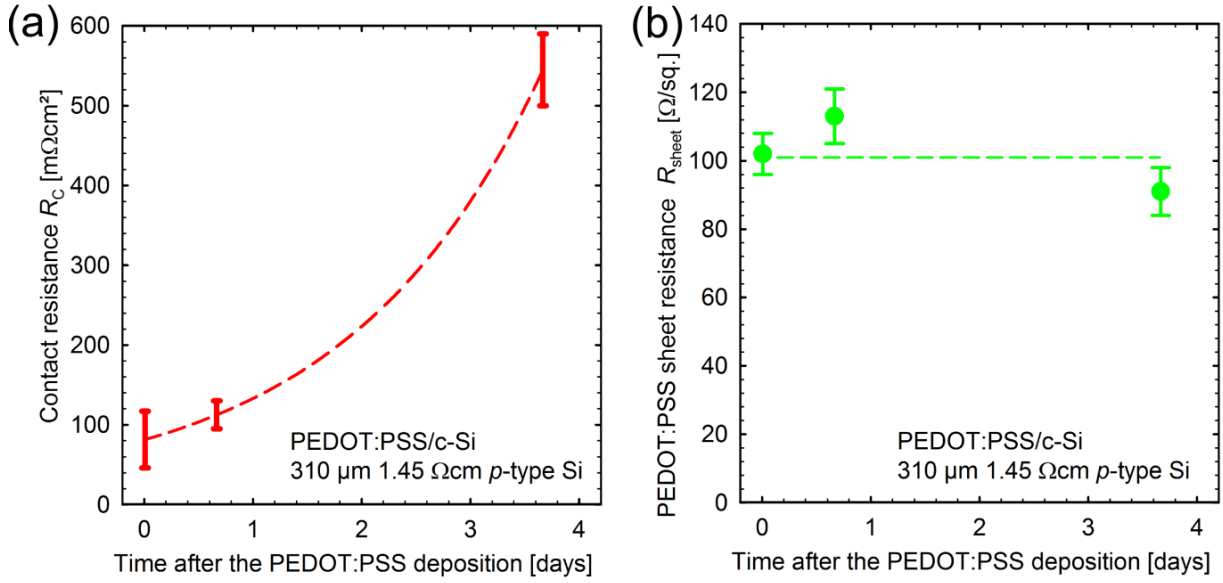

Figure 43: (a) Measured contacts resistance (R_C) between PEDOT:PSS and silicon as a function of time in air. (b) Measured sheet resistance (R_{sheet}) of the PEDOT:PSS layer as a function of time in air. Dashed lines are guide-to-the-eyes.

The contact resistance is determined as described in the Section 4.6.3. After an RCA cleaning and an HF dip (1%, 1 minute) we deposit PEDOT:PSS onto one side of the silicon wafers within 10 minutes. After PEDOT:PSS deposition the sample is annealed at 130°C for 15 mins in air. R_{sheet} and R_C values are measured after storing the PEDOT:PSS/c-Si samples for 10 minutes, 16 hours, and 88 hours in ambient air. The error bars represent the standard deviations of four measurements on the same sample.

Figure 43 (a) shows R_C values as a function of time in air. The R_C values of PEDOT:PSS/c-Si samples are (82 ± 5) mΩcm², (110 ± 50) mΩcm², and (545 ± 50) mΩcm² after 10 minutes, 16 hours and 88 hours storing in ambient air, respectively [63]. The contact resistance between the silicon wafer and the PEDOT:PSS layer increases by a factor 8 after 88 hours in ambient air. Figure 43 (b) shows measured R_{sheet} values as a function of time in air. The R_{sheet} values of the PDOT:PSS layer are (102 ± 6) Ω/□, (113 ± 8) Ω/□, and (91 ± 7) Ω/□ after 10 minutes, 16 hours and 88 hours storage in ambient air, respectively [63]. The sheet resistance of the PEDOT:PSS layer decreases by a only $12\%_{rel}$ after 88 hours in ambient air, which is well within the experimental scatter. We conclude that the degradation of the organic-silicon solar cells is caused by an increasing contact resistance between at the PEDOT:PSS and the silicon wafer.

5.2 Effect of encapsulation and storage in a humidity-reduced environment

In this Section, we compare the degradation behavior of solar cells in ambient air and in a dehumidified environment and propose cell encapsulation using ALD-Al_2O_3 or a metal foil.

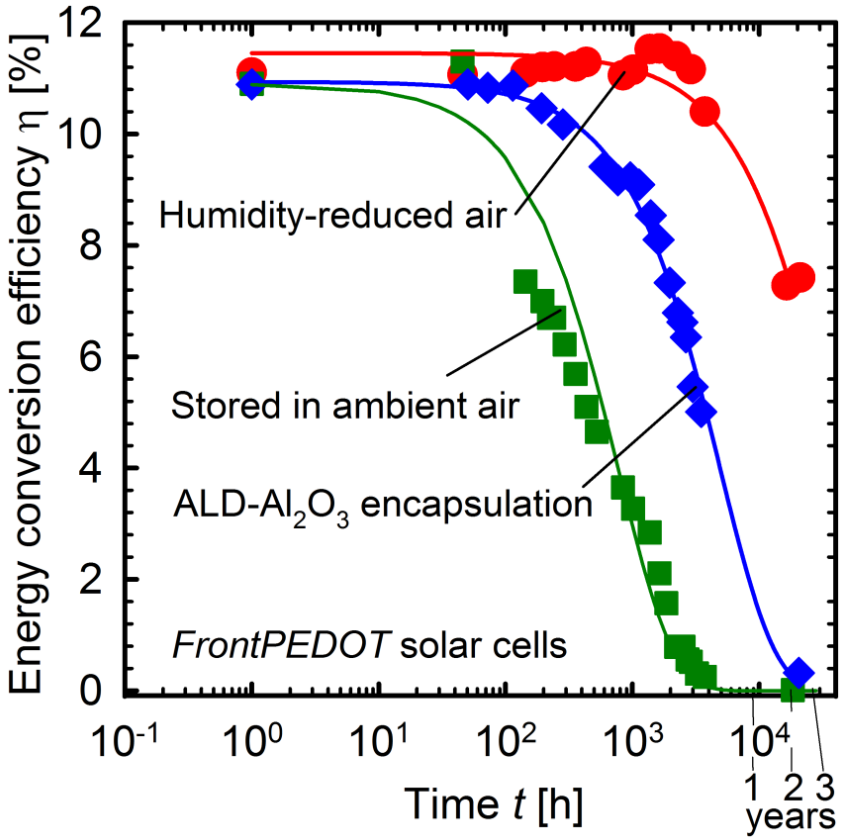

Figure 44: Measured one-sun efficiencies of *FrontPEDOT* solar cells of comparable initial efficiency as a function of storage time in darkness. The cells are stored in air (green squares) and in a desiccator in humidity-reduced air (red circles). The stability is improved by encapsulating the cells with ALD-Al_2O_3 (blue diamonds). The lines are exponential fits to the measured decay curves.

Figure 44 shows the measured efficiency evolution of 3 representative organic-silicon front junction solar cells with a comparable initial efficiency of 11% during storage in darkness at room temperature. A pronounced degradation in the cell efficiency is observed for the cell which is stored in air (green squares), whereas the cell which is stored in a humidity-reduced air in a desiccator does not show degradation for a time scale for up to 3000 hours (red circles). Please note that each measurement requires removal of the samples from the desiccator. Therefore, an exposure of the samples to ambient air during the measurement is inevitable. Degradation after 3000 hours is hence probably caused by absorbing moisture during each measurement. This experimental finding suggests that the observed degradation is caused by the interaction of the PEDOT:PSS/c-Si junction and/or PEDOT:PSS bulk material with water molecules from the atmosphere [69].

In order to improve the stability of our organic-silicon solar cells, we have encapsulated the devices with a 30 nm thick Al_2O_3 film deposited by plasma-enhanced ALD at 30°C (see Chapter 3.1.2.2).

ALD is known to result in highly conformal, very dense, pin-hole-free layers and Al_2O_3 deposited by ALD had already been successfully applied for the encapsulation of organic solar cells [83]. Indeed, we observe a pronounced improvement in stability after encapsulation of our organic-silicon solar cells with ALD-Al_2O_3, as can be seen in Figure 44 (blue diamonds). Exponential fits $\eta(t) = \eta_0 \times \exp(-t/t_{deg})$, where η_0 is the initial efficiency and t is the time, to the measured efficiency decay curves in Figure 44 (lines) result in degradation time constants t_{deg} of 28 days for the cell without encapsulation and $t_{deg} = 203$ days for the Al_2O_3-encapsulated cell. This result demonstrates that the applied ALD-Al_2O_3 encapsulation is protecting the device against humidity. The solar cell stored in a desiccator show an t_{deg} of 1615 days. However, further optimization of the encapsulation layer is required to fully stabilize the organic-silicon devices.

Therefore, we propose a new encapsulation method based on a metal foil. This encapsulation method is suitable for our *BackPEDOT* solar cells.

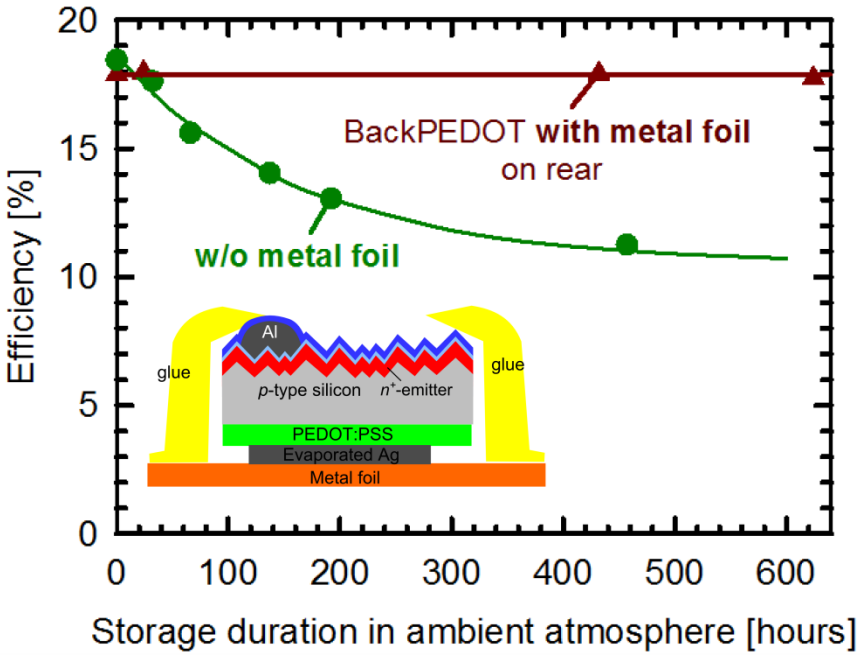

Figure 45: First long-term stable *BackPEDOT* solar cell with metal foil on the rear [84]. The inset shows a schematic of a *BackPEDOT* solar cell encapsulated with a metal foil on the rear. The edges of the solar cell are sealed with glue.

The inset in Figure 45 shows one possible encapsulation method of our *BackPEDOT* solar cells using a metal foil and glue to seal the edges. We use a copper foil covering the rear surface of our *BackPEDOT* cell. The glue was distributed at the edge of solar. Figure 45 shows first results regarding the stability of the efficiency in air. We observe a stable efficiency within 600 hours of our *BackPEDOT* solar cell encapsulated with a metal foil compared to a *BackPEDOT* solar cell without a metal foil. Optimization of encapsulation methods is the topic of an ongoing research [84].

5.3 Degradation mechanisms

In the previous Section, we have discovered a humidity-related degradation of the efficiency of our organic-silicon solar cells. An increased contact resistance was identified as the most affected solar cell parameter in the course of degradation. Based on this observation we conclude that the carrier transport between PEDOT:PSS and silicon alters during the degradation process. In the following, we will discuss two possible mechanisms which alter the charge carrier transport and therefore R_s and *FF*.

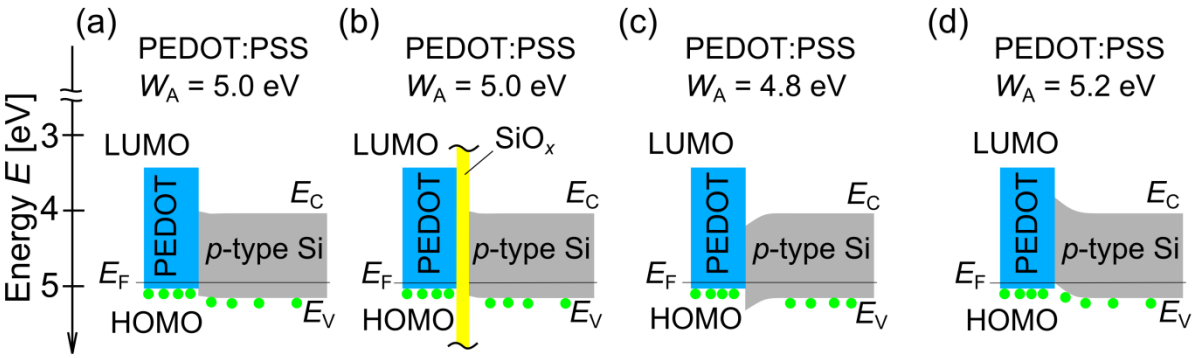

Figure 46: Band diagrams of the PEDOT:PSS/c-Si interface (a) at thermodynamic equilibrium, (b) with a SiO_x layer between PEDOT:PSS and silicon and (c), (d) with an altered PEDOT:PSS/c-Si band configuration due to a shift of the PEDOT:PSS work function. The filled forms represent the band gaps (E_G) of silicon (grey form with E_G = 1.12 eV) and PEDOT:PSS (blue form with E_G = 1.6 eV). The green dots symbolize holes.

Figure 46 (a) shows the band diagram of the rear surface of our *BackPEDOT* solar cell in the initial state at thermodynamic equilibrium. The difference between HOMO and LUMO levels (the bandgap) of PEDOT:PSS is 1.6 eV [56]. The work function W_A of PEDOT:PSS is ~5 eV [56]. *p*-type silicon has an electron affinity χ = -4.05 eV and a band gap E_G = 1.12 eV. Since the PEDOT:PSS has a metal-like behavior, the Fermi level E_F is approximately at the HOMO level. Jäckle et al. [85] measured an offset between the Fermi-level und HOMO level of 80 meV. The filled forms represent the band gaps of silicon (grey form with E_G = 1.12 eV) and PEDOT:PSS (blue form with E_G = 1.6 eV). Using the equation:

$$E_V - E_F = qV_T ln\left(\frac{N_A}{N_V}\right), \tag{5.3.1}$$

with the thermal voltage V_T = 25.7 mV and effective density of states in the valence band $N_V = 3.1 \times 10^{19}$ cm^{-3} and the acceptor concentration in silicon N_A, we can calculate the difference between E_F and E_V. For *p*-type silicon with a resistivity of 1.5 Ωcm ($N_A = 1 \times 10^{16}$ cm^{-3}) – as typically used in this work – we calculate using equation (5.3.1) an E_F - E_V difference of 206 meV at 25°C. The resulting band diagram is shown in Figure 46 (a). This diagram is favorable for the hole extraction from silicon into the PEDOT:PSS layer. In the following we discuss two possible mechanisms which might be responsible for the observed degradation in the contact resistance.

One possible effect might be an interfacial SiO_x growth between the PEDOT:PSS and the silicon. SiO_x formation on the silicon surface during the solar cell fabrication sequence is unavoidable. Figure 46 (b) shows the band diagram of the rear surface of the *BackPEDOT* solar cell with an assumed

interfacial silicon oxide layer. The different band offsets between Si and SiO_x are 3.2 eV for conduction band and 4.7 eV for valence band [86]. Therefore, tunneling through SiO_x is less efficient for holes due to the larger barrier height. The increased SiO_x layer thickness can reduce the tunneling probability of holes and therefore be harmful to the transport property between silicon and PEDOT:PSS.

Another possibility would be an altered band configuration a the PEDOT:PSS/c-Si interface. We can exclude silicon as the material which is affected during degradation. PEDOT:PSS – as an organic layer – could be easily affected. It is well known that long-term stability is a predominant issue in organic solar cells [87]. It is also known that the work function W_A of PEDOT:PSS can be adjusted in the range of 4.7 eV to 5.6 eV [56] e.g. by varying the PEDOT:PSS ratio and by incorporation of additives. Therefore, we conclude that a drift in the work function of the PEDOT:PSS layer is a more likely reason for the observed degradation.

Figure 46 (c) and (d) show band diagrams of the rear surface of our *BackPEDOT* solar cell with a band bending caused by a hypothetical change in the work function of the PEDOT:PSS. Figure 46 shows band diagrams with (c) a decreased and (d) an increased W_A by the value of 200 meV, respectively. In the case of an increased W_A, we observe a band alignment which is favorable for hole extraction. In contrast, in the case of a decreased W_A, we observe the formation of a potential barrier for holes. We conclude, that a $W_A \geq 5$ eV is suitable for a barrier-free hole transport. A decreasing W_A of the PEDOT:PSS during degradation would lead to the formation of a potential barrier for holes. This barrier would hinder the transport of holes and would consequently increase the contact resistance.

5.3.1 First hypothesis: silicon oxide at the PEDOT:PSS/c-Si interface

Carrier transport through an ultrathin (few nm) insulating SiO_x layer can be realized by quantum-mechanical tunneling. An increased SiO_x thickness reduces the tunneling probability of holes (and electrons) and therefore, increases the series resistance. To confirm a possible degradation caused by oxidation of the silicon surface beneath the PEDOT:PSS layer, a SiO_x layer has to be detected. Therefore, we evaluate images made with transmission electron microscopy (TEM) of the degraded PEDOT:PSS/c-Si interface.

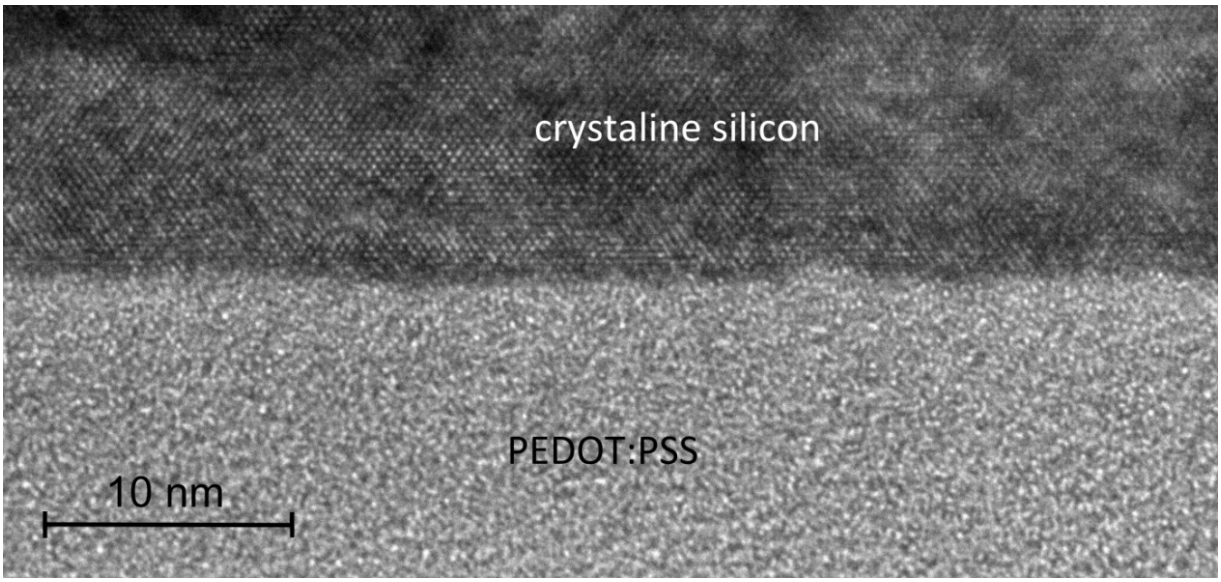

Figure 47: Transmission electron microscopy (TEM) image of a PEDOT:PSS/c-Si interface stored in air for approximately 3 months.

We examine a *p*-type silicon wafer with a resistivity of 1.45 Ωcm and a thickness of 310 µm. After RCA cleaning, a PEDOT:PSS layer is deposited on one surface of the silicon sample using a spin-coater. The time between the last HF dip (after RCA cleaning) and the PEDOT:PSS deposition was kept below 30 mins. Next, the sample is annealed in air at 130°C for 15 mins. After annealing, the sample is stored in air for approximately 3 months. This relatively long time ensures the complete electrical transport degradation of the PEDOT:PSS/c-Si interface.

Figure 47 shows a transmission electron microscopy (TEM, *Tecnai* G2 F20 TMP, FEI™) image representing a cross-section of the PEDOT:PSS/c-Si interface. The silicon area is identified by the monocrystalline arrangement of the silicon atoms. The varying brightness within the silicon area is caused by the TEM sample preparation. The PEDOT:PSS area is identified in the TEM image as an amorphous material. Although SiO_x has also an amorphous structure, we expect a different brightness in the TEM image between PEDOT:PSS and a possibly present SiO_x layer since both materials have different elemental compositions. Based on our TEM images we were not able to identify a closed SiO_x layer at the PEDOT:PSS/c-Si interface. We conclude that no closed SiO_x layer was formed at the PEDOT:PSS/c-Si interface during the storage in air for nearly 3 months.

5.3.2 Second hypothesis: drift in the PEDOT:PSS work function

As mentioned above, another possible mechanism leading to the degradation in the transport properties would be change in the band alignment due to drift in the work function of the PEDOT:PSS. To examine the validity of this hypothesis, we measure the work function of the PEDOT:PSS as a function of the storage time in ambient air.

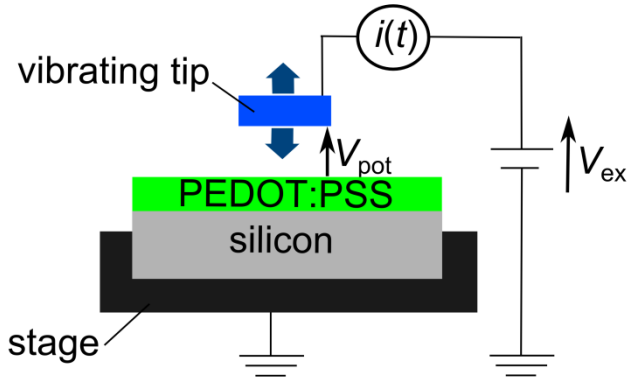

Figure 48: Schematic of the Kelvin-probe measurement setup.

Figure 48 shows a schematic of the Kelvin-probe setup (TREK 320C) to measure the potential difference V_{pot} between the vibrating tip at angular velocity ω and the sample [88], [89]. The tip is positioned in a distance of 1-2 millimeters above the sample and forms a capacitor with a capacitance C. The alternating distance changes the capacitance, which causes an alternating current $i(t)$ as a function of time t [90]:

$$i(t) = (V_{\text{pot}} - V_{\text{ex}})\omega\Delta C \cos\omega t\,, \qquad (5.3.2.2)$$

where ΔC is the change in capacitance. To extract the work function difference between tip and the sample, an external voltage V_{ex} is applied until $i(t) = 0$ at any given point in time. This is the case were V_{ex} equals V_{pot}. Please note that using this method only relative change in the work function of the sample can be measured.

The left inset in Figure 49 shows our PEDOT:PSS/c-Si test sample. We use 6'' Float-Zone (FZ) boron-doped (100)-oriented silicon wafer with a doping concentration of $N_A = 1\times10^{16}$ cm^{-3} and a thickness of 300 µm. First, the wafer is laser-cut into 2.5 × 2.5 cm² samples followed by an RCA cleaning. Next, samples are dipped in 1% diluted hydrofluoric acid (HF) for 1 min. Within 10 mins after the HF dip PEDOT:PSS is spin-coated onto the silicon sample front surface. As PEDOT:PSS dispersion we use the *optimized* solution as described above. Spin coating parameters are 500 RPM for 10 secs followed by 1500 RPM for 30 secs. After PEDOT:PSS deposition the sample is annealed on a hot plate in air at a temperature of 130°C for 15 mins. This PEDOT:PSS/c-Si interface of our sample corresponds to the interface in our organic-silicon solar cells.

The right inset in Figure 49 shows a PEDOT:PSS/Ag test sample. We cut silver foil into ~2.5 × 2.5 cm² samples and spin-coat PEDOT:PSS onto one surface of the foil. As PEDOT:PSS dispersion we use the *optimized* solution. Spin coating parameters are 500 RPM for 10 secs followed by 1500 RPM for 30 secs. After PEDOT:PSS deposition the sample is annealed on a hot plate in air at a temperature of 130°C for 15 mins.

Directly after annealing, the sample is placed on the grounded stage of our Kelvin-probe setup. The PEDOT:PSS-covered surface faces towards the vibrating tip. The external voltage signal V_{ex} was acquired every two minutes. The measurements were performed at room temperature in ambient air.

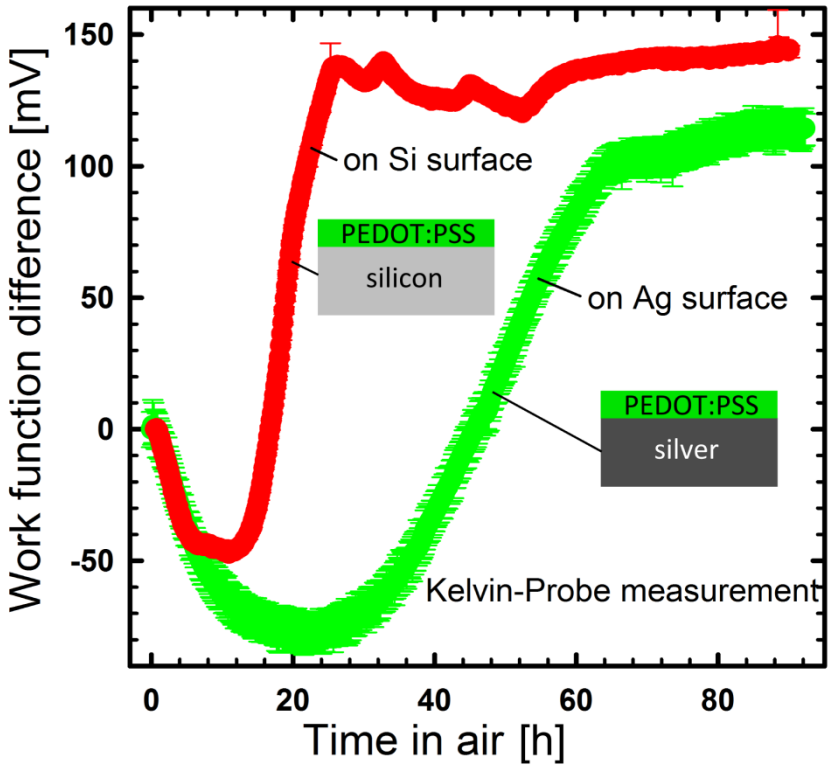

Figure 49: Work function difference between tip and PEDOT:PSS/c-Si (red symbols) and PEDOT:PSS/Ag (green symbols) test samples as a function of time in ambient air. The uncertainty represents the minimal and maximal measured values within the time interval of two minutes.

Figure 49 shows measured work function difference V_{pot} between the PEDOT:PSS and the vibrating tip as a function of time in ambient air. In the graph we set $V_{pot} = 0$ V at the time $t = 0$. For the sample where PEDOT:PSS is on top of the silicon surface (red symbols) we observe in the first 12 h a decreasing V_{pot} signal to - (39 – 50) mV compared to the initial value. In the following 14 h we observe a rise in the V_{pot} to + (119 – 150) mV compared to the initial value followed by an abrupt saturation. For the sample where PEDOT:PSS is deposited on the top of the silver foil we observe in the first 20 h a decreasing V_{pot} signal to - (67 – 86) mV compared to the initial value. In the following 40 h we observe an increase in V_{pot} to + (91 – 122) mV compared to the initial value followed by saturation.

We observe a qualitatively similar behavior for the work function differences as a function of time in ambient air for PEDOT:PSS/c-Si and PEDOT:PSS/Ag samples. Based on our observation we conclude that the change in the work function difference as a function of time in air is an intrinsic effect of the PEDOT:PSS.

In our above considerations we concluded that a reduction in the work function of PEDOT:PSS would cause a barrier for the hole transport in our *BackPEDOT* solar cells. Combining this consideration with the findings made in this Section, we conclude that the work function of our PEDOT:PSS decreases during storage in ambient air, which is also fully consistent with results based UPS measurement published in the literature [91].

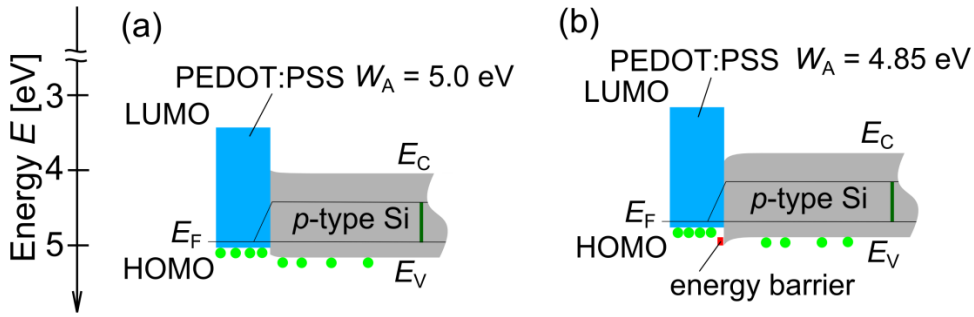

Figure 50: Energy-band alignment of a *BackPEDOT* solar cell (a) at the maximum power point (MPP) before degradation and (b) at the MPP after degradation. The dark green bar marks the quasi-Fermi level splitting which equals qV_{mpp}. The red bar marks the height of the energy barrier for holes created during the drift of the work function W_A of the PEDOT:PSS.

Figure 50 (a) shows a simplified drawing of the band diagram of a *BackPEDOT* solar cell at the maximum power point (MPP). At MPP, the quasi-Fermi-energy splitting (marked by a dark green bar) equals V_{mpp} = 535 mV which is typical for a *BackPEDOT* solar cell. The 'x-axis' is not to scale.

Figure 50 (b) shows a band diagram at MPP with an introduced W_A reduction of the PEDOT:PSS of 150 mV as observed by our Kelvin-probe measurements. Figure 50 (b) shows the resulting band bending (marked by a red bar) at the PEDOT:PSS/c-Si interface. The band bending creates a barrier for the hole transport from c-Si into the PEDOT:PSS.

This unfavorable band diagram change as a function of storage time in ambient air is a clear indication towards a deeper understanding of the increased series resistance after the degradation. One weakness of our work function theory is the time scale. We observe an abrupt saturation of the W_A difference after ~ 20 h, while the *FF* degradation of our *BackPEDOT* solar cells occurs on the time scale of a few weeks. This discrepancy might be due to the fact that in our *BackPEDOT* solar cells the PEDOT:PSS is covered by a metal layer preventing the water molecules to rapidly interact with the PEDOT:PSS. Further investigations are necessary to develop a complete understanding of the degradation mechanisms and industrially feasible encapsulation techniques.

5.4 Chapter summary

We have observed a pronounced degradation of our PEDOT:PSS/c-Si heterojunction solar cells. Storage was performed in air at approximately 23°C and 65% relative humidity. We observed efficiency degradation behavior for *FrontPEDOT* and *BackPEDOT* solar cells. The relative efficiency degradation could be described by a simple exponential decay with characteristic degradation time constant t_{deg} of (28 ± 1.6) days. The illuminated *J-V* curves showed an '*S*-shape' curve form with increasing time in air, indicating a barrier formation for the carrier transport. By storing the solar cells in a humidity-reduced environment (in a desiccator) t_{deg} was drastically increased to 1615 days, suggesting that humidity in the major cause of degradation. We have encapsulated a *FrontPEDOT* solar cell by a 30 nm thick ALD-Al_2O_3 layer increasing the t_{deg} to 203 days in ambient air. We have proposed a novel encapsulating method for *BackPEDOT* solar cells implementing a metal foil to the cell rear, leading to an improved stability. Based on TEM images of the PEDOT:PSS/c-Si interface we were not be able to detect a SiO_x layer which would explain the degradation. However, using the Kelvin-probe technique we measured a decreasing work function of the PEDOT:PSS as a function of time in air. After 26 hours in air the work function difference reaches a value of + (119 – 150) mV compared to the initial state, which we attributed to a decrease in the PEDOT:PSS work function. We presented a model, where a decreasing work function of the PEDOT:PSS with time in air alters the band configuration, forming a barrier for the hole transport from the silicon into the PEDOT:PSS. With our investigations of the fundamental cause of the degradation and with our approaches towards effective encapsulation method, we made an important step towards the development of fully long-term stable *BackPEDOT* solar cells.

6 Efficiency potential of multicrystalline silicon wafers

Today, block-cast multicrystalline silicon (mc-Si) is the most common material with a market share of 65% of the total solar cell production in 2015 [24]. The benefits of using mc-Si are lower production costs, full-square format, and lower oxygen content compared to Czochralski-grown monocrystalline silicon. However, the electronic quality of the mc-Si bulk material frequently is limited by crystallographic defects decorated with metallic impurities [92], [93], [94], [95]. In this Chapter, we determine the efficiency potential of mc-Si solar cells grown in (non-industrial) highest-purity crucibles with purified coatings [96]. To minimize the impact of crystallographic defects, we select wafer areas with very high lifetimes and accordingly reduced defect concentrations. We fabricate solar cells on non-industrial mc-Si, industrial mc-Si, and FZ-Si wafers and compare the results with SENTAURUS device simulations.

6.1 Block casting of multicrystalline silicon

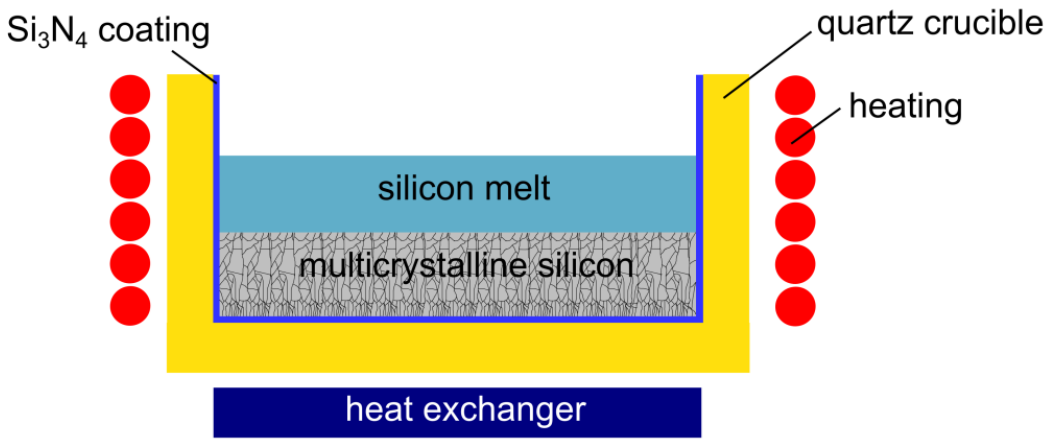

Figure 51: Schematic of a silicon casting setup with directional solidification.

Figure 51 shows a schematic of a silicon casting setup with directional solidification [97]. First, the quartz-crucible is spray-coated with silicon nitride powder (Si_3N_4). After a thermal treatment a crystalline Si_3N_4 layer is formed, which prevents a direct contact of the silicon melt with the quartz-crucible. Next, polycrystalline silicon chunks and boron – the doping material – are filled into the crucible. The polycrystalline silicon is melted and then directionally solidified. The solidification starts at the bottom initialized and supported by a heat exchanger at the bottom of the crucible. After crystallization, the quartz-crucible is detached. The casted silicon crystal is called ingot. The casted multicrystalline ingot is sliced into N rectangular blocks. Each block has a volume of $(15.6 \times 15.6 \times Z)$ cm³, where Z is the height of a block. The square root $\sqrt{N}$ defines the generation (G) of an ingot, which achieved dimensions of up to G7 in the year 2015 [98]. Such casted ingots have masses of up to 1000 kg. Each block is sliced into $(15.6 \times 15.6 \times 0.018)$ cm³ wafers using a wire saw.

To increase the quality of mc-Si material, the defect concentration and the level of metal contamination in the bulk needs to be decreased. Possible sources of contamination may originate from the quartz crucible, the silicon nitride coating, the silicon chunks and boron. The best technical conditions are created to realize the most pure environment for silicon block-casting, to demonstrate the high-quality potential of mc-Si material. However, no effort was made towards the reduction of the crystallographic defect concentration. To minimize the impact of crystallographic defects, we select wafer areas of very high lifetimes and accordingly reduced defect concentrations for solar cell fabrication.

Our high-quality mc-Si wafers were casted in a G1 crucible at the silicon material technology research center (*SiMTEC*) at Fraunhofer ISE in Freiburg, Germany and at the *Leibniz-Institut für Kristallzüchtung* (IKZ) in Berlin, Germany. The crucible walls are made from high-purity quartz glass and are coated with a high-purity silicon nitride (Si_3N_4) double layer in order to reduce the diffusion of impurities into the silicon during the casting process. More details on the crystallization can be found elsewhere [96]. Si_3N_4 powder was supplied from *HC Stark* AG. High-purity polycrystalline silicon feedstock material for casting was supplied by *Wacker Chemie* AG. The commercially available (in this Chapter referred to as 'standard') mc-Si wafers are chosen from the middle block of a G5 crucible. Suppliers were two companies: *GREEN ENERGY TECHNOLOGY* Inc., Taiwan (GET) and *Sino-American Silicon Products* Inc., Taiwan (SAS).

6.2 Impact of phosphorus gettering

Each multicrystalline silicon wafer has a unique spatial carrier lifetime distribution, which is particularly affected by the phosphorus diffusion step. During the phosphorus diffusion, metal impurities agglomerate in the phosphorus-diffused region due to the higher solubility than in the bulk [99]. This 'cleaning' of the silicon bulk is called 'phosphorus gettering' [95], [100].

To demonstrate the effect of phosphorus gettering on our high-purity mc-Si material, we use two neighboring wafers. The wafers were cut into 5×5 cm² samples. Next, both mc-Si wafers were damage-etched and RCA-cleaned. One wafer was phosphorus-diffused at 850°C in a quartz-tube furnace. After phosphorus diffusion the emitter was removed by chemical etching. Then, both wafers were RCA-cleaned and subsequently passivated by ALD-Al_2O_3. The lifetime of both wafers was measured by an infrared lifetime mapping (ILM) [20] at an illumination intensity of 0.27 suns.

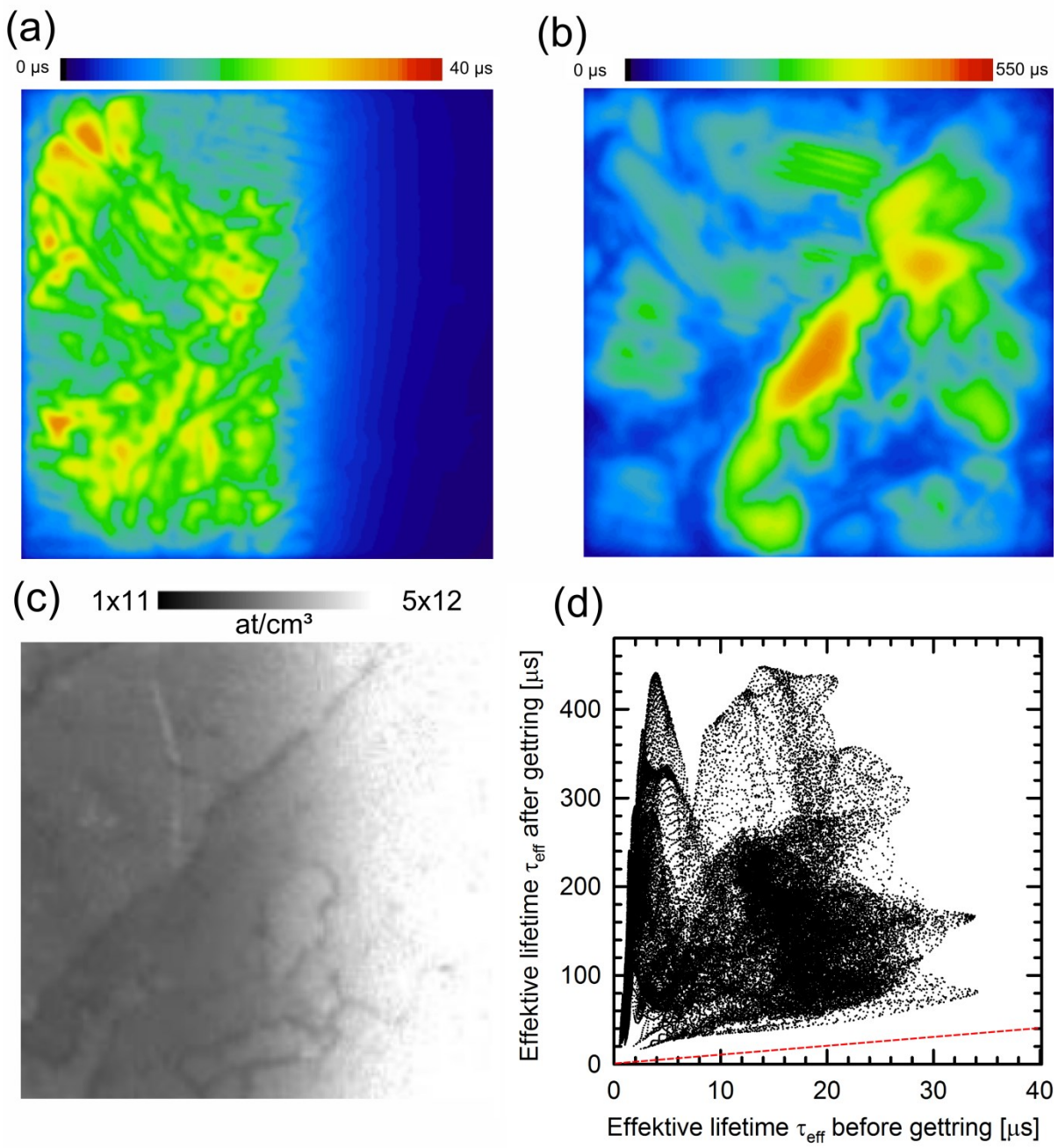

Figure 52: Infrared lifetime mapping (ILM) of a passivated mc-Si wafer (a) before and (b) after phosphorus gettering, (c) interstitial iron concentration measured using the PC-PLI method [101], (d) effective lifetime after the phosphorus gettering as function of the effective lifetime before phosphorus gettering. Effective lifetime values which do not change during the phosphorus gettering are shown as a dashed red line.

Figure 52 shows spatially resolved effective lifetime images of a passivated mc-Si wafer (a) without and (b) with phosphorus gettering. Please note the scale which ranges from 0 µs to 40 µs and 0 µs to 550 µs for the wafers before and after phosphorus gettering, respectively. We observe that the effective lifetime increases by one order of magnitude after the phosphorus gettering. One characteristic is the lower lifetime region at the right edge of the mc-Si sample before phosphorus gettering. This region – the so-called 'red zone' – is contaminated with interstitial iron (Fe_i) from the crucible wall . Figure 52 (c) shows the Fe_i concentration measured with the PC-PLI method [101] without phosphorus gettering. As can be observed in Figure 52 (b), the Fe_i contamination is successfully reduced in the 'red zone' after the phosphorus gettering.

Figure 52 (d) shows a plot of the effective lifetime after phosphorus gettering as a function of the effective lifetime before phosphorus gettering. Each point corresponds to one pixel-pair of the Figure 52 (a) and (b). Effective lifetime values which do not change in phosphorus gettering are shown as a dashed red line in Figure 52 (d). We observe that the spatially distributed effective lifetime increases for each pixel after the phosphorus gettering. However, no correlation between the effective lifetime before and after phosphorus gettering can be observed. Therefore, the selection of the best suited area for our solar cell process has to be performed on the phosphorus gettered mc-Si wafers.

We select a 1 × 1 cm² region out of a 15.6 × 15.6 cm² mc-Si wafer for our solar cells process. Criteria for the selected region are (i) a high local effective lifetime of a phosphorus gettered mc-Si wafer and (ii) a (100) crystal orientation to allow implementation of a random-pyramid texture.

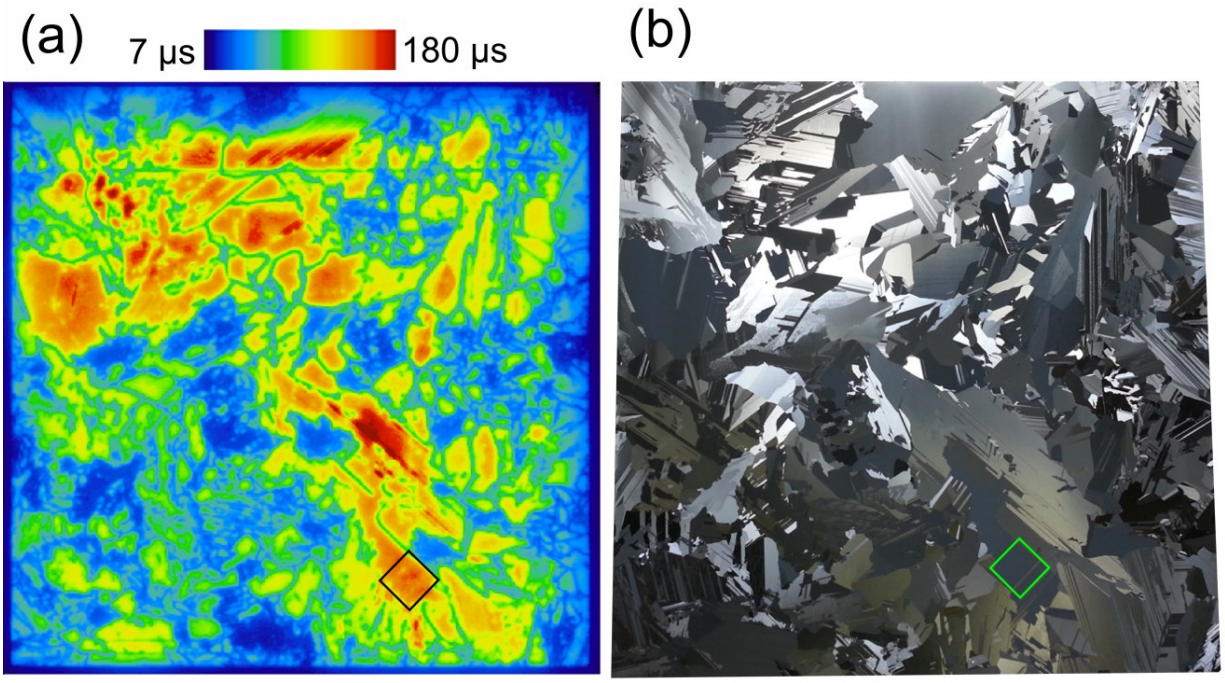

Figure 53: (a) Photoconductance-calibrated photoluminescence lifetime image (PC-PLI) of a 156 × 156 mm² phosphorus-gettered and ALD-Al_2O_3-passivated mc-Si wafer. (b) Photograph of a random-pyramid-textured wafer. Wafers shown in (a) and (b) are neighbours. A suitable region for high-efficiency solar cell processing is marked by (a) a black square and (b) a green square.

The most important criteria for selecting the area is the high local lifetime after phosphorus gettering. First, we apply a phosphorus diffusion to the complete 15.6 × 15.6 cm² mc-Si wafer. Next, the phosphorus-doped silicon region is removed by chemical etching. After RCA cleaning the wafer surface is passivated by atomic-layer-deposited Al_2O_3. Afterwards, we perform photoconductance-calibrated photoluminescence lifetime imaging (PC-PLI) measurements [23] to identify the best suitable areas for our high-efficiency solar cell process. Figure 53 (a) shows the phosphorus-gettered and ALD-Al_2O_3-passivated mc-Si wafer. One suitable region for a high-efficiency solar cell with an area of 1 × 1 cm² is marked by a black square.

The second selection criterium is to find an area with (100) crystal orientation. Therefore, we apply KOH/2-propanol etching to the entire mc-Si wafer. Using light microscopy we determine wafer areas where upright random pyramids (RPs) are formed. Figure 53 (b) shows a photograph of an RP-textured wafer. One suitable region for a high-efficiency solar cell with an area of 1 × 1 cm² is marked as a green square.

Wafers shown in Figure 53 (a) and (b) are neighbours. By overlapping both images we determine areas which fulfill both criteria. For the solar cell processing, we cut out the best-suited areas using a laser.

6.3 Fabrication of multicrystalline silicon solar cells

In the following Section, we apply our lab-type PERC process to FZ-Si, high-quality mc-Si and industrial type mc-Si wafers. We compare our solar cell results with SENTAURUS device simulations.

Figure 54 shows a schematic of our lab-type PERC solar cell. In the following, we briefly describe the PERC process applied in this study. We use 15.6 × 15.6 cm² mc-Si wafers with a thickness of 200 µm and a resistivities (ρ) of 1 Ωcm, 1.7 Ωcm and 2 Ωcm. For reference cells, we use 6'' FZ-Si wafers with a thickness of 300 µm and a ρ of 0.5 Ωcm and 1.5 Ωcm. First, the mc-Si wafers are damage-etched and the FZ wafers are thinned in a $C_2H_4O_2/HNO_3/HF$ (chemical polishing) solution. FZ wafers are thinned to a thickness of ~180 µm which is comparable to those of the mc-Si wafers. The final wafer thickness is ~180 µm. Two FZ silicon samples are processed without chemical polishing and have a thickness of 300 µm. These samples are processed as reference solar cells. After RCA cleaning, both surfaces of the wafers are protected by a 100 nm thick SiN_x layer deposited by plasma-enhanced chemical vapor deposition (PECVD). Then, a 1 × 1 cm² or a 2 × 2 cm² (only reference solar cells) window is opened on the front side by picosecond laser ablation of the silicon nitride. Subsequently, the silicon surface within the ablated windows is random-pyramid-textured in a KOH/2-propanol solution. After texturing, the samples are phosphorus-diffused in a quartz-tube furnace at 850°C. The resulting n^+-emitter has a sheet resistance of (89 ± 9) Ω/□. After the phosphorus glass and the SiN_x protecting layers are removing in a 5% HF-diluted solution, the rear surface is passivated by an atomic-layer-deposited Al_2O_3 / PECVD-SiN_x stack [33]. The Al_2O_3 / SiN_x stack is structured by laser contact opening (LCO) and the entire rear surface is metallized by electron beam evaporation of aluminum. Subsequently, after the deposition of an 0.24 nm thick AlO_x tunneling layer on the n^+-emitter [39], an Al front grid is electron beam evaporated through a nickel-shadow mask. After evaporation, a short ~8 sec dip in a 70°C Al-etching bath removes residual aluminum. Finally, the entire front surface is coated with a 10 nm SiN_x passivating layer (refractive index of $n = 2.4$) and a 75 nm SiN_x anti-reflection coating (refractive index of $n = 1.9$). Note that our solar cell process does not include a hydrogen passivation step [102], [103], which might be capable of further improving the bulk quality of the mc-Si materials.

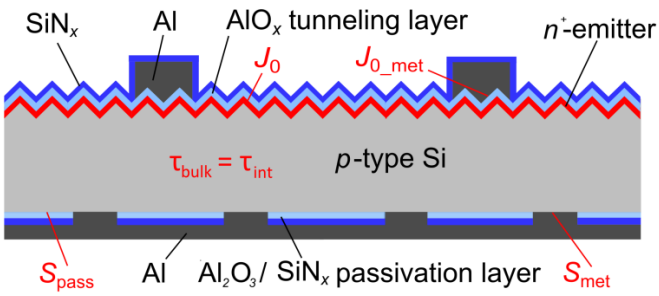

Figure 54: Schematic of our lab-type PERC solar cell. Simulation parameters are labeled red.

A three-dimensional device simulation is performed using SENTAURUS Device. The simulated solar cell parameters mark the upper limit, which can be achieved with our solar cell geometry when the effective lifetime in the bulk is only limited by the intrinsic recombination. As input parameters we use a wafer thickness of 180 µm. The intrinsic effective lifetime (τ_{int}) is calculated using the

parameterization of Richter et al. [12], resulting in a τ_{int} value of 1.3 ms for a resistivity $\rho = 0.5$ Ωcm, $\tau_{int} = 5$ ms for $\rho = 1.0$ Ωcm, $\tau_{int} = 10.3$ ms for $\rho = 1.5$ Ωcm, $\tau_{int} = 12.8$ ms for $\rho = 1.7$ Ωcm, and $\tau_{int} = 16.7$ ms for $\rho = 2.0$ Ωcm. The rear surface metallization fraction is 5%. The contact resistance between aluminum and emitter is assumed to be 2 mΩcm^2, and between base and aluminum is assumed to be 3 mΩcm² [104]. The emitter saturation current density J_0 of 124 fA/cm² on the SiN_x-passivated emitter was estimated from measurements on test samples using the Kane and Swanson method [15]. For the metallized area fraction of the emitter, we assume $J_{0_met} = 1054$ fA/cm² [46]. The rear surface recombination velocity is assumed to be $S_{pass} = 4.8$ cm/s on the passivated rear surface and $S_{met} = 2\times10^4$ cm/s in the metallized fraction of the rear surface [104]. The different recombination parameters taken into account for our SENTAURUS Device simulations are labeled red in Figure 54. Table 6 shows the results of the simulated solar cell parameters.

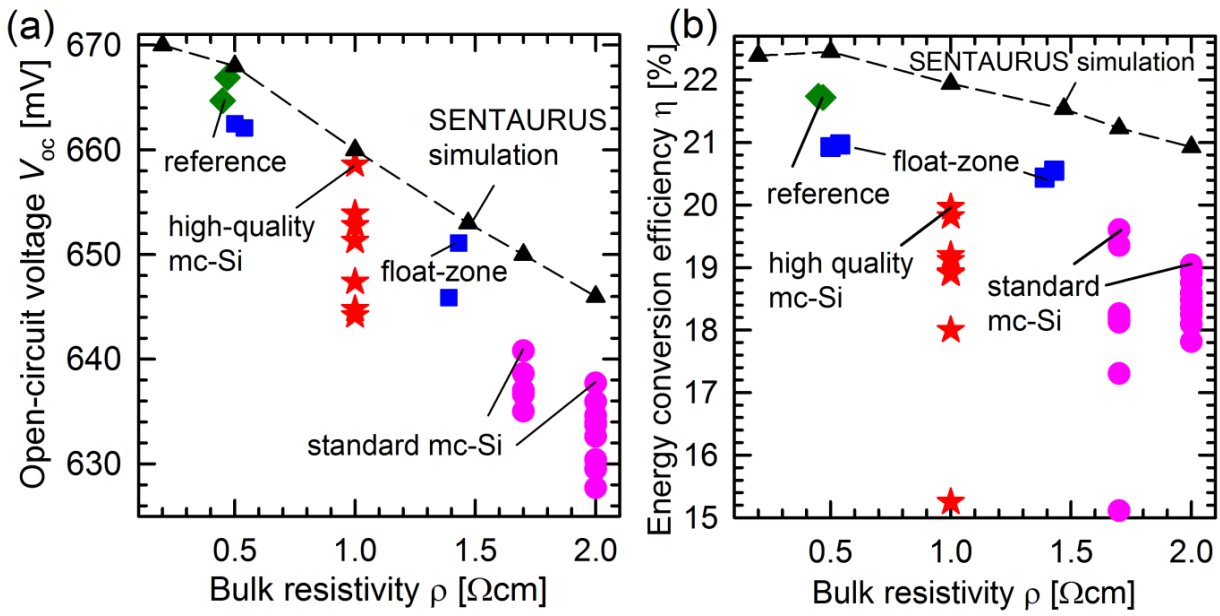

Figure 55: (a) Open-circuit voltages V_{oc}, and (b) energy conversion efficiencies η of FZ-Si solar cells with (blue squares) and without (green diamonds) chemically polished silicon surface, and mc-Si solar cells fabricated on commercially available mc-Si (pink circles) and casted in high-purity crucible mc-Si (red stars), and SENTAURUS device simulations (black triangles) as a function of bulk resistivity ρ.

Table 6: Measured and simulated PERC solar cell parameters. Solar cells with the highest measured V_{oc} among each group are shown. The bulk lifetime of the simulated solar cells is Auger-limited.

Material	ρ [Ωcm]	W [µm]	Area [cm²]	V_{oc} [mV]	J_{sc} [mA/cm²]	FF [%]	η [%]
FZ-Si	0.5	300	1	667	40.6	80.2	21.7
FZ-Si	0.5	187	1	663	39.4	80.2	20.9
simulated	0.5	180	-	668	41.4	81.2	22.5
FZ-Si	1.5	195	1	651	40.0	78.8	20.6
simulated	1.5	180	-	653	41.5	79.5	21.5
mc-Si, purified	1.0	167	4	**659**	37.6	77.1	19.1
mc-Si, purified	1.0	172	1	647	39.5	78.0	**20.0**
simulated	1.0	180	-	660	41.4	80.2	21.9
mc-Si, industrial	1.7	160	1	641	39.2	78.1	19.6
simulated	1.7	180	-	650	41.48	78.7	21.2
mc-Si, industrial	2.0	169	4	638	37.6	78.2	18.8
simulated	2.0	180	-	646	41.52	78.0	20.9

Table 6 shows measured and simulated PERC solar cell *J-V* parameters. Figure 55 (a) shows the measured open-circuit voltages (V_{oc}) of our PERC solar cells with an aperture area of 1 × 1 cm² and 2 × 2 cm², respectively, as a function of the bulk resistivity for the different materials investigated in this work. The reference solar cells made on 0.5 Ωcm FZ silicon with a thickness of 300 µm show the highest V_{oc} values of up to 667 mV (green diamonds). The experimentally achieved highest V_{oc} is 5 mV below the simulated V_{oc} value (black triangles). On the same FZ material, however with a chemically polished surface, we achieve V_{oc} values of 662 mV and 663 mV (blue squares). We attribute the lower V_{oc} values - compared to the reference solar cells - to a surface modification of the silicon surface during chemical polishing. For the 1.5 Ωcm FZ silicon the experimental V_{oc} values are 646 mV and 651 mV.

For the standard industrial mc-Si material (pink circles) we achieve relatively low V_{oc} values of 635 mV - 641 mV on the 1.7 Ωcm material and 628 mV - 638 mV on the 2.0 Ωcm material, respectively. Due to the reduced bulk quality, the experimental V_{oc} values of standard mc-Si are between 8 and 18 mV below the SENTAURUS-calculated V_{oc} values for the Auger-limited bulk lifetime.

For the high-quality 1.0 Ωcm mc-Si material (red stars), a high maximum V_{oc} of 659 mV is achieved. To our knowledge, this was the highest V_{oc} value of any mc-Si solar cell reported at that time of publication [106] for a ≥2 × 2 cm² mc-Si solar cell. More important, the highest V_{oc} value of the high-quality mc-Si is only 1 mV below the calculated V_{oc} value for the Auger-limited case. Based on these finding, we conclude that the bulk quality of the best high-quality mc-Si areas are in fact comparable to the best possible monocrystalline silicon material.

Please note that the highest V_{oc} of 638 mV for standard mc-Si and 659 mV for high-quality mc-Si, respectively, are achieved on phosphorus-gettered wafers. After the diffusion the n^+-region was removed in a chemical polishing solution. During the solar cell process, the wafers are phosphorus-diffused for the second time to form an n^+-emitter. Phosphorus gettered drastically improves the bulk quality of the mc-Si wafers. On the high-quality mc-Si wafers that are not phosphorus-gettered, we achieve a V_{oc} difference of 6 mV compared the simulated V_{oc} values even for the high-quality mc-Si wafers. On the standard mc-Si wafers that are not phosphorus-gettered we obtain a maximum V_{oc} which is 9 mV below the simulated maximum value.

Figure 55 (b) shows the energy conversion efficiencies η of our lab-type PERC solar cells as a function of the bulk resistivity ρ for the different materials examined in this work. Both FZ reference solar cells achieved an efficiency of 21.7%. On a selected mc-Si area of 1 × 1 cm² we achieve a very high solar cell efficiency of 20.0% [106], which was during the time of publication only slightly below the record value of 20.4% [105]. Compared to the device simulation, all measured solar cell efficiencies are reduced by at least $0.75\%_{abs}$. This deviation is partially attributed to a reduced fill factor due to series resistance losses, as we neglect the series resistance within the front metallization grid in our simulations. Furthermore, we observe a pronounced difference between the efficiencies measured on FZ silicon and mc-Si solar cells. The deviation between FZ silicon and mc-Si is caused mainly by two factors, as depicted in Figure 53: (i) an inhomogeneous distribution of the bulk lifetime, reducing V_{oc} and J_{sc} and (ii) an imperfect random-pyramid texture for the mc-Si samples, which reduces the J_{sc}.

The spatial homogeneity of the effective lifetime examined by PC-PLI and the surface texture of our best mc-Si solar cell with the efficiency of 20% are shown in Figure 56.

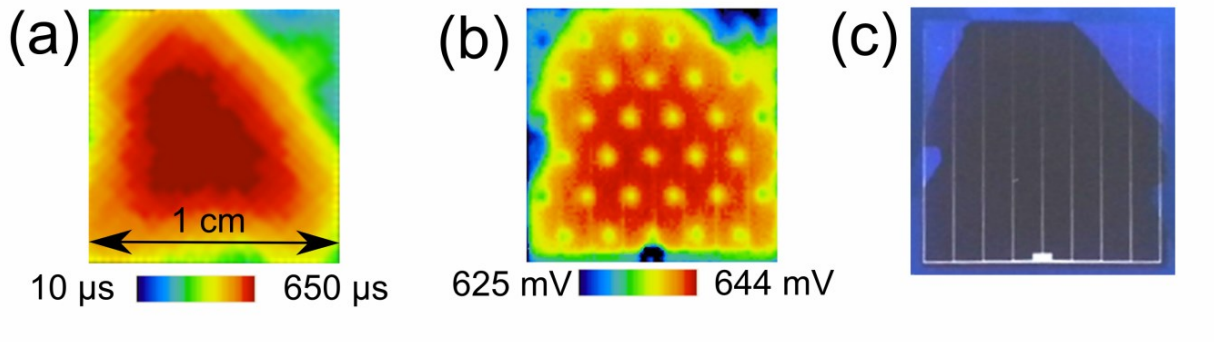

Figure 56: (a) PC-PLI lifetime image of a phosphorus-gettered 1 cm^2 area of an mc-Si wafer. (b) V_{oc} image calculated from an electroluminescence image of the PERC solar cell made on the area shown in (a). (c) Photograph of the mc-Si solar cell. From the photo it can be seen that different crystallites are present in the active cell area.

Figure 56 (a) shows the PC-PLI image of a phosphorus-gettered 1 cm^2 area of an mc-Si wafer. Figure 56 (b) shows the spatially distributed open-circuit voltage that is calculated from an electroluminescence image of the finished solar cell at an applied voltage of 644 mV [the cell was processed on the area shown in Figure 56 (a)]. We find an excellent correlation between the photoluminescence image of the wafer prior to the solar cell processing and the V_{oc} image of the finished solar cell, demonstrating that our pre-selection procedure was successful. Figure 56 (c) shows a photograph of the processed solar cell. The photograph illustrates a variation in the RP texturing at the top left and top right corners, caused by varying crystal orientations.

6.4 Chapter summary

Float-zone silicon, multicrystalline block-cast silicon from an industrial supplier and mc-Si from a laboratory-scale high-purity crucible were compared on solar cell level. On the multicrystalline material from the high-purity crucible, we achieved V_{oc} values of up to 659 mV, which was a record-high value at that time of publication [106]. The open-circuit voltage of our best multicrystalline silicon solar cell is only 1 mV lower compared to SENTAURUS Device simulations, where the bulk lifetime is only limited by Auger recombination. For commercially available standard multicrystalline silicon material, however, the highest measured open-circuit voltages are 8 – 9 mV lower compared to the simulations. Accordingly, the efficiency of today's multicrystalline silicon solar cells is predominantly limited by regions of high defect and impurity concentrations. Our cell results based on multicrystalline silicon material casted in high-purity crucibles show that the reduced bulk quality commonly observed in standard multicrystalline silicon material is largely avoidable using a high-purity crucible during casting and by extending the area of monocrystallinity. On a selected area of 1×1 cm², we achieved a solar cell efficiency of 20% on the high-purity mc-Si material.

7 Laser-texturing of multicrystalline silicon

Texturing of the silicon wafer surface is performed to reduce the front reflection and increase the light absorption within the silicon wafer via light trapping. State-of-the-art industrial texturing is realized by anisotropic etching of the (100) oriented silicon surface in a KOH/2-propanol alkaline solution. Unfortunately – as shown in the previous Chapter – this texture is only applicable to a fraction of a multicrystalline silicon (mc-Si) wafer surface with predominant (100) crystalline orientation. In this Chapter, we hence develop a novel texturing method suitable for mc-Si solar cells.

7.1 Random-pyramid texturing

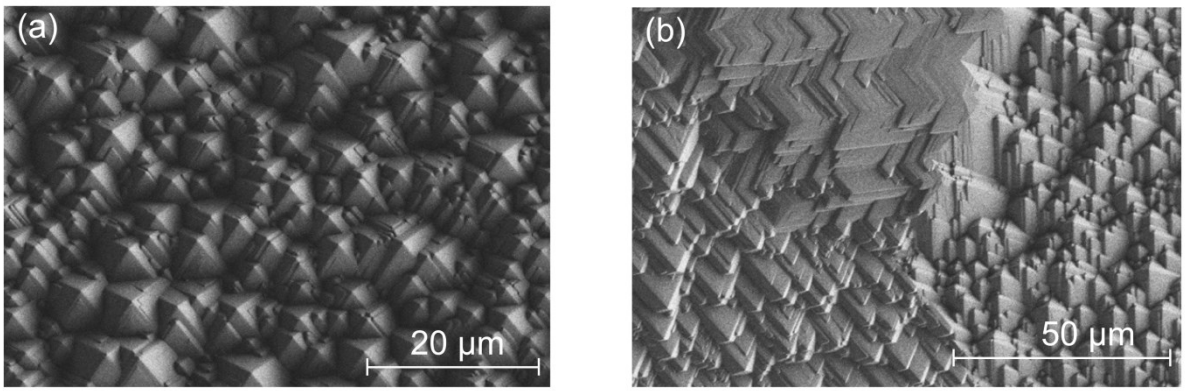

Figure 57: Plan view of an SEM image of a random-pyramid-textured (a) monocrystalline silicon and (b) multicrystalline silicon. Due to the varying crystal orientation of the mc-Si surface random pyramids are of different sizes and tilted.

The standard texturing process in the production of monocrystalline silicon solar cells is alkaline texturing also referred to as random-pyramid texturing. The alkaline solution is based on potassium (K) or sodium (Na) hydroxide and 2-propanol as a wetting agent. The fundamental mechanism behind the alkaline texturing process is the different etching rate in different crystal orientations. The (100)-oriented silicon surface has a 35× larger etching rate in alkaline texturing solutions based on KOH compared to the (111)-oriented silicon surface [107]. During alkaline texturing randomly sized pyramids with a facet angle of 54.74° are formed on the silicon surface, which is the angle between the (100) and the (111) crystal planes. Figure 57 (a) shows a scanning electron microscopy (SEM) image of a plan view of a random-pyramid-textured silicon surface. In contrast, multicrystalline silicon (mc-Si) typically consists of randomly oriented grains with grain sizes up to a few square centimeters. Alkaline texturing of a surface with an orientation other than (100) results in tilted pyramids and less optimal optical properties than upright pyramids. Figure 57 (b) shows a plan view of an SEM image of a mc-Si surface with three grains with orientations other than (100). This is the reason why the texturing of mc-Si wafers requires an alternative technique.

7.2 The honeycomb texture

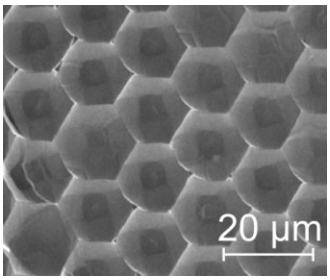

Figure 58: SEM image of a *honeycomb* texture of silicon.

An ideal isotropic texturing process forms hemispherically shaped tubs within the silicon surface. The smallest fraction of untextured silicon is achieved by a hexagonal arrangement of the tubs, resulting in the so-called *honeycomb* texture [108]. Figure 58 shows an SEM image of a honeycomb-textured silicon surface. Various techniques have been reported in the literature to fabricate honeycomb textures in silicon using: lithography [108], [109], [110], masked reactive ion etching [111], [105], ink-jet masking [112], nanoimprint lithography [113], [114], masked laser texturing [115], [116], [117], and direct laser texturing [115], [118], [119].

Laser techniques have the advantage of non-contact processing and are already well established in a couple of industrial solar cell processes, such as edge isolation, selective emitter formation and dielectric layer ablation. Laser texturing of silicon solar cells was first demonstrated by Zolper et al. in 1989 [120]. More recently, the applicability of laser texturing to high-efficiency solar cell processes was studied [116], [118], [121]. While energy conversion efficiencies of up to 19.3% were achieved on mc-Si using masked laser texturing [121], there is still a necessity to demonstrate the high efficiency potential of the simpler (and therefore more industrially relevant) direct laser texturing (*DiLaT*) on mc-Si material. Another important advantage of *DiLaT* over masked laser texturing is the absence of two additional process steps for the deposition and removal of a masking dielectric layer on the silicon surface.

7.3 Direct laser texturing (*DiLaT*)

In this Section, we develop and implement *DiLaT* into lab-type small-area (2 × 2 cm²) PERC cells on mono- and multicrystalline silicon wafers. We compare the solar cell results obtained on both materials with planar, alkaline textured and *DiLaT* surfaces.

7.3.1 Direct laser texturing process

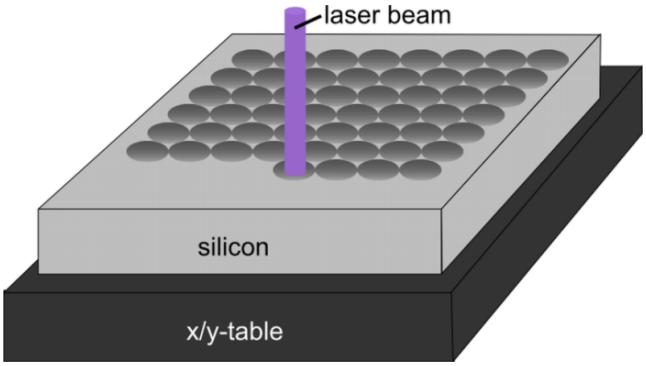

Figure 59: Schematic of our *DiLaT* process.

In our *DiLaT* process we use a frequency-converted q-switched Nd:YVO_4 laser (*AviaX*, *Coherent* Inc.). All relevant laser parameters of our *DiLaT* process are summarized in Table 7.

Table 7: Laser parameters as used for *DiLaT* texturing in this work.

Wavelength	355 nm
Repetition rate	50 kHz
Pulse duration	30 ns
Pulse energy	6 µJ/shot
Pitch *p*	7 µm
Laser mode	'on the fly'
Spot positioning	X/Y-Table
Beam shape	Gaussian
M^2 factor	1.3

The aspect ratio is defined as the structure depth-to-diameter ratio. Higher aspect ratios will generally be favorable for a reduced reflection. The depth of the structures (tubs) should be kept smaller than the metallization layer thickness (in this work 20 µm) to avoid additional resistance losses. To achieve a low structure depth and high aspect ratio at the same time, the diameter of the tubs has to be as small as possible. With the optical setup used in this work we achieve a minimum laser diameter of ~7 µm. At a laser pulse energy of 6 µJ we obtain tubs with a diameter of $d \sim 7$ µm (measured with a *Leica* 328 optical microscope, *Leica Microsystems* GmbH) at an estimated structure depth of 4 µm [122]. In order to reduce overlapping, we choose a pitch of $p = 7$ µm between the neighboring spots. To further enhance the aspect ratio and therefore the light trapping, we create deeper structures by applying up to four laser pulses at the same position on the same sample. The positioning of the laser spots is

achieved in the 'on the fly' mode by moving the sample on an X/Y-table, as schematically shown in Figure 59. 'on the fly' mode is defined by a continuous moving of the sample relative to the laser beam. The distance between two laser shots is defined by the repetition rate of the laser and the relative velocity. Subsequently, to apply more laser shots on the same position, the laser process has to be repeated. Another mode is the 'burst' mode where the desired amount of laser shots is applied sequently on the same position. The advantage of the 'on the fly' mode is a shorter process time compared to the 'burst' mode which is on the other side more accurate. Even with the 'on the fly' mode, the positioning of the wafer using an X/Y-table has the disadvantage of being a very slow process, which is not compatible with the required high throughput in an industrial solar cell production line. The *DiLaT* process as described above takes about 10 minutes for texturing an area of one square centimeter. It is possible, however, to speed up the process by several orders of magnitude using a beam splitting system and applying diffractive optical elements. We expect the main challenge in combining available high-energy and high-beam-repetition laser systems with a suitable diffractive optics. Such a system would be conceivable in an industrial solar cell production process.

7.3.2 Laser damage removal by wet chemical treatment

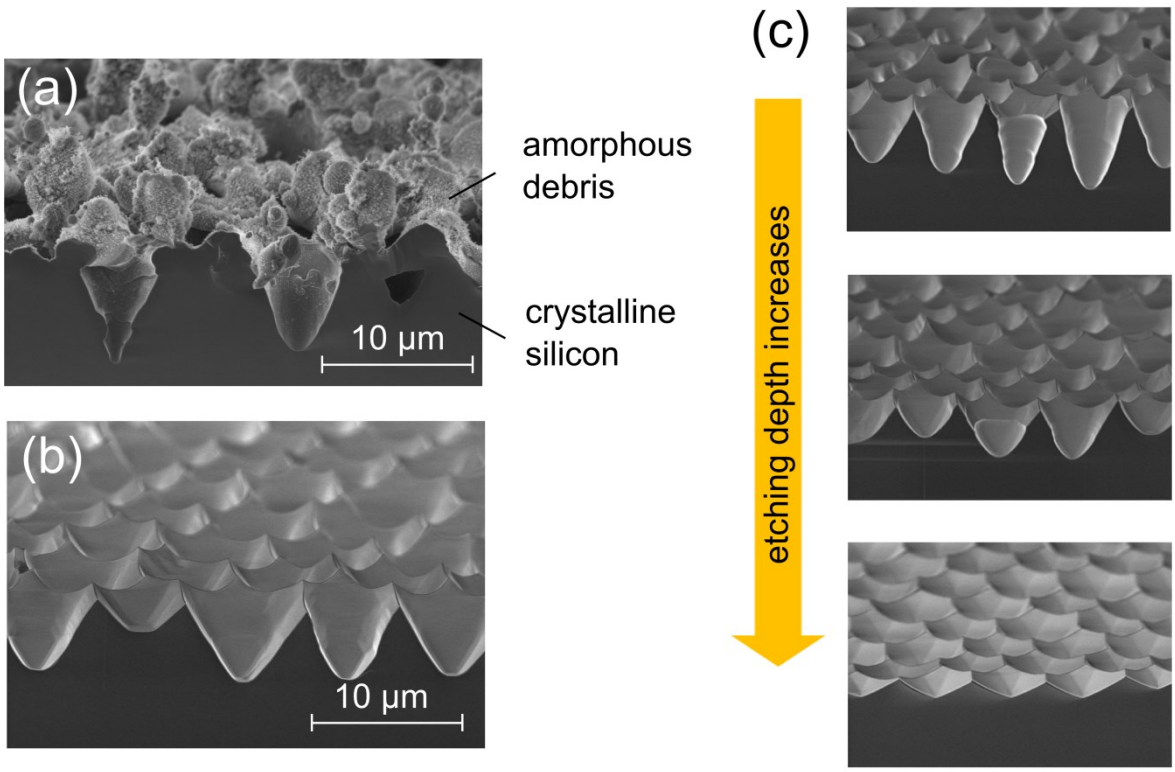

Figure 60: SEM images of a direct-laser-textured silicon surface (a) before and (b) after wet chemical etching. The effect of an increased etching depth on the *DiLaT*-textured silicon surface is shown in (c).

To remove the debris and the laser-damaged silicon region after laser texturing we have developed a two-step wet chemical etching process [123]. In the first step, we remove the amorphous debris by etching the sample in a 25%$_{wt}$ NaOH alkaline solution at a temperature of 40°C for 3 mins. In the second step, we remove the laser-damaged silicon region by etching the sample in a 40%$_{vol}$ HF : 100%$_{vol}$ HNO_3 (1 : 30) acidic solution. We measure the weight difference before and after the

etching to determine the average etching depth as a parameter for the amount of removed silicon. The etching depth is a more accurate parameter than etching time, since silicon reacts with HF/HNO_3 solution exothermally [124] and no active cooling is available in our experimental setup. Consequently, the exact etching depth cannot be determined before the complete etching process is finished. The term 'etching depth' may cause irritation since it may be thought as a measure for the depth of the tubs. Etch depth is however, referred to the removal of a planar surface. As shown in Figure 60 (c), an increasing depth flattens the surface texture. Therefore, there is a tread-off to be determined between removal of the laser-induced damage and the texturing profile.

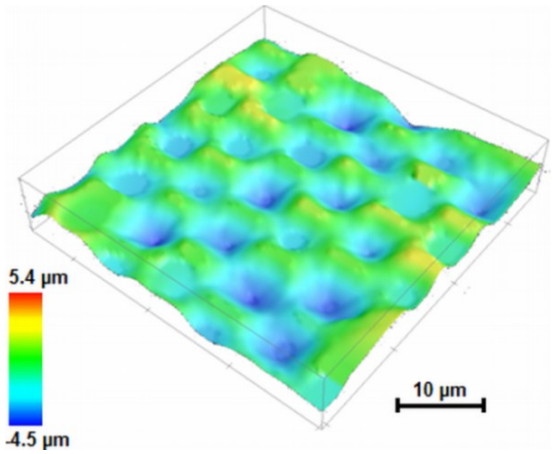

Figure 61: Confocal microscopy image of a direct-laser-textured silicon surface.

Next, we characterize the structure of our *DiLaT*-textured silicon surface. Figure 61 shows a confocal microscopy (*Leica DCM3D*, *Leica Microsystems* GmbH) image of a *DiLaT* mc-Si surface after the two-step chemical etching, showing the *honeycomb* pattern of the tubs. The confocal microscopy image confirms that the depth of the tubs is below 10 µm.

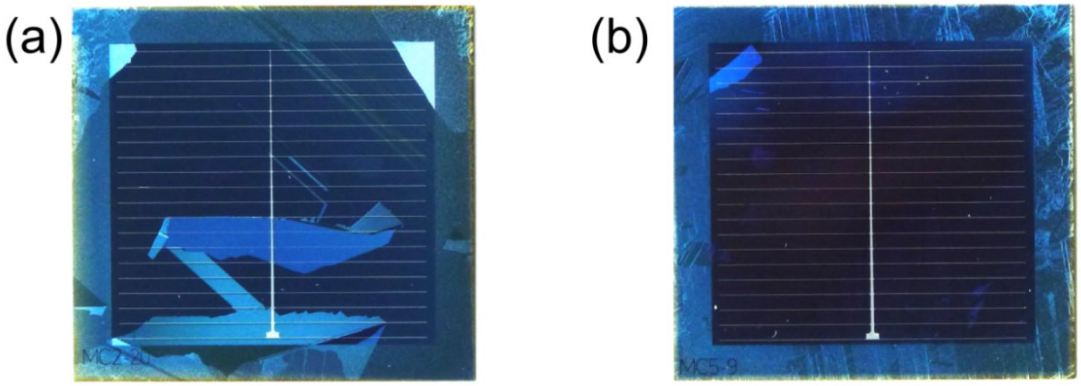

Figure 62: Photograph of (a) alkaline textured and (b) *DiLaT* mc-Si PERC solar cells. The size of the aperture cell area is 2×2 cm^2 while the total size of the cell is 2.5×2.5 cm². Please note that the inactive edge is not diffused and not textured.

Figure 62 shows photographs of two mc-Si PERC solar cells with (a) an alkaline textured surface in a KOH/2-propanol solution at 80°C and (b) a *DiLaT* surface. We have selected an mc-Si wafer area with different but few grains to achieve an optimal result of the alkaline texturing. The *DiLaT* cell shown in Figure 62 (b) contains a larger number of crystallites of various orientations. Despite the latter, the surface of the *DiLaT* mc-Si cell appears more homogeneous compared to the cell with the alkaline textured surface, highlighting the isotropic nature of our *DiLaT* process. Reflectance and quantum efficiency measurements of these solar cells will be discussed in the next Section.

7.4 Application of direct laser texturing to solar cells

We apply our newly developed *DiLaT* texture to our lab-type PERC solar cells on multicrystalline and monocrystalline silicon wafers. As references we fabricate PERC solar cells with random-pyramid-textured and planar surfaces. We compare the solar cell results based on illuminated current-voltage characteristics and compare internal quantum efficiencies of our best random-pyramid-textured and *DiLaT*-textured solar cells.

7.4.1 Solar cell structure and processing sequence

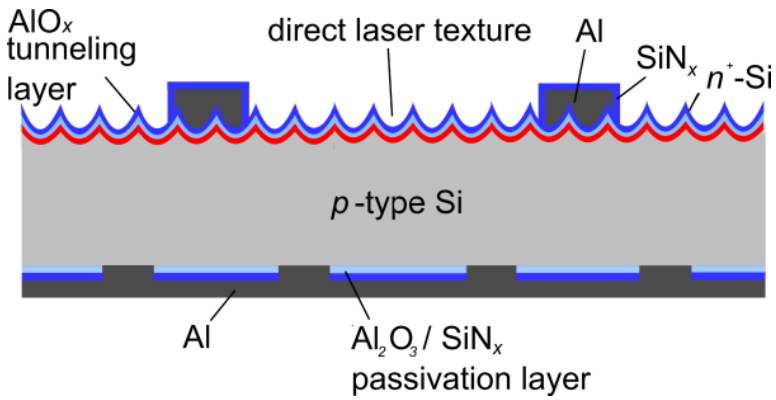

Figure 63: PERC solar cell with *DiLaT* front surface as processed in this study.

A schematic of the passivated emitter and rear cell (PERC) with *DiLaT* front surface is depicted in Figure 63. As substrate materials we use 0.5 Ωcm *p*-type boron-doped float-zone silicon (FZ-Si) as well as 1.3 Ωcm and 1.8 Ωcm *p*-type boron-doped block-casted multicrystalline silicon (mc-Si). The mc-Si samples originate from different, non-neighboring positions of wafers and have therefore different grain distributions. For the mc-Si wafers we start with a *Puraton* cleaning, then perform an isotropic damage etching and subsequently an RCA cleaning. For the FZ-Si wafers we only perform an RCA cleaning, as the delivered wafers had already been damage-etched. Next, a 110 nm thick silicon nitride (SiN_x) (refractive index $n = 1.9$ at $\lambda = 632$ nm) diffusion barrier is deposited on both sides of the wafers by microwave-remote plasma-enhanced chemical vapor deposition (PECVD, *Oxford Instruments*, *Plasmalab 80+*). We then define a 2 × 2 cm² diffusion window with a frequency-doubled Nd:YVO_4 laser ($\lambda = 532$ nm, pulse duration 9 ps, *SuperRapid*, *Coherent* Inc.). The diffusion window is a part of our small-area lab PERC process and is not required for the *DiLaT* process in general. At this step, we split the cell batch into three different groups. One group does not receive any texture, the second group receives an alkaline texture, and the third group is *DiLaT*-textured. The texturing is performed within the laser-opened diffusion windows only. For random-pyramid texturing we use a KOH/2-propanol solution at 80°C, which is our standard process for random-pyramid texturing of (100)-oriented silicon wafers. For *DiLaT* we apply three laser pulses at the each wafer position and etch the samples in the two-step process, as described above, to remove the debris and the laser-damaged silicon. We vary the etching depth in order to optimize the *DiLaT* process. After RCA cleaning, phosphorus is diffused into the textured regions at 850°C from a $POCl_3$ source in a quartz-tube furnace, resulting in an n^+-emitter with a sheet resistance in the range between 80 Ω/□ and 120 Ω/□. After diffusion the phosphorus silicate glass and the SiN_x diffusion barrier are removed in a $40\%_{wt}$ HF solution. For the rear surface passivation we use a 30 nm thick Al_2O_3/100 nm thick SiN_x stack [33]. The Al_2O_3 layer is deposited at 200°C by plasma-assisted atomic layer deposition (*FlexAL*,

Oxford Instruments), followed by an annealing step in a quartz-tube furnace at 425°C for 15 minutes in a nitrogen atmosphere. The Al_2O_3 layer is coated with a 100 nm thick SiN_x layer ($n = 2.05$ at $\lambda = 632$ nm) deposited by microwave-remote PECVD in an Oxford Instruments Plasmalab 80+ reactor at 400°C. Subsequently, we define contacts in the Al_2O_3/SiN_x stack by laser contact opening (LCO) using a Lumera laser (*Coherent* Inc.). The optimum opening geometry depends on the bulk resistivity ρ and the wafer thickness W. We calculate the optimum geometry using an analytical model [125]. For material with $\rho = 0.5$ Ωcm and $W = 275$ µm we use a rectangular pattern of square pads with a pitch p of 2.2 mm and a total area coverage fraction f of 4%. For material with $\rho = 1.3$ Ωcm and $W = 130 – 140$ µm we use a rectangular pattern of square pads with $p = 1.9$ mm and $f = 5.4\%$. For material with $\rho = 1.8$ Ωcm and $W = 170 – 180$ µm we use $p = 1.2$ mm and $f = 13.7$ %. After contact opening, 10 µm aluminum is evaporated by electron-beam evaporation (*BAK 600*, *Oerlikon Balzers* AG) onto the entire rear. Next, we deposit an AlO_x tunneling layer on the top of the n^+-emitter [38] in an *FlexAL* (*Oxford Instruments*) reactor. We then evaporate a 20 µm thick aluminum grid through a shadow mask on top of the AlO_x layer using electron-beam evaporation (*BAK 600*, *Oerlikon Balzers* AG). After evaporation, a short ~8 sec dip in a 70°C Al-etching bath 25 : 5 : 1 H_3PO_4 (85%) : CH_3COOH (100%) : HNO_3 (70%) is performed in order to remove residual aluminum. During Al-etching AlO_x on the non-metallized area is removed. Note that under the Al front metal grid, the AlO_x layer is not affected. Finally, we deposit an anti-reflection coating at 300°C on the entire cell front in a microwave-remote PECVD Plasmalab 80+ reactor, consisting of 10 nm SiN_x ($n = 2.4$ at $\lambda = 632$ nm) and 70 nm SiN_x ($n = 2.05$ at $\lambda = 632$ nm). Before characterization each cell is annealed on a hot plate in ambient atmosphere at 330°C for 1 to 4 minutes.

7.4.2 Solar cell results

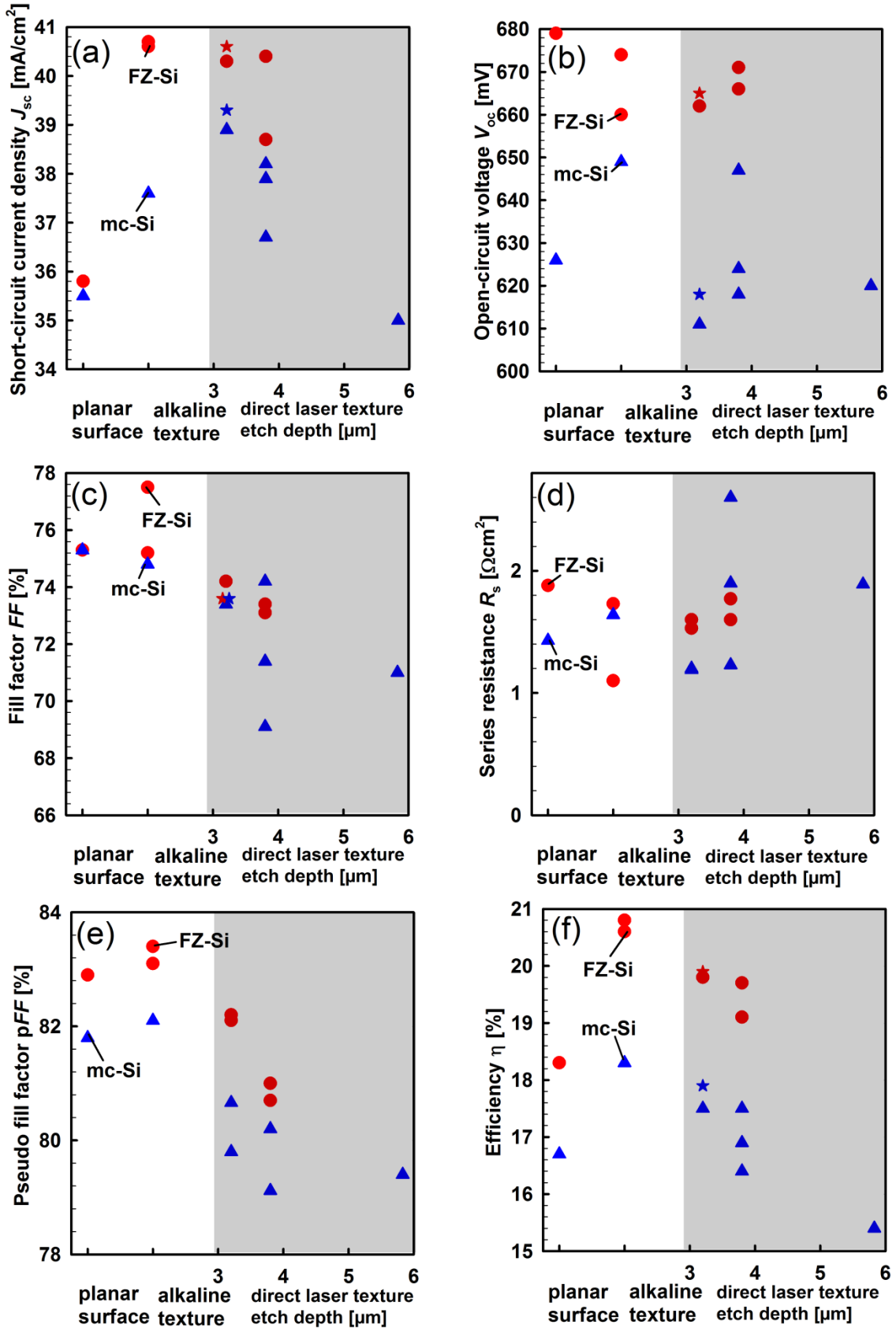

Figure 64: (a) Short-circuit current density J_{sc}, (b) open-circuit voltage V_{oc}, (c) fill factor FF, (d) Series resistance R_s, (e) pseudo fill factor (pFF), and (f) energy conversion efficiency η of FZ-Si (red circles) and mc-Si (blue triangles) PERC solar cells with planar, alkaline textured, and *DiLaT* surfaces, respectively. The solar cell parameters that have been independently measured at ISE CalLab are shown as stars. The damage etch depth is varied for the *DiLaT* process.

Table 8 summarizes the FZ-Si and mc-Si PERC solar cell results with planar, alkaline textured and *DiLaT* surfaces. Figure 64 (a) compares the measured short-circuit current densities (J_{sc}) of PERC solar cells with differently textured front surfaces. The J_{sc} values of solar cells with a planar surface are 35.5 mA/cm² for mc-Si and 35.8 mA/cm² for FZ-Si PERC solar cells. The corresponding weighted reflectance (R_{wgh}) values (weighted reflectance with AM 1.5G spectrum in the range of 340 nm to 1200 nm) are 15.3% and 16% for mc-Si and FZ-Si PERC solar cells, respectively. By applying the alkaline texturing process, the J_{sc} value increases to 37.6 mA/cm² for mc-Si and to 40.7 mA/cm² for FZ Si PERC solar cells. The increase in J_{sc} can be attributed to a decreasing R_{wgh} to 11.1% for mc-Si and to (5.6 – 6.9)% for the FZ-Si PERC solar cells. We observe a clear J_{sc} trend for our *DiLaT* PERC cells: the J_{sc} values decrease with increasing etching depth. This decrease in J_{sc} can be explained with a flattening of the texture profile with increasing etching depth. By applying *DiLaT* and an etching depth of 3.2 µm we achieve an independently confirmed J_{sc} value of 39.3 mA/cm² for mc-Si and 40.6 mA/cm² for FZ-Si PERC solar cells. Corresponding R_{wgh} values of *DiLaT* surfaces with an etching depth of 3.2 µm are in the range of (5.7 – 7.3)% for both materials. These values are comparable to the R_{wgh} values of alkaline textured FZ-Si surfaces. To our knowledge the J_{sc} of 39.3 mA/cm² was the highest reported value at the time of publication [123] for any boron-doped mc-Si solar cell, highlighting the enormous potential of our novel *DiLaT* process.

Figure 64 (b) compares the measured open-circuit voltages (V_{oc}) of the processed cells with different surface textures. The highest V_{oc} value on FZ-Si of 679 mV is obtained without texturing. Reduced V_{oc} values between 660 mV and 674 mV are achieved with alkaline textured front. The V_{oc} values of *DiLaT* FZ-Si PERC cells are between 662 mV and 671 mV and are hence comparable with the alkaline-textured FZ-Si cells. For the mc-Si solar cells, our best V_{oc} results are 649 mV for the alkaline textured and 647 mV for *DiLaT* surfaces. The larger scatter in V_{oc} values between different mc-Si solar cells result from different bulk lifetimes of the mc-Si samples, which originate from different, non-neighboring positions of the initial mc-Si wafers.

Figure 64 (c) shows the fill factors (*FF*) for solar cells with different surface texture. We obtain an average *FF* value of (75.6 ± 0.8)% for planar and alkaline textured FZ-Si and mc-Si cells. The *DiLaT* cells have a decreased average *FF* value of (72.5 ± 1.5)% for FZ-Si and mc-Si cells. The *DiLaT* process decreases the *FF*.

Figure 64 (d) shows the series resistance (R_s) for solar cells with different surface texture. The R_s value is – with one exception – in the range of 1 to 2 Ωcm². The average R_s value of (1.62 ± 0.28) Ωcm^2 does not dependent on the surface texture.

Another parameter which has a direct impact on the *FF* is the pseudo fill factor p*FF*. A reduced p*FF* might be a result of recombination in the space charge region and/or an injection dependent minority carrier lifetime and/or a shunt. Figure 64 (e) shows the p*FF* for the solar cells with different surface textures. We observe that for each type of texture the p*FF* of mc-Si solar cells is 1%$_{abs}$ lower compared to that of the FZ-Si solar cells. This observation can be explained with the injection dependence of the carrier lifetime in the multicrystalline silicon. After applying *DiLaT* with an etching depth of 3.2 µm we observe an additional drop of ~1%$_{abs}$ for mc-Si and FZ-Si solar cells. Interestingly, the p*FF* decreases further with an increasing etching depth. The p*FF* decreases from (82.2 ± 0.1)% to (80.9 ± 0.1)% for FZ-Si with a *DiLaT* texture with an etching depth of 3.2 µm and 3.8 µm, respectively. The p*FF* decreases from (80.2 ± 0.4)% to (79.8 ± 0.5)% for mc-Si with a *DiLaT* texture with an etching depth of 3.2 µm and 3.8 µm, respectively. We would expect a laser-induced damage in the silicon bulk close to the surface. Since the emitter is at the textured surface, the laser-damaged region could cause recombination within the space-charge region and consequently reduce the p*FF*. Therefore, an increased etching depth would remove the laser-induced damage and increase the p*FF*. Surprisingly, we observe the opposite trend. The p*FF* decreases with increased etching depth. Based

on our result the laser-induced damage must have a minor effect on recombination and the major effect is caused by the extended time of the silicon surface to the etching solution itself. An optimized etching solution might solve the problem.

Figure 64 (f) shows the energy conversion efficiencies (η) of the fabricated PERC solar cells. For mc-Si wafers, the best efficiency for a *DiLaT* solar cell is 17.9%, which is achieved at an etching depth of 3.2 µm. For FZ-Si, an independently confirmed efficiency of 19.9% is achieved.

Table 8: FZ-Si and mc-Si PERC solar cell results with planar, alkaline textured and *DiLaT* surfaces. Values marked with an asterisk (*) have been independently measured at ISE CalLab, Germany.

Substrate	Surface/ Etching depth	J_{sc} [mA/cm²]	V_{oc} [mV]	*FF* [%]	p*FF* [%]	η [%]	R_s [Ωcm²]
FZ-Si	Planar	35.8	679	75.3	82.9	18.3	1.88
mc-Si	Planar	35.5	626	75.3	81.8	16.7	1.43
FZ-Si	alkaline texture	40.6	660	77.5	83.1	20.8	1.1
FZ-Si	alkaline texture	40.7	674	75.2	83.4	20.6	1.73
mc-Si	alkaline texture	37.6	649	74.8	82.1	18.3	1.64
FZ-Si	*DiLaT* / 3.2 µm	40.3	662	74.2	82.1	19.8	1.6
FZ-Si	*DiLaT* / 3.2 µm	**40.6***	**665***	**73.6***	**82.2**	**19.9***	**1.53**
mc-Si	*DiLaT* / 3.2 µm	38.9	611	73.4	79.8	17.5	1.2
mc-Si	*DiLaT* / 3.2 µm	**39.3***	**618***	**73.6***	**80.7**	**17.9***	**1.19**
FZ-Si	*DiLaT* / 3.8 µm	38.7	671	73.4	80.7	19.1	1.6
FZ-Si	*DiLaT* / 3.8 µm	40.4	666	73.1	81.0	19.7	1.77
mc-Si	*DiLaT* / 3.8 µm	36.7	647	69.1	79.1	16.4	2.6
mc-Si	*DiLaT* / 3.8 µm	37.9	624	71.4	80.2	16.9	1.9
mc-Si	*DiLaT* / 3.8 µm	38.2	618	74.2	80.2	17.5	1.23
mc-Si	*DiLaT* / 5.8 µm	35.0	620	71.0	79.4	15.4	1.89

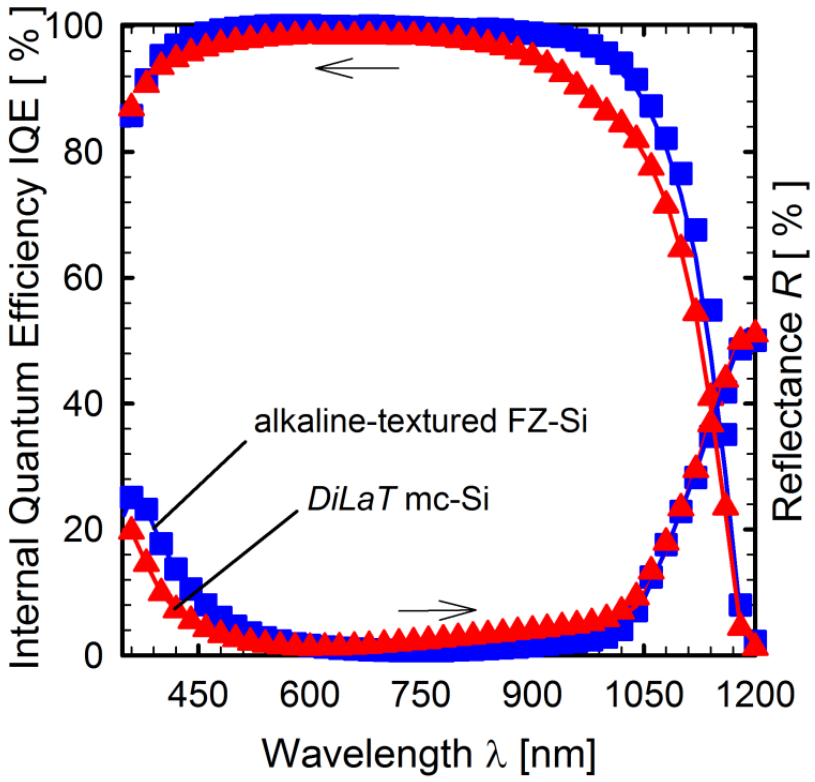

Figure 65: Measured reflectance *R* and internal quantum efficiency IQE as a function of the wavelength λ of an alkaline-textured FZ-Si (blue squares) and a *DiLaT* mc-Si (red triangles) PERC solar cell. The lines show the fitted IQE(λ) and *R*(λ) curves.

Figure 65 shows the measured spectral internal quantum efficiency IQE(λ) and reflectance *R*(λ) of a 180 µm thick mc-Si solar cell (J_{sc} = 39.3 mA/cm²) with a *DiLaT* surface and that of a 275 µm thick FZ-Si solar cell (J_{sc} = 40.6 mA/cm²) with an alkaline-textured surface. Both cells are covered with an anti-reflection coating. The *DiLaT* mc-Si cell shows a lower reflectance compared to alkaline-textured FZ-Si cell in the wavelength range between 360 nm and 650 nm. However, in the wavelength range from 650 nm to 1050 nm, the *DiLaT* mc-Si cell shows an increased reflectance, probably due to the position-dependent surface angles with respect to the wafer normal, resulting in varying position-dependent thicknesses of the anti-reflection coating. In order to model the wavelength-dependent IQE(λ) and reflectance *R*(λ), we use the software LASSIE [6] and our in-house developed software for solar cell analysis SCAN [126], [127]. For the FZ-Si solar cell we obtain a minimum minority-carrier diffusion length of L_{mins} = 803 µm and a maximum rear surface recombination velocity S_{max} = 132 cm/s. For the wavelength enhancement factor *Z* [128] we determine a value in the range between 18 and 21 at λ = 1200 nm. For the mc-Si solar cell we obtain a reduced L_{mins} value of 265 µm and an increased S_{max} value of 1054 cm/s. The reduced IQE(λ) of the *DiLaT* mc-Si solar cell is mainly due to the increased contribution of recombination in the bulk and/or at the rear of the mc-Si solar cell, which leads, however, to a still excellent J_{sc} of 39.3 mA/cm². The wavelength enhancement factor *Z* of the mc-Si solar cell is in the range between 22 and 23 at λ=1200 nm, which is comparable to that of the alkaline-textured random-pyramid FZ-Si solar cell.

7.5 Chapter summary

In this Chapter, we have implemented our direct laser texturing (*DiLaT*) process into PERC solar cells fabricated on mono- and multicrystalline silicon wafers. We have optimized the *DiLaT* profile by applying different etching depths of 3.2 µm, 3.8 µm and 5.8 µm and found that the smallest applied etching depth of 3.2 µm results in the best cell performance. On FZ-Si substrates, we have obtained similar cell parameters for the *DiLaT* as compared to random-pyramid texturing, with best V_{oc} and J_{sc} values of 671 mV and 40.6 mA/cm² for *DiLaT* as compared to 674 mV and 40.7 mA/cm² for random-pyramid texturing, respectively. By modeling the reflectance curves, we have obtained average light path enhancement factors Z in the range of 22 to 23 for *DiLaT* and in the range of 18 to 21 for alkaline-textured cells. *DiLaT* resulted in independently confirmed energy conversion efficiencies of 19.9% on FZ-Si and 17.9% on mc-Si material. On mc-Si, we have achieved an independently confirmed J_{sc} value of 39.3 mA/cm² by our novel *DiLaT* process, which was the highest achieved J_{sc} value at the time of publication [123], highlighting the enormous potential of *DiLaT* for the application to mc-Si solar cells.

8 Summary

In this thesis, we have demonstrated the application of ultrathin ALD-AlO_x as a contact passivating tunneling layer between the phosphorus-doped n^+-emitter and the Al-evaporated front metal grid of a PERC solar cell. We have identified an optimal nominal ALD-AlO_x layer thickness of 0.24 nm, which effectively passivates the Al contact, prevents the Al-spiking and allows for a suitable current transport from the n^+-emitter into the Al metal contact. Increasing the AlO_x thickness above 0.24 nm led to a drastic decrease in fill factor, and hence a reduced conversion efficiency. The *FF* decreased from a median value of 79.3% to a median value of 53.7% for PERC solar cells with a nominal AlO_x thickness of 0.24 nm and 0.48 nm, respectively. The best PERC solar cell fabricated in this work showed an independently confirmed record-high efficiency of 21.7% and a V_{oc} of 673 mV. Importantly, the solar cells with implemented AlO_x tunneling layers showed an improved reproducibility and only small variations in the cell parameters. An 0.24 nm thick AlO_x tunneling layer led to a nearly 8 times larger R_{sh} compared to cells without AlO_x layer, preventing aluminum to spike through the n^+-emitter during the SiN_x deposition at 300°C and subsequent annealing at 350°C. The J_{0_total} values of (174 ± 11) fA/cm^2 of a PERC cell with ALD-AlO_x passivated contact compared to the J_{0_total} values of (320 ± 41) fA/cm^2 of a PERC cell with non-passivated contact clearly demonstrated a highly effective contact passivation of our ALD-AlO_x tunneling layer. Applying our ultrathin AlO_x layer deposited by only two ALD cycles between the n^+-emitter and Al metal grid, we reduced the saturation current density of the metallized area by at least a factor of 4.8. For the first time, we have successfully reduced the recombination at the metal contact of an electron contact region by introducing a passivating tunneling layer based on ALD-AlO_x.

We have performed an in-depth analysis of organic-silicon heterojunctions based on the hole-conducting polymer PEDOT:PSS. Using photoconductance decay lifetime measurements we have determined for the first time the J_0 value of the PEDOT:PSS/c-Si heterojunction. We have measured J_0 values of 208 fA/cm² on RP-textured silicon surface and J_0 values of 80 fA/cm² on planar silicon surfaces, respectively. The surprisingly low J_0 value of 80 fA/cm² was the first hint towards the high efficiency potential of the PEDOT:PSS/c-Si heterojunction solar cells. We have realized heterojunction solar cells with PEDOT:PSS on c-Si *n*-type silicon wafers front surfaces and achieved a record-high efficiency at the time of publication of 12.3%. This efficiency was achieved by implementing an RP-texture on the front surface and an n^+-BSF on the rear surface of our solar cell architecture. We have investigated the optical properties of PEDOT:PSS layers via ellipsometry and transmission measurements and performed ray-tracing simulations of a solar cell where the PEDOT:PSS layer is on the RP-textured front surface or on the planar rear surface. Our optical measurements in combination with the ray-tracing simulations have shown that the solar cell with PEDOT:PSS layer on the RP-textured front surface could realistically reach a J_{sc} of 34.1 mA/cm², and solar cell with PEDOT:PSS layer on the planar rear surface could realistically reach a J_{sc} of 40.5 mA/cm², respectively. We have introduced a novel solar cell concept – the so-called *BackPEDOT* solar cell – where the advantage of a PEDOT:PSS layer on the planar rear could realistically reach a J_{sc} of 40.5 mA/cm², a V_{oc} of 667 mV and an efficiency of 22.0%.

We have realized first *BackPEDOT* experimental devices, which achieved a remarkably high V_{oc} of 663 mV and a J_{sc} of 39.7 mA/cm^2. The *J-V* curves showed a high pseudo fill factor of up to p*FF* = 82.0%. However, the actual fill factors were largely limited by a high series resistance which was in the range between 2.88 and 3.35 Ωcm^2. By optimizing the PEDOT:PSS dispersion and the silicon surface pre-treatment we were able to achieve J_0 values of 46 fA/cm² and contact resistance values of R_C = (490 ± 210) mΩcm². We successfully implemented our optimal silicon treatment,

which is a native SiO_x grown for less than 10 mins, and the optimized PEDOT:PSS composition to *BackPEDOT* solar cells and achieved series resistance values of $R_s < 1$ Ωcm² and V_{oc} values of (653 – 659) mV. Our lowest series resistance of 0.5 Ωcm² resulted in a *FF* of 80.6%. Combining the high *FF* value with a short-circuit current density of 38.9 mA/cm², an outstanding efficiency of 20.6% was achieved, which is by far the highest efficiency for a PEDOT:PSS/c-Si solar cell to date.

Organic-based devices are well known to be prone to the degradation. Here, we have performed degradation experiments on our PEDOT:PSS/c-Si heterojunction solar cells. Storage was performed in air at approximately 23°C and 65% relative humidity. We observed a comparable degradation behavior of the efficiency for *FrontPEDOT* and *BackPEDOT* solar cells. The relative efficiency degradation followed a simple exponential decay with the corresponding degradation time constant t_{deg} of (28 ± 1.6) days. The illuminated *J-V* curves showed an '*S*-shaped' form with increasing time in air, indicating a barrier formation for the charge carrier transport. The contact resistance R_C has been identified as the most affected solar cell parameter during degradation. The R_C value increased by factor of 8 after storing the R_C samples in ambient air for 88 hours. By storing organic-silicon solar cell in dehumidified environment (in a desiccator) the t_{deg} was extended to 1615 days, showing that humidity is the major source of degradation. In our first approach, to stabilize the cells, we have encapsulated a *FrontPEDOT* solar cell by a 30 nm thick ALD-Al_2O_3 layer, extending the t_{deg} to 203 days. Second, we applied a novel encapsulation method for *BackPEDOT* solar cells by putting a metal foil on the rear surface. With this encapsulating method the efficiency was stable for 600 hours so far. We have discussed possible degradation mechanisms: (i) the formation of an SiO_x layer at the PEDOT:PSS/c-Si interface and (ii) alternation of the band alignments of the PEDOT:PSS layer caused by storage in humid environment. Based on TEM images of the degraded PEDOT:PSS/c-Si interface we have excluded the formation of a closed SiO_x layer. However, using Kelvin-probe measurements, we detected a decreasing work function W_A difference of the PEDOT:PSS/c-Si samples stored in air. After 26 hour in air the W_A difference reaches a value of + (119 – 150) mV. On the PEDOT:PSS/Ag samples stored air, the W_A difference reaches a value of + (91 – 122) mV after 60 hours. Comparing the Kelvin-probe measurements of the PEDOT:PSS/c-Si and the PEDOT:PSS/Ag, samples we were able to attribute the observed degradation to the change of the PEDOT:PSS work function. We developed a model, where a decreasing W_A of the PEDOT:PSS with time in air alters the band configuration, forming a barrier for hole transport from silicon into PEDOT:PSS. With this detailed analysis of the degradation mechanism and with our novel approaches towards effective encapsulation, an important step has been made towards fully stabilized *BackPEDOT* solar cells.

We have fabricated lab-type PERC solar cells on float-zone silicon, block-cast multicrystalline silicon (mc-Si) from an industrial supplier and mc-Si from a laboratory-scale high-purity crucible. On the multicrystalline material from the high-purity crucible we achieved record-high V_{oc} values of up to 659 mV. The open-circuit voltage of our best multicrystalline silicon solar cell was only 1 mV lower compared to SENTAURUS Device simulations, where the bulk lifetime was assumed to be limited by Auger recombination. For commercially available standard multicrystalline silicon material, however, the highest measured open-circuit voltages are 8 mV – 9 mV reduced compared to our simulations, implying that the efficiency of today's industrial multicrystalline silicon solar cells is predominantly limited by regions of high defect and impurity concentrations. Our cell results based on multicrystalline silicon material casted in high-purity crucibles show that the reduced bulk quality commonly observed in standard multicrystalline silicon material is largely avoidable using a high-purity crucible during casting and by extending monocrystalline areas. On a selected area of 1 × 1 cm² we have achieved a very high solar cell efficiency of 20% on the mc-Si high-purity mc-Si material. Note that during the time of publication this efficiency was only slightly below the record value of 20.4% [111], [123] for a 1 cm² solar cell.

In the last part of this thesis, we have implemented a direct laser texturing (*DiLaT*) process into PERC solar cells fabricated on mono- and multicrystalline silicon wafers. The advantage of the *DiLaT* texture is its applicability to any crystal orientation and the absence of any masking layer. We have optimized the *DiLaT* profile by applying different etching depths of 3.2 µm, 3.8 µm and 5.8 µm and found that the smallest applied etching depth of 3.2 µm resulted in the best cell performance. On FZ-Si substrates we have obtained similar cell parameters for the *DiLaT* as compared to random-pyramid texturing, with best V_{oc} and J_{sc} values of 671 mV and 40.6 mA/cm² for *DiLaT* as compared to 674 mV and 40.7 mA/cm² for random-pyramid texturing, respectively. By modeling the reflectance curves, we have determined average light path enhancement factors in the range of 22 to 23 for *DiLaT* and in the range of 18 to 21 for alkaline-textured solar cells. *DiLaT* resulted in independently confirmed energy conversion efficiencies of 19.9% on FZ-Si and 17.9% on mc-Si material, respectively. On mc-Si, we have achieved an independently confirmed J_{sc} value of 39.3 mA/cm², which is the highest reported J_{sc} value at the time of publication for any mc-Si solar cell, highlighting the enormous potential of *DiLaT* for the application to mc-Si solar cells.

9 Bibliography

[1] A. Cuevas, J. Bullock, Y. Wan, Di and X. Zang, „Skin Care for Healthy Silicon Solar Cells," *42nd IEEE Photovoltaic Specialist Conference (PVSC),* pp. 1-6, 2015.

[2] P. Würfel, Physics of Solar Cells From Principles to New Concepts, Weinheim: WILEY-VCH Verlag GmbH & Co, KGaA, 2005.

[3] A. Fell, „A Free and Fast Three-Dimensional/Two-Dimensional Solar Cell Simulator Featuring Conductive Boundary and Quasi-Neutrality Approximations," *IEEE Trans. Electron Devices,* 60(2), pp. 733-738, 2012.

[4] J. Petermann, „Prozessentwicklung & Verlustanalyse für dünne monokristalline Solarzellen und deren Prozessierung auf Modullevel," *PhD thessis, Gottfried Wilhelm Leibniz Universität Hannover,* 2014.

[5] R. Brendel, T. Dullweber, R. R. Peibst, C. Kranz, A. Merkle and D. Walter, „Breakdown of the Efficiency Gap to 29% Based on Experimental Input Data and Modelling," *Proceedings of the 31st European Photovoltaic Solar Energy Conference and Exhibition,* pp. 264 - 272, 2015.

[6] B. Fischer, pv-tools GmbH, 2015. [Online]. Available: http://www.pv-tools.de/. [2015].

[7] A. Goetzberger, B. Voß and J. Knobloch, Sonnenenegie: Photovoltaic, Freiburg: Teubner Studienbücker Physik, 1997.

[8] Sze S. M., SEMICONDUCTOR DEVICES Physics and Technology, Murray Hill, New Jersey: John Wiley & Sons, 1985.

[9] J. D. Cuthbert, „Recombination Kinetics of Excitonic Molecules and Free Excitons in Intrinsic Silicon," *Phys. Rev. B,* 1, pp. 1552-1557, 1970.

[10] J. Dziewior and W. Schmidt, „Auger coefficient for highly doped and highly excited silicon," *Appl. Phys. Lett.,* 31, p. 346, 1977.

[11] A. Hangleiter and R. Häcker, „Enhancement of band-to-band Auger recombination by electron-hole correlations," *Phys. Rev. Lett.,* 65, pp. 215-18, 1990.

[12] A. Richter, J. Benick, M. Hermle and S. W. Glunz, *Phys. Status Solidi RRL,* 5, p. 202, 2011.

[13] A. Cuevas, M. Stocks, D. Macdonald and R. Sinton, „Applications of the quasi-steady-state photoconductance technique," *Proceedings of the 2nd World Conference on Photovoltaic Energy Conversion, Vienna, Austria,* 1998.

[14] A. B. Sproul, „Dimensionless solution of the equation describing the effect of surface recombination on carrier decay in semiconductors," *J. Appl. Phys.,* 76, Nr. 5, p. 285, 1994.

[15] D. E. Kane and R. M. Swanson, „Measurement of theemitter saturation current by a contactless photoconductivity decay method," *Proc. 18th IEEE PVSC,. Las Vegas, USA,* pp. 578-581, 1985.

[16] K. Bothe, „ Oxygen-related trapping and recombination centres in boron-doped crystalline silicon," *PhD thessis, Gottfried Wilhelm Leibniz, Universität, Hannover,* 2006.

[17] R. Sinton and A. Cuevas, „Contactless determination of current–voltage charac-teristics and minority-carrier lifetimes in semiconductors from quasi-steady-state photoconductance data," *Appl. Phys. Lett.,* 2510, p. 69, 1996.

[18] B. Lim, Boron-oxygen-related recombination centers in crystalline silicon and the effects of dopant-compensation, Hannover: Leibniz Universität Hannover, 2012.

[19] R. Sinton, Sinton Consulting Inc., [Online]. Available: http://www.sintoninstruments.com/Sinton-Instruments-WCT-120.html. [2016].

[20] K. Ramspeck, K. Bothe, J. J. Schmidt and R. Brendel, „Combined dynamic and steady-state infrared camera based carrier lifetime imaging of silicon wafers“ *J. Appl. Phys.,* 106, p. 114506, 2009.

[21] S. Herlufsen, „Characterization of crystalline silicon based on measurements of the photoluminescence emission,“ *PhD thesis, Gottfried Wilhelm Leibniz Universität Hannover,* 2013.

[22] K. Ramspeck, „Characterization techniques for silicon solar cells and material using an infrared-camera based approach,“ *PhD thesis, Gottfried Wilhelm Leibniz Universität Hannover,* 2009.

[23] S. Herlufsen, J. Schmidt, D. Hinken, K. Bothe and R. Brendel, „Photoconductance-calibrated photoluminescence lifetime imaging of crystalline silicon,“ *Phys. Status Solidi RRL.,* 2, p. 245–247, 2008.

[24] International Technology Roadmap for Photovoltaics (ITRPV), Frankfurt am Main: VDMA, 2016.

[25] W. Kern and D. Puotinen, „ Cleaning solutions based on hydrogen peroxide for use in silicon semiconductor technology,“ *RCA Review,* 31, p. 187, 1970.

[26] T. Lauinger, M. J., A. Aberle and R. Hezel, „Record low surface recombination velocities on 1 Ω cm p-silicon using remote plasma silicon nitride passivation,“ *J. Vac. Sci. Technol., A,* 16, pp. 530-543, 1998.

[27] J. Schmidt, J. D. Moschner, J. Henze, D. S. and R. Hezel, „Recent progress in the surface passivation of silicon solar cells using silicon nitride,“ *Proceedings of the19th European Photovoltaic Solar Energy Conference, Paris, France,* pp. 391-396, 2004.

[28] A. Kimmerle, J. Greulich and A. Wolf, „Carrier-diffusion corrected J0-analysis of charge carrier lifetime measurements for increased consistency,“ *Sol. Energy Mater. Sol.,* 142, pp. 116-122, 2015.

[29] G. Agostinelli, A. Delabie, P. Vitanov, Z. Alexieva, H. F. W. Dekkers, S. D. Wolf and G. Beaucarne, „Very low surface recombination velocities on p-type silicon wafers passivated with a dielectric with fixed negative charge,“ *Sol. Energy Mater. Sol. Cells,* 90, p. 3438, 2006.

[30] B. Hoex, S. Heil, E. Langereis, M. C. M. van de Sanden and W. Kessels, *Appl. Phys. Lett.,* 89, p. 042112, 2006.

[31] F. Werner, Atomic layer deposition of aluminum oxide on crystalline silicon: Fandamental interface properties and application to solar cells, Leibniz Universität Hannover: *PhD thessis*, 2014.

[32] F. Werner, B. Veith, D. Zielke, L. T. C. Kühnemund, M. Seibt, R. Brendel and J. Schmidt, „Electronic and chemical properties of the c-Si/Al2O3 interface,“ *J. Appl. Phys.,* 109, pp. 113701 01-06, 2011.

[33] J. Schmidt, A. Merkle, R. Brendel, B. Hoex, M. C. M. v. d. Sanden and a. W. M. M. Kessels, „Surface Passivation of High-efficiency Silicon Solar Cells by Atomic-layer-deposited Al2O3,“ *Photovolt. , Res. Appl.,* 16, p. 461, 2008.

[34] T. Dullweber, C. Kranz, R. Peibst, U. Baumann, H. Hannebauer, A. Fülle, S. Steckemetz, T. Weber, M. Kutzer, M. Müller, G. Fischer, P. Palinginis and H. Neuhaus, „PERC+: industrial PERC solar cells with rear Al grid enabling bifaciality and reduced Al paste consumption.,“

Prog. Photovolt: Res. Appl., EU PVSEC Paper, 2015.

[35] B. Veith, Oberflächenpassivierung von Silicium mit atomlagenabgeschiedenem Aluminiumoxid, Leibniz Universität Hannover, *Diploma thesis*, 2009.

[36] R. Hezel and A. Metz, „Crystalline silicon solar cells with efficiencies above 20% suitable for mass production.," *Proceedings of the 16th European Photo-voltaic Solar Energy Conference, Glasgow, UK,* p. 1091–1094, 2000.

[37] H. R. Metz A, „Record efficiencies above 21% for MIS-contacted diffused junction silicon solar cells," *Proceedings of the 26th IEEE Photovoltaic Specialist Conference, Anaheim, CA ,* pp. 283-286, 1997.

[38] D. Zielke, J. H. Petermann, F. Werner, B. Veith, R. Brendel and J. Schmidt, „21.7 % efficient PERC solar cell with AlOx tunneling layer," *Proceedings 26th EU PVSEC,* 2011.

[39] D. Zielke, J. H. Petermann, F. Werner, B. Veith, R. Brendel and J. Schmidt, "Contact passivation in silicon solar cells using atomic-layer-deposited aluminum oxide layers," *Phys. Status Solidi RRL,* vol. 5, pp. 298-300, 2011.

[40] P. P. Altermatt, G. Heiser, A. G. Aberle, A. Wang, J. Zhao, S. J. Robinson, S. Bowden and M. A. Green, „Spatially Resolved Analysis and Minimization of Resistive Losses in High-eficiency Si Solar Cells," *Prog. Photovoltaics Res. Appl.,* 4, pp. 399 - 413, 1996.

[41] J. H. Petermann, D. Zielke, J. Schmidt, F. Haase, E. G. Rojas and R. Beandel, „19% - efficient and 43 µm - thick crystalline Si solar cell from layer transfer using porous silicon," *Prog. Photovolt: Res. Appl.,* 20, Nr. 1, pp. 1-5, 2011.

[42] M. A. Green, K. Emery, Y. Hishikawa, W. Warta and E. D. Dunlop, „Solar cell efficiency tables (Version 38)," *Prog. Photovolt: Res. Appl.,* 19, pp. 564-572, 2011.

[43] B. Fischer, „Loss analysis of crystalline silicon solar cells using photoconductance and quantum efficiency measurements," *PhD,* 2003.

[44] X. Loozen, J. B. Larsen, F. Dross, M. Aleman, T. Bearda, B. J. O'Sullivan, I. Gordon and J. Poortmans, „Passivation of a Metal Contact with a Tunneling Layer," *Energy Procedia,* 21, pp. 75-83, 2012.

[45] J. Deckers, E. Cornagliotti, Debucquoy., I. Gordon, R. Mertens and J. Poortmans, „Aluminum oxide-aluminum stacks for contact passivation in silicon solar cells," *Energy Procedia,* 55, pp. 656-664, 2014.

[46] J. Bullock, D. Yan and A. Cuevas, "Passivation of aluminum-n+ silicon contacts for solar cells by ultrathin Al2O3 and SiO2 dielectric layers," *Phys. Status Solidi RRL,* vol. 11, pp. 946-949, 2013.

[47] D. Zielke, „Rückseitenpassivierung von kristallinen Siliciumsolarzellen mit Aluminiumoxid," *Diploma thesis,* 2010.

[48] V. Naumann, M. Otto, R. B. Wehrspohn and C. Hagendorf, „Chemical and structural study of electrically passivating Al2O3/Si interfaces prepared by atomic layer deposition," *Journal of Vacuum Science & Technology,* A 30, p. 04D106, 2012.

[49] M. A. Green, K. Emery, Y. Hishikawa, W. Warta and D. Dunlop, „Solar cell efficiency tables (Version 45)," *Prog. Photovolt: Res. Appl.,* 23, pp. 1-9, 2014.

[50] M. Liu, M. B. Johnston and S. H. J., „Efficient planar heterojunction perovskite solar cells by vapour deposition," *Nature,* 501, pp. 395-398, 2013.

[51] J. H. Noh, S. Im, J. H. Heo, T. H. Mandal and S. I. Seok, „Chemical Management for Colorfull, Efficient, and Stable Inorganic-Organic Hybrid Nanostructured Solar Cells," *Nano Letters,* 13,

pp. 1764-1769, 2013.

[52] S. Avasthi, S. Lee, Y.-L. Loo and J. C. Sturm, „ Role of Majority and Minority Carrier Barriers Silicon/Organic Hybrid Heterojunction Solar Cells," *Adv. Mater.,* 23, p. 5762–5766, 2011.

[53] L. He, C. Jiang, H. Wang, H. Lei, D. Lai and Rusli, „11.3% efficient planar Si-PEDOT:PSS hybrid solar cell with a thin interfacial oxide," *Photovoltaic Specialists Conference (PVSC), 2012 38th IEEE ,* pp. 002785 - 002787, 2012.

[54] L. He, C. Jiang, H. Wang, D. Lai and Rusli, „High efficiency planar Si/organic heterojunction hybrid solar cells," *Appl. Phys. Lett.,* 100, pp. 073503 1-3, 2012.

[55] M. Rehahn, „Der Weg zu einer neuen Materialklasse: Elektrisch leitfähige Kunststoffe," *Chem. Unserer Zeit,* 37, pp. 18-30, 2003.

[56] A. Elschner, S. Kirchmeyer, W. Loevenich, U. Merker and K. Reuter, PEDOT Principles and Applications of an Intrinsically Conductive Polymer, CRC Press, 2011.

[57] U. Müller, Anorganische Srukturchemie 6. Auflage, Wiesbaden: VIEWER+TEUBNER, 2008.

[58] C. K. Chiang, C. B. Fincher, J. Y. W. Park, A. J. Heeger, H. Shirakawa, E. J. G. S. C. Louis and A. G. MacDiarmid, „Electrical Conductivity in Doped Polyacetylene," *Phys. Rev. Lett.,* 39, Nr. 17, pp. 1098-1101, 1977.

[59] O. Niwa, M. Hikita and T. Tamamura, „Electrical properties of poly(vinyl chlorids)-polypyrrole conductive polymer alloy films," *Makromat. Chem., Rapid Commun.,* 6, pp. 375-379, 1985.

[60] R. Waltman, J. Bargon and A. F. Diaz, „Electrochemical studies of some conducting polythiophene films," *J. Phys. Chem.,* 87, pp. 1459-1463, 1983.

[61] A. Elschner, Autor, *Das leitfähige Polymer PEDOT:PSS als Funktionsschicht in optoelektrischen Anwendungen.* [Performance]. Heraeus Deutschland GmbH, 2014.

[62] F. Jonas, G. Heywang and W. Schmidtberg, „Neue polythiophene, verfahren zu ihrer herstellung and ihre verwendung". Deutschland Patent DE 3813589 , 22 April 1988.

[63] C. Niehaves, Charakteresierung von Polymer / Si-Heteroübergängen für Solarzellen, Leibniz Universität Hannover, Georg-August Universität Göttingen, 2014.

[64] V. Titova, Herstellung and Charakterisierung von organischen Schichten für die Anwendung in kristallinen Silicium-Solarzellen., Leibniz Universität Hannover, Hochschule für Angewandte Wissenschaften Hamburg, 2013.

[65] R. Brendel, *Sunrays 1.3, MPI-FKF D-70569 Stuttgart, Germany.*

[66] D. Zielke, A. Pazidis, F. Werner and J. Schmidt, „Organic-silicon heterojunction solar cells on n-type silicon wafers: The BackPEDOT concept," *Sol. Energy Mater. Sol. Cells,* 131, pp. 110-116, 2014.

[67] C. Liu, Z. Su, W. Li, F. Jin, B. Chu, J. Wang, H. Zhao, C. Lee, J. Tang and B. Kang, „Improved performance of perovskite solar cells with a TiO2/MoO3 core/shell nanoparticles doped PEDOT:PSS hole-transporter," *Org. Electron.,* 33, p. 221–226, 2016.

[68] M. Vogt, Simulation der streuenden Reflexion an Nanotröpfchen auf der Rückseite von Silizium-Solarzellen, Hannover: Leibniz Universität Hannover, 2011.

[69] J. Schmidt, V. Titova and D. Zielke, „Organic-silicon heterojunction solar cells: Open-circuit voltage potential and stability," *Appl. Phys. Lett.,* pp. 183901-1-4, 2013.

[70] M. A. Green, Solar cells: Operating Principles, Technology and System Applications, Kensington: Published by The University of New South Wales , 1992.

[71] N. Chen and A. Ebong, „Towards 20% efficient industrial Al-BSF silicon solar cell with multiple busbars and fine gridlines," *Sol. Energy Mater. Sol. Cells,* 146, pp. 107-113, 2016.

[72] D. Zielke, C. Niehaves, W. Lövenich, A. Elschner, M. Hörteis and J. Schnidt, „Organic-silicon solar cells exceeding 20% efficiency," *Energy Procedia,* 77, pp. 331-339, 2015.

[73] R. Gogolin, D. Zielke, W. Lövenich, R. Sauer and J. Schmidt, „Silicon heterojunction solar cells combining an a-Si:H electron-collector with a PEDOT:PSS hole-collector," *to be presented at the SiliconPV, Chambéry, France,* 2016.

[74] U. Römer, R. Peibst, T. Ohrdes, B. Lim, J. Krügener, E. Bugiel, T. Wietler and R. Brendel, „Recombination behavior and contact resistance of n+ and p+ poly-crystalline Si/mono-crystalline Si junctions," *Sol. Energy Mater. Sol. Cells,* 131, pp. 85-91, 2014.

[75] Y. Zhang, R. Liu, S. T. Lee and B. Sun, „The role of a LiF layer on the performance of poly(3,4-ethylenedioxythiophene):poly(styrenesulfonate)/Si organic-inorganic hybrid solar cells," *Appl. Phys. Lett.,* 104, pp. 083514-1 - 4, 2014.

[76] S. Avasthi, K. A. Nagamatsu, J. Jhaveri, W. E. McClain, G. Man, A. Kahn, J. Schwartz, S. Wagner and J. C. Sturm, „Double-Heterojunction Crystalline Silicon Solar Cell Fabricated at 250°C with 12.9 % Effi ciency," *IiEEE Journ al of Photovoltaics,* pp. 949-953, 2014.

[77] J. Wagner, M. Gruber, A. Wilke, Y. Tanaka, K. Topczak, A. Steindamm, U. Hörmann, A. Opitz, Y. Nakayama, H. Ishii, J. Pflaum, N. Koch and W. Brütting, „Identification of different origins for s-shaped current voltage characteristics in planar heterojunction organic solar cells," *J. Appl. Phys.,* 111, pp. 054509-1-12, 2012.

[78] A. Kumar, S. Sista and Y. Yang, „Dipole induced anomalous S-shape I-V curves in polymer solar cells," *J. Appl. Phys.,* 105, pp. 094512-1-6, 2009.

[79] F. J. Garciıa-Sanchez, D. Lugo-Munoz and J. Muci, „Lumped Parameter Modeling of Organic Solar Cells' S-Shaped I–V Characteristics," *IEEE J. of photovoltaics,* 3, Nr. 1, pp. 330-335, 2013.

[80] A. Wagenpfahl, D. Rauh, M. Binder, C. Deibel and V. Dyakonov, „S-shaped current-voltage characteristics of organic solar devices," *Phys. Rev. B,* 82, pp. 115306 1-8, 2010.

[81] A. Froitzheim, K. Brendel, L. Elstner, W. Fuhs, K. Kliefoth and S. M, „Interface recombination in heterojunctions of amorphous and crystalline silicon," *Journal of Non-Crystalline Solids,* pp. 663 - 667, 2002.

[82] T. F. Schulze, L. Korte, E. Conrad, M. Schmidt and R. B., „Electrical transport mechanisms in a-Si:H/c-Si heterojunction solar cells," *J. Appl. Phys.,* 107, Nr. 2, pp. 023711-1-14, 2010.

[83] K. Li, H. Fan, C. Huang, X. Hong, X. Fang, H. Li, X. Liu, C. Li, Z. Huang and H. Zhen, „Thin-film encapsulation of inverted indium-tin-oxide-free polymer solar cells by atomic layer deposition with improvement on stability and efficiency," *Appl. Phys. Lett.,* 101, p. 233902 , 2012.

[84] J. Schmidt, D. Zielke, R. Gogolin, R. Sauer and W. Lövenich, „Recent Advances in Polymer/Silicon Heterojunction Solar Cells," *presented at the 32th Europ. Photovolt. Solar Energy Conf., Munich, Germany (WIP, Munich),* 2016.

[85] S. Jäckle, M. Liebhaber, J. Niederhausen, M. Büchele, R. Félix, R. G. Wilks, M. Baer, K. Lips and S. H. Christiansen, „Unveiling the hybrid n-Si/PEDOT:PSS interface," *ACS Appl. Mater. Interfaces,* 8(13), p. 8841–8848, 2016.

[86] R. Williams, „Photoemission of electrons from silicon into silicon dioxide," *Phys. Rev.,* 140, pp. 569-775, 1965.

[87] M. Jørgensen, K. Norrman and F. C. Krebs, „Stability/degradation of polymer solar cells," *Sol.*

Energy Mater. Sol. Cells, 92, pp. 686-714, 2008.

[88] L. Kelvin, „Contact electricity of metals," *Philosophical Magazine,* 46, p. 82–120, 1898.

[89] P. P. Craig and V. Radeka, „Stress Dependence of Contact Potential: The ac Kelvin Method," *Rev. Sci. Instrum.,* 41, p. 258, 1970.

[90] M. Nonnenmacher, M. P. O'Boyle and H. K. Wickramasinghe, „Kelvin probe force microscopy," *Appl. Phys. Lett.,* 58, pp. 2921-2923, 1991.

[91] N. Koch, A. Vollmer, A. Elschner, "Influence of water on the work function of conducting poly(3,4-ethylenedioxythiophene)/poly(styrenesulfonate)", *Appl. Phy Lett.* 90, pp. 043512-1 – 3, 2007.

[92] D. Macdonald, A. Cuevas, A. Kinomura, Y. Nakano and L. J. Geerligs, „Transition-metal profiles in a multicrystalline silicon ingot," *J. Appl. Phys.,* 97, p. 033523, 2005.

[93] T. Buonassisi, A. A. Istratov, M. D. Pickett, M. Heuer, J. P. Kalejs, G. Hahn, M. A. Marcus, B. Lai, Z. Cai, S. M. Heald, T. F. Ciszek, R. F. Clark, D. W. Cunningham, A. M. Gabor, R. Jonczyk, S. Narayanan, E. Sauar and E. R. Weber, „Chemical Natures and Distributions of Metal Impurities in Multicrystalline Silicon Materials," *Prog. Photovolt: Res. Appl.,* 14, pp. 513-531, 2006.

[94] J. R. Davis, A. Rohatgi, R. H. Hopkins, P. D. Blais, P. Rai-Choudhury, J. R. McCormick and H. C. Mollenkopf, „Impurities in silicon solar cells," *IEEE Trans. on Electron,* 27, Nr. 4, p. 677–687, 1980.

[95] J. S. Kang and D. K. Schroder, „Gettering in silicon," *J. Appl. Phys.,* 65, pp. 2974-2985, 1989.

[96] W. Kwapil, A. Zuschlag, I. Reis, I. Schwirtlich, S. Meyer, R. Zierer, R. Krain, F. M. Kießling, M. Schumann, C. Schmidt and S. Riepe, „Influence of Crucible and Coating on the Contamination of Directionally Solidified Silicon: First Results of the German Research Network »SolarWinS«," *Proceedings of the 27th EU PVSEC. Frankfurt, Germany,* pp. 627 - 635, 2012.

[97] T. Saito, A. Shimura and S. Ichikawa, „A new directional solidification technique for polycrystalline solar grade silicon," *15th Photovoltaic Specialists Conference, Kissimmee, FL, USA,* pp. 576-580, 1981.

[98] ITRPV, „International Technology Roadmap for Photovoltaic," 2015.

[99] D. Gilles, W. Schröter and W. Bergholz, „Impact of the electronic structure on the solubility and diffusion of 3d transition elements in silicon," *Phys. Rev. B,* 41, pp. 5770-5782, 1990.

[100] A. Cuevas, M. Stocks, S. Armand, M. Stuckings and A. Blackers, „High minority carrier lifetime in phosphorus-gettered multicrystalline silicon," *Appl. Phys. Lett.,* 70, pp. 1017-1029, 1997.

[101] S. Herlufsen, D. Macdonald, K. Bothe and J. Schmidt, „Imaging of the interstitial iron concentration in crystalline silicon by measuring the dissociation rate of iron–boron pairs," *Phys. Status Solidi RRL,* 6, Nr. 1, pp. 1-3, 2012.

[102] H. Nagel, J. Schmidt, A. G. Aberle and R. Hezel, „Exceptionally high bulk minority-carrier lifetimes in block-cast multicrystalline silicon," *Proceedings of the 14th European Photovoltaic Solar Energy Conference, Barcelona, Spain,* p. 762, 1997.

[103] P. Karzel, A. Frey, S. Fritz and G. Hahn, „Influence of hydrogen on interstitial iron concentration in multicrystalline silicon during annealing steps," *Appl. Phys. Lett.,* 113, pp. 114903-1 - 114903-9, 2013.

[104] J. H. Petermann, T. Ohrdes, P. P. Altermatt, S. Eidelloth and R. Brendel, „19% Efficient Thin-Film Crystalline Silicon Solar Cells From Layer Transfer Using Porous Silicon: A Loss

Analysis by Means of Three-Dimensional Simulations," *IEEE TRANSACTIONS ON ELECTRON DEVICES,* 59, pp. 909-917, 2012.

[105] O. Schultz, S. W. Glunz, S. Riepe and G. P. Willeke, „High-efficiency solar cells on phosphorus gettered multicrystalline silicon substrates," *Prog. Photovolt., Res. Appl.,* 14, p. 711–719, 2006.

[106] D. Zielke, S. Herlufsen, F. Werner and J. Schmidt, „Multicrystalline silicon solar cell with efficiencies exceeding 20%," *Proc. 29th European Photovoltaic Solar Energy Conf., WIP, München,* pp. 1282 - 1285, 2014.

[107] J. B. Price, H. R. Huff and R. R. Burgess, *The electrochemical siciety softbound proceedings series, Princeton,* p. 339, 1973.

[108] J. Zhao, A. Wang, M. A. Green and F. Ferrazza, „19.8% efficient "honeycomb" textured multicrystalline and 24.4% monocrystalline silicon solar cells," *Appl. Phys. Lett.,* 73., p. 1991–1993, 1998.

[109] M. J. Stocks, High efficiency multicrystalline silicon solar cells, Ph. D. thesis, Dept. Eng., Australian National University, Canberra, Australia, 1998.

[110] M. J. Stocks, A. J. Carr and A. W. Blakers, „Texturing of polycrystalline silicon," *Sol. Energy Mater. Sol. Cells,* 40, p. 33–42, 1996.

[111] O. Schultz, S. W. Glunz and G. P. Willeke, „Multicrystalline silicon solar cells exceeding 20% efficiency," *Prog. Photovolt., Res. Appl.,* 12, p. 553–558, 2004.

[112] J. Nievendick, J. Specht, M. Zimmer, L. Zahner, W. Glover, D. Stüwe and J. Rentsch, „Formation of a honeycomb texture for multicrystalline silicon solar cells using an inkjetted mask," *Phys. Status Solidi. RRL,* 6, p. 7–9, 2011.

[113] H. Hauser, B. B. Michl, S. Schwarzkopf, V. Kübler, C. Müller, M. Hermle and B. Bläsi, „Honeycomb texturing of silicon via nanoimprint lithography for solar cell applications," *IEEE J. Photovolt.,* 2, pp. 114-122, 2012.

[114] B. Bläsi, H. Hauser, O. Höhn, V. Kübler, M. Peters and A. J. Wolf, „Photon management structures originated by interference lithography," *Energy Procedia,* 8, pp. 712-718, 2011.

[115] R. Grischke, B. Terheiden, S. Mau, N. P. Harder, A. Schoonderbeek, R. Kling, A. Ostendorf, B. Benkena and R. Brendel, „Laser surface texturing for reducing reflection losses in multicristalline silicon solar cells," *Proc. ICALEO 26th Laser Mater. Process. Conf., Orlando, FL,,* 132, p. 123, 2007.

[116] D. Niinobe, H. Morikawa, S. Hiza, T. Sato, S. Matsuno, H. Fujioka, T. Katsura, T. Okamoto, S. Hamamoto, T. Ishihara and S. Arimoto, „Large-size multi-crystalline silicon solar cells with honeycomb textured surface and point-contacted rear toward industrial production," *Sol. Energy Mater. Sol. Cells,,* 95, pp. 49-52, 2011.

[117] H. Morikawa, D. Niinobe, K. Nishimura, S. Matsuno and S. Arimoto, „Processes for over 18.5% high-efficiency multi-crystalline silicon solar cell," *Curr. Appl Phys.,* 10, pp. 5210-5214, 2010.

[118] M. Abbott and J. Cotter, „Optical and electrical properties of laser texturing for high-efficiency solar cells," *Prog. Photovolt., Res. Appl.,* 14, pp. 225-235, 2006.

[119] J. Rentsch, Trockentechnologien zur Herstellung von kristallinen Siliziumsolarzellen, Ph.D. thesis, Fakultät für Angewandte Wissenschaften, Albert-Ludwigs Universität Freiburg, Freiburg, Germany, 2005.

[120] J. C. Zolper, S. Narayanan, S. R. Wenham and M. A. Green, „16.7% efficient, laser textured, buried contact polycrystalline silicon solar cell," *Appl. Phys. Lett.,* 55, pp. 2363-2365, 1989.

[121] „Next-generation Multi-crystalline Photovoltaic Cell", *Technical report*, Solar Power Generation System Promotion Department, Mitsubishi Electric Corporation, Tokyo Bldg., 2-7-3,

Marunouchi, Chiyoda-ku, Tokyo 100-8310, p. E-15, 2011.

[122] D. M. Karnakis, „High power single-shot laser ablation of silicon with nanosecond 355 nm," *Appl. Surf. Sci.,* 252, pp. 7823-7825, 2006.

[123] D. Zielke, D. Sylla, T. Neubert, R. Brendel and J. Schmidt, "Direct Laser Texturing for High-Efficiency Silicon Solar Cells," *IEEE J. Photovoltaics,* vol. 3, no. 2, pp. 656-661, 2013.

[124] M. S. Kulkarni and H. F. Erk, „"Acid-based etching of silicon wafers: Masstransfer and kinetic effects," *J. Electrochem. Soc.,* 147, pp. 176-188, 2000.

[125] P. Saint-Cast, M. Rüdiger, A. Wolf, M. Hofmann, J. Rentsch and R. Preu, „Advanced analytical model for the effective recombination velocity of locally contacted surfaces," *J. Appl. Phys.,* 108, pp. 013705-1– 013705-7, 2010.

[126] S. B. Projekt., „Abbildende Verlustanalyse von Solarzellen für die industrielle Fertigungskontrolle and die Ausbildung Kurzbezeichnung LOANA (LOssANAlysis). Förderkennzeichen 0327661," 2010.

[127] R. Brendel, M. Hirsch, R. Plieninger and W. J. H., „Quantum Efficiency Analysis of Thin-Layer Silicon Solar Cells with Back Surface Fields and Optical Confinement," *IEEE Transactions On Electron Devices,* 43, pp. 1104-1113, 1996.

[128] P. A. Basore, „Extended spectral analysis of the internal quantum efficiency," *Proc. 23th IEEE Photovoltaic Specialists Conf., Louisville, KY, USA,* pp. 147-152, 1993.

10 List of Publications

Refereed journal papers

J1 D. Zielke, J. H. Petermann, F. Werner, B. Veith, R. Brendel and J. Schmidt, "Contact passivation in silicon solar cells using atomic-layer-deposited aluminum oxide layers," *Phys. Status Solidi RRL,* 5, pp. 298-300, 2011.

J2 J. H. Petermann, D. Zielke, J. Schmidt, F. Haase, E. G. Rojas and R. Beandel, „19% - efficient and 43 µm - thick crystalline Si solar cell from layer transfer using porous silicon," *Prog. Photovolt: Res. Appl.,* 20, Nr. 1, pp. 1-5, 2011.

J3 F. Werner, B. Veith, D. Zielke, L. Kühnemund, C. Tegenkamp, M. Seibt, R. Brendel, and J. Schmidt, "Electronic and chemical properties of the c-Si/Al_2O_3 interface", *J. Appl. Phys.*, 109, 113701-1 – 6, 2011.

J4 R. Brendel, J. H. Petermann, D. Zielke, H. Schulte-Huxel, M. Kessler, S. Gatz, S. Eidelloth, R. Bock, E. G. Rojas, J. Schmidt, and T. Dullweber, "High-Efficiency Cells From Layer Transfer: A First Step Toward Thin-Film/Wafer Hybrid Silicon Technologies", *IEEE J. Photovoltaics*, 1, pp. 9-15, 2011

J5 D. Zielke, D. Sylla, T. Neubert, R. Brendel and a. J. Schmidt, "Direct Laser Texturing for High-Efficiency Silicon Solar Cells," *IEEE J. Photovoltaics,* 3, no. 2, pp. 656-661, 2013.

J6 J. Schmidt, V. Titova and D. Zielke, „Organic-silicon heterojunction solar cells: Open-circuit voltage potential and stability," *Appl. Phys. Lett.,* pp. 183901-1-4, 2013.

J7 D. Zielke, A. Pazidis, F. Werner and J. Schmidt, „Organic-silicon heterojunction solar cells on n-type silicon wafers: The BackPEDOT concept," *Sol. Energy Mater. Sol. Cells,* 131, pp. 110-116, 2014.

J8 F. Werner, Y. Larionova, D. Zielke, T. Ohrdes, and J. Schmidt, „Aluminum-oxide-based inversion layer solar cells on n-type crystalline silicon: Fundamental properties and efficiency potential", *J. Appl. Phys.*, vol. 115, pp. 073702-1 – 12, 2014.

Refereed papers presented at international conferences

C1 B. Veith, F. Werner, D. Zielke, R. Brendel, J. Schmidt, "Comparison of the thermal stability of single Al_2O_3 layers and Al_2O_3 /SiN_x stacks for the surface passiviation of silicon", *Energy Procedia*, 8, pp. 307-312, 2011.

C2 D. Zielke, C. Niehaves, W. Lövenich, A. Elschner, M. Hörteis and J. Schnidt, „Organic-silicon solar cells exceeding 20% efficiency," *Energy Procedia,* 77, pp. 331-339, 2015.

C3 F. Werner, B. Veith, D. Zielke, L. Kühnemund, C. Tegenkamp, M. Seibt, J. Schmidt, and R. Brendel, „*Improved understanding of recombination at the Si/Al_2O_3 interface*",*Proc. 25th Europ. Photovolt. Solar Energy Conf., Valencia, Spain* (WIP, Munich) , pp. 1121 – 1124, 2010.

C4 J. Schmidt, F. Werner, B. Veith, D. Zielke, R. Bock, V. Tiba, R. Poodt, F. Roozeboom, A. Li, A. Cuevas and R. Brendel, „*Industrially relevant Al_2O_3 deposition techniques For the surface passivation of si solar cells*" *Proc. 25th Europ. Photovolt. Solar Energy Conf., Valencia, Spain* (WIP, Munich), pp. 1130 – 1133, 2010.

C5 D. Zielke, J. H. Petermann, F. Werner, B. Veith, R. Brendel and J. Schmidt, „21.7 % efficient PERC solar cell with AlOx tunneling layer," *Proceedings 25th Europ. Photovolt. Solar Energy Conf., Hamburg, Germany* (WIP, Munich) , pp. 1115 – 1119, 2011.

C6 J. Schmidt, D. Zielke, W. Lövenich, M. Hörteis and A. Elschner, „Organic-silicon Heterojunctions: a Promising New Concept for High-efficiency Solar Cells," *Proceedings of the 6th WCPEC, Kyoto, Japan,* pp. 869-870, 2014.

C7 D. Zielke, S. Herlufsen, F. Werner, and J. Schmidt, "*Multicrystalline silicon solar cells with efficiencies exceeding 20%*", *Proc. 29th Europ. Photovolt. Solar Energy Conf., Amsterdam, Netherlands* (WIP, Munich), pp. 1282 – 1285, 2014.

C8 R. Gogolin, D. Zielke, W. Lövenich, R. Sauer, J. Schmidt, „Silicon heterojunction solar cells combining an *a*-Si:H electron-collector with a PEDOT:PSS hole-collector", *6th SiliconPV, Chambéry, France*, in press, 2016.

C9 J. Schmidt, D. Zielke, R. Gogolin, R. Sauer, W. Lövenich, „Recent Advances in Polymer/Silicon Heterojunction Solar Cells", presented at the *32th Europ. Photovolt. Solar Energy Conf., Munich, Germany* (WIP, Munich), in press. 2016.

C10 J. Schmidt, D. Zielke, "Novel types of heterojunction silicon solar cells: concepts and efficiency potentials", *12th Photovoltaic Science Applications and Technology Conference, Liverpool, UK* 2016.

Awards and Prizes

A1 SiliconPV Award, s'Hertogenbosch, Netherlands, 2014

A2 NanoDay 2015, NanoDay of the Laboratory of Nano and Quantum Engineering in Hannover, Poster Award

Curriculum vitae

Name:	Dipl.-Phys. Dimitri Zielke
Date of birth:	24.11.1983
Place of birth:	Schapaewsk, Russia
Family status:	married to Sofie Gelzer

Since 03/11	Research associate and doctoral candidate at the Institute for solar energy research Hamelin (ISFH) in the materials research group of Prof. Dr. Jan Schmidt
10/10 – 02/11	Research associate at ISFH, material research group
10/04 – 10/10	Study of technical Physics, Leibniz Universität Hannover
	Diploma thesis at ISFH: "Rückseitenpassivierung von kristallinen Siliciumsolarzellen mit Aluminiumoxid"
08/08 – 05/09	Academic exchange year, Michigan Technological University, USA
09/01 – 06/04	Fachgymnasium Technik, Hannover
	General qualification for university entrance (Abitur)
09/98 – 06/01	Secondary school, Ronnenberg
04/97 – 08/97	Secondary school, Roßla, Germany
09/91 – 02/97	Elementary school, Schapaewsk, Russia

Danksagung

Abschließend möchte ich mich ganz herzlich bei Denen bedanken, die zum Gelingen dieser Arbeit beigetragen haben. Besonderer Dank gilt:

- Prof. Dr. Rolf Brendel für die Möglichkeit diese Arbeit am ISFH durchführen zu können;
- Prof. Dr. Jan Schmidt für seine ausgezeichnete wissenschaftliche Betreuung sowie für die vielen Anregungen und den Freiraum beim Gestalten dieser Arbeit;
- Prof. Dr. Tobias Wietler für die freundliche Übernahme des Korreferats;
- Prof. Dr. Olaf Lechtenfeld für die freundliche Übernahme des Prüfungsvorsitzes;
- Boris Veith-Wolf für die Einführung in die ISFH Abläufe und die fruchtbaren Gespräche und insbesondere dafür, dass er stets bei meiner (linken) Seite ist;
- ALD-Team Boris Veith-Wolf und Florian Werner;
- PEDOT-Team Ralf Gogolin, Valeriya Titova, Claudia Niehaves und Conny Marquard;
- SolarWinS-Team Sandra Herlufsen und Rafael Krain;
- Laser-Team Tobias Neubert, David Sylla und Peter Giesel;
- Henning Schulte-Huxel für die zahlreichen Tipps;
- Ralf, Henning, Valeriya, Boris und Andeas Moor für das Korrekturlesen;
- Marita Steihof, Susanne Mau, Sarah Spätlich und Anja Christ für die Unterstützung im Reinraum;
- Michael Weiss und Stefan Beisse für die Instandhaltung der Anlagen;
- Bettina Wolpensinger für die schönen REM und TEM Aufnahmen;
- DoktorandInnen/KollegInnen Alexandra Pazidis, Jörg Käsewiter, Sören Schäfer, Helge Hannebauer, Robert Witteck, Fabian Kiefer, Hendrik Holst, Dennis Brendemeier, Dominic Walter, Verena Stekenreiter, Christopher Kranz, Jan Hensen, Catherin Gemmel, Malte Vogt, Michael Rienäcker, Nadine Wehmeier, Arnaud Morlier, Felix Hase und Martin Wolf und Susanne Blankemeyer;
- Bärwatchteam Sebastian Gatz und Jan Hendrik Petermann;
- ITP-Kulturprogramm Organisatoren Tobias Ohrdes und Hannes Wagner;
- allen weiteren KollegInnen am ISFH, die nicht persönlich erwähnt wurden;
- Meinen Eltern für alles;
- Meiner Frau für die Geduld mit mir;
- Meiner Tochter Katharina, dass sie geduldig bis zur Abgabe dieser Arbeit gewartet hat.